UC Berkeley
UC Berkeley Electronic Theses and Dissertations

Title
Solid-Liquid Interdiffusion Bonding of Silicon Carbide to Steel for High Temperature MEMS Sensor Packaging and Bonding

Permalink
https://escholarship.org/uc/item/0r09f7ns

Author
Chan, Matthew

Publication Date
2013

Peer reviewed|Thesis/dissertation

eScholarship.org Powered by the California Digital Library
University of California

Solid-Liquid Interdiffusion Bonding of Silicon Carbide to Steel for High Temperature MEMS Sensor Packaging and Bonding

By

Matthew Wei-Jen Chan

A dissertation submitted in partial satisfaction of the

requirements for the degree of

Doctor of Philosophy

in

Engineering - Mechanical Engineering

in the

Graduate Division

of the

University of California, Berkeley

Committee in charge:

Professor Albert P. Pisano, Chair
Professor Liwei Lin
Professor Junqiao Wu

Fall 2013

Solid-Liquid Interdiffusion Bonding of Silicon Carbide to Steel for High Temperature MEMS Sensor Packaging and Bonding

Copyright © 2013

by

Matthew Wei-Jen Chan

Abstract

Solid-Liquid Interdiffusion Bonding of Silicon Carbide to Steel for High Temperature MEMS Sensor Packaging and Bonding

by

Matthew Wei-Jen Chan

Doctor of Philosophy in Engineering - Mechanical Engineering

University of California, Berkeley

Professor Albert P. Pisano, Chair

Complex engineering systems ranging from automobile engines to geothermal wells require specialized sensors to monitor conditions such as pressure, acceleration and temperature in order to improve efficiency and monitor component lifetime in what may be high temperature, corrosive, harsh environments. Microelectromechanical systems (MEMS) have demonstrated their ability to precisely and accurately take measurements under such conditions. The systems being monitored are typically made from metals, such as steel, while the MEMS sensors used for monitoring are commonly fabricated from silicon, silicon carbide and aluminum nitride, and so there is a sizable thermal expansion mismatch between the two. For these engineering applications the direct bonding of MEMS sensors to the components being monitored is often required. This introduces several challenges, namely the development of a bond that is capable of surviving high temperature harsh environments while mitigating the thermally induced strains produced during bonding.

This project investigates the development of a robust packaging and bonding process, using the gold-tin metal system and the solid-liquid interdiffusion (SLID) bonding process, to join silicon carbide substrates directly to type-316 stainless steel. The SLID process enables bonding at lower temperatures while producing a bond capable of surviving higher temperatures. Finite element analysis was performed to model the thermally induced strains generated in the bond and to understand the optimal way to design the bond. The cross-sectional composition of the bonds has been analyzed and the bond strength has been investigated using die shear testing. The effects of high temperature aging on the bond's strength and the metallurgy of the bond were studied. Additionally, loading of the bond was performed at temperatures over 415 °C, more than 100 °C above the temperature used for bonding, with full survival of the bond, thus demonstrating the benefit of SLID bonding for high temperature applications.

Lastly, this dissertation provides recommendations for improving the strength and durability of the bond at temperatures of 400 °C and provides the framework for future work in the area of high temperature harsh environment MEMS packaging that would take directly bonded MEMS to temperatures of 600 °C and beyond.

Dedicated to my wife, Krissy, and my parents, Gaik and Charles.
It's been quite a journey and your support has meant the world to me.

Contents

Abstract **1**

Dedication **i**

Contents **ii**

List of Figures **v**

List of Tables **vii**

Acknowledgements **viii**

1 Introduction **1**
1.1 Direct Bonding Applications and the Need for High Temperature Bonds . . . 2
1.2 A Survey of Existing Bonding Methods . . . 3
1.2.1 Lower Temperature Application Bonding: Below 250 °C . . . 5
1.2.2 Higher Temperature Application Bonding: 300 - 500 °C . . . 6
1.3 Materials for Bonding . . . 9
1.4 Outline of Dissertation . . . 9

2 Solid-Liquid InterDiffusion Bonding Process **11**
2.1 The Process of Solid-Liquid InterDiffusion . . . 11
2.2 Material System Selection for SLID Bonding . . . 14
2.3 Fabrication Process for Silicon to Silicon Substrate SLID Bonding . . . 16
2.4 Fabrication Process for Silicon Carbide Substrate to Steel SLID Bonding . . . 17
2.4.1 The SiC Substrates . . . 18
2.4.2 The Type-316 Stainless Steel Substrate . . . 18
2.4.3 Electroplating of Soft Gold . . . 19
2.4.4 Selection and Preparation of Low Melting-Point Metal . . . 25
2.4.5 Heating Process for SLID Bonding . . . 26

3 Design and Theory of SLID Bonds for High Temperatures Applications **30**
3.1 Tailoring the Thicknesses of the SLID Bond Layer . . . 30
3.1.1 Layer Thicknesses in Silicon to Silicon SLID Bonding . . . 31
3.1.2 Layer Thicknesses in Silicon Carbide to Steel SLID Bonding . . . 31
3.2 Analytical Modeling of Thermally Induced Strains . . . 32

3.3 Computer Modeling of Thermally Induced Strains 39
3.3.1 Bond Shape Geometries of the SLID Bond 41
3.3.2 Cooling the Square Shaped SLID Bond After Bonding 42
3.3.3 Reheating the Square Shaped SLID Bond to Operational Temperature 43
3.3.4 Modeling of Alternate Bond Geometries 44

4 Characterization and Testing of the SLID Bonds 50
4.1 Die Shear Testing Method 50
4.2 Microscopy and Chemical Composition Analysis Methods 53
4.2.1 Optical microscopy 53
4.2.2 Scanning Electron Microscopy and Energy Dispersive X-Ray Analysis 54
4.2.3 Metallographic Polishing 55
4.3 Characterization and Testing of Si to Si SLID Bonds 57
4.3.1 Die Shear Testing of Si to Si SLID Bonds 57
4.3.2 Optical and Compositional Analysis of Si to Si SLID Bonds 57
4.4 Characterization and Testing of SiC to Steel SLID Bonds 60
4.4.1 Die Shear Testing of SiC to Steel SLID Bond After Cooling 60
4.4.2 Compositional Analysis of SiC to Steel SLID Bond After Cooling . . 62
4.4.3 Die Shear Testing of SiC to Steel Bonds after High Temperature Aging 67
4.4.4 Elevated Temperature Loading of SiC to Steel Bonds 70
4.4.5 High Temperature Exposure Testing of SiC to Steel SLID Bond . . . 74

5 Conclusion 76
5.1 Improving the SLID Bonding of Silicon Carbide to Steel 76
5.2 Future Works and Directions 77
5.2.1 SLID Bonding with Nanoparticles or Reactive Nano-Layers 77
5.2.2 Gradual Layering of Increasing CTE Materials 77
5.2.3 Material Systems for Higher Temperature Bonds (>600 °C) 78

Bibliography 79

Appendix A 85

A ANSYS Code for Thermal Strain Modeling of SLID Bond 86
A.1 MATLAB Script for Calculating SLID Bond Layer Thicknesses and Compositions 86
A.2 MATLAB Script for Analytical Model of In-Plane Stresses 86
A.3 ANSYS Model Code for Stress Distribution 90
A.4 ANSYS Macro Code for Material Properties 92
A.5 MATLAB Script for Calculating SLID Bond Area in Si-to-Si Bond 96
A.6 MATLAB Script for Calculating DOE Cause and Effects 97

B Process Recipes and Notes for SLID Bonding 98
B.1 E-Beam Evaporation Thin Films Deposition 98
B.2 Electroplating 98
B.3 Substrate Dicing 98

B.4 Heating the SLID Bond 99

List of Figures

1.1 Overview of sensor bonding for high temperature applications 2
1.2 Si MEMS DETF resonant strain gauge bonded to steel via induction heating 6
1.3 Residual flux on SiC die after brazing 7
1.4 Breakage of Si die upon cooling after high temperature brazing 8
1.5 Bonding of Si dies to steel engine valves using S-Bond 400 8

2.1 Generic eutectic binary phase diagram 12
2.2 Phase diagram for gold-tin metal system 14
2.3 Overview of gold-tin SLID bonding process 15
2.4 Metal layer combinations used in Si to Si SLID bonds 17
2.5 Gold electroplating bath setup 20
2.6 SLID bonding fabrication process for MEMS substrate 21
2.7 Inspection of electroplated film on SiC die 22
2.8 SLID bonding fabrication process for type-316 stainless steel 24
2.9 ASTM D3359-09 adhesion testing of plated gold 25
2.10 Step height profile of gold electroplating on stainless steel 26
2.11 Components of the heater setup for SLID bonding 27
2.12 Assembled heater with sample for SLID bonding 28
2.13 Heating profile for SLID Bonding 29

3.1 Layers of SLID bond for analytical model 33
3.2 Analytical calculations of bond's in-plane thermal stresses 38
3.3 Finite element analysis mesh for SLID bonding simulation 40
3.4 Different SLID bond geometries modeled in ANSYS 41
3.5 Thermal stress model of bonding stack cooled to room temperature 42
3.6 Thermal stress model of bonding stack at operating temperature 43
3.7 Comparison of thermal stresses generated when cooling and reheating SLID bond 44
3.8 Thermal stress from cooling center-bonded geometry 47
3.9 Thermal stress from reheating center-bonded geometry 47
3.10 Thermal stress from cooling small center-bonded geometry 48
3.11 Thermal stress from reheating small center-bonded geometry 48
3.12 Thermal stress from cooling cross-bonded geometry 49
3.13 Thermal stress from reheating cross-bonded geometry 49

4.1 MIL-STD 883J die shear strength requirements for the SLID bond 51

4.2 Schematic of the die shear bond tester 52
4.3 Graph of shear force versus time for an example die shear test 53
4.4 EDX analysis spectrum for Au80%wt.-Sn20%wt. 55
4.5 Metallographic polishing samples of bonded SiC to Steel 56
4.6 Top-down view of Si to Si bond surface before and after shear testing 58
4.7 Cross-sectional image of the Si to Si Bond 58
4.8 Top-down view of Si to Si bond surface before and after shear testing 59
4.9 SEM Image of SLID bond before and after bonding 63
4.10 Fracture surface EDX analysis on steel side of bond after shear testing . . . 65
4.11 Fracture surface EDX analysis on SiC side of bond after shear testing 66
4.12 Oven setup for high temperature loading tests 68
4.13 Cross section of SLID bond before and after high temperature aging 68
4.14 Excess solder diffusion outside bond area after high temperature exposure . . 69
4.15 Cross section compositional analysis of fresh SLID bond 70
4.16 Cross section compositional analysis of aged SLID bond 71
4.17 Test apparatus for high temperature loading of SLID bond 72
4.18 Operational schematic of high temperature loading apparatus 73
4.19 High temperature loading apparatus operating in oven 74
4.20 High temperature melting test of SLID bond using IR lamp 75

List of Tables

2.1 Metallization used for Si to Si SLID bonding 16

3.1 Material properties of SLID bond components for finite element and analytical modeling 34
3.2 Analytically modeled in-plane stresses from heating and cooling the SLID bond 37

4.1 Design of experiments with SLID bonding parameters 61
4.2 Die shear testing strength results 62

B.1 Heating recipe for HP 6263B and MS-M1000 ceramic heater 99

Acknowledgements

First and foremost, I acknowledge Professor Albert Pisano for his support and guidance over the course of my graduate studeis. My peers in Professor Pisano's lab have offered invaluable support over the course of my studies, and have made the lab an enjoyable place to work. For this I thank all the members of the Berkeley MEMS Analysis and Design laboratory, especially Fabian Goericke, Michael Sheppy, Debbie Senesky, David Myers, Sarah Wodin-Schwartz and Kirti Mansukhani.

I thank Professor Knut Aasmundtveit of Vestfold University College in Norway for his assistance and mentorship with my research. Visiting Norway to conduct my research and learn in depth about microelectronic packaging and experimentation has shaped my scientific approach.

The staff of the Mechanical Engineering Student Machine Shop have provided me with great assistance in the design and fabrication of my test setups and I would like to thank Gordon Long and Mick Franssen in particular. I would also like to thank the staff of the Marvell Nanofabrication Laboratory, especially Joe Donnelly and Jay Morford, for keeping the tools running and enabling the microfabrication in my research.

Chapter 1

Introduction

High temperature harsh environments are difficult places to deploy sensors, yet sensors in such places can provide critical data to improve complex engineering systems. Silicon (Si) microelectromechanical systems (MEMS) have long demonstrated their ability to take highly precise, highly accurate measurements of temperature, acceleration, pressure, inertia, and strain, and have demonstrated their ability to operate in moderate temperature applications, below 100 °C [1, 2]; however, for high temperature applications, a more robust material system is required. For such high temperature applications, silicon carbide (SiC) has demonstrated outstanding mechanical, electrical, and chemical properties for MEMS sensor technology and electrical circuits. It softens less than silicon at elevated temperatures, as a wide bandgap semiconductor it is suitable for operation at high temperatures, and it is resistant to chemical attack [3, 4, 5]. This dissertation investigates the solid-liquid interdiffusion (SLID) packaging approach for directly bonding silicon carbide substrates onto steel for high temperature harsh environment applications and the approach used to join materials with large mismatches in coefficients of thermal expansion, for high temperature harsh environment monitoring applications.

Much effort has been spent by many groups to develop sensor technologies and material systems capable of withstanding these environments, such as silicon carbide (SiC), aluminum nitride (AlN) and aluminum oxide (Al_2O_3) [6, 7, 8, 9, 10, 11, 12, 13]. In university research these MEMS sensors have demonstrated their ability to function unencapsulated in laboratory settings and conditions, and the materials used in these sensors have been tested independently for survival in high temperature steam environments[14, 15]. However, to be deployed in real-world harsh environment applications successfully, where the sensor cavity must maintain hermeticity and the sensor requires attachment directly to mechanical components being monitored, a new packaging approach is required. This packaging approach must ensure a robust connection of the sensor to the component under a wide range of conditions.

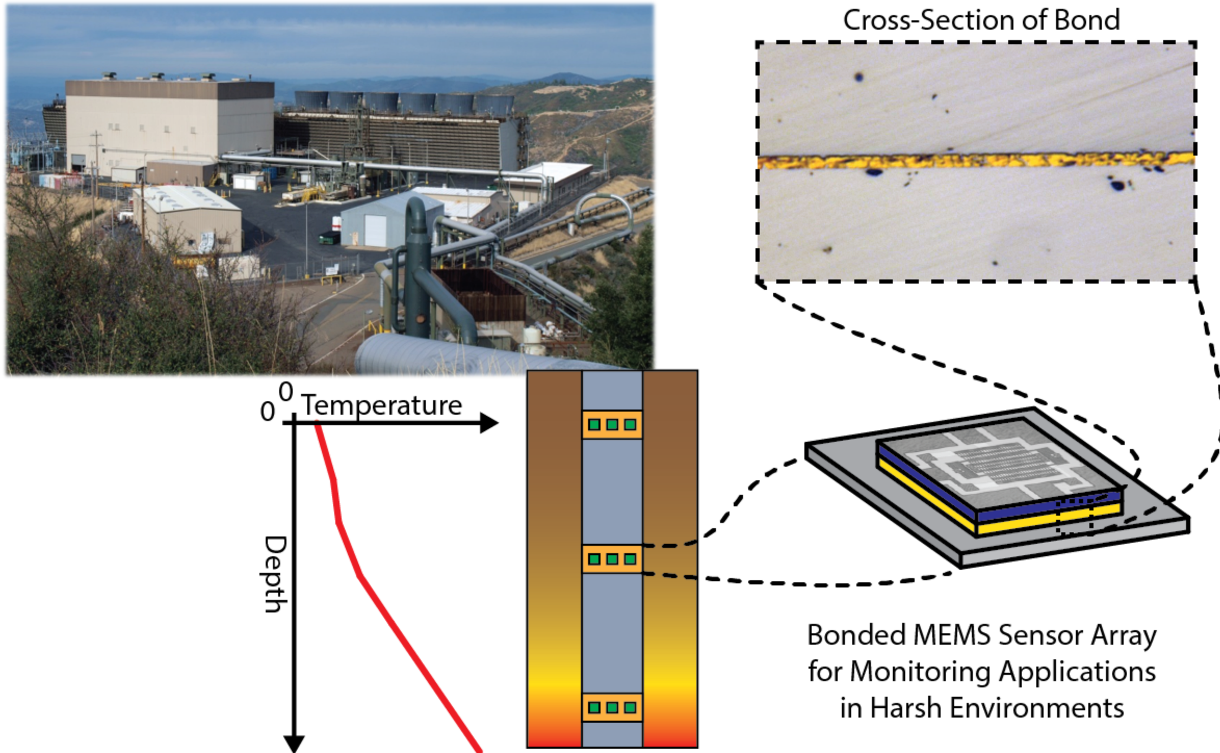

Figure 1.1: Sensor bonding for high temperature applications, such as geothermal well monitoring, require a robust direct attachment of the sensor to the component being monitored. In the case of geothermal well monitoring, the sensor must be directly bonded to the pipe wall of the extraction or injection well in order to measure the pressure of the fluid passing through the pipe.

1.1 Direct Bonding Applications and the Need for High Temperature Bonds

With intensified global interest in meeting the world's current energy demands there is a need to better tap renewable resources and improve the efficiency and lifetime of many currently existing engineering systems[16]. These engineering systems, such as geothermal wells, oil-and-gas pipelines and steam turbines often operate at high temperatures and require the implementation of robust sensors to provide needed data on operating conditions and environmental conditions. In the case of geothermal well monitoring sensors, as shown in Figure 1.1, increasing the operating efficiency of the wells would require down-hole monitoring of temperature and pressure. These measurements would allow enhanced geothermal systems, which pump water deep into bedrock to be heated and recovered, to determine the right pumping conditions to maximize energy output from a production well. At depth, these enhanced geothermal systems operate at temperatures around 375 °C and with wet steam, and sometimes corrosive environments and such an application would require a robust sensor bonding method to survive. Additionally, in the cases of enhanced geothermal systems and oil and gas well exploration, the use of robust MEMS accelerometers and inertial mea-

surement sensors would improve navigation for well-drilling, enabling these systems to more accurately navigate to subterranean areas of interest while drilling the wells. With steam turbines, high-temperature MEMS sensors could provide in-turbine structural monitoring to measure the mechanical creep of turbine blades and enable the lifetime monitoring of turbine rotors and stators. In each these long-term applications, it is unavoidable to expose the MEMS to elevated temperatures for prolonged periods of time, and so a direct bonding method is required for securing MEMS sensors to the metal in question for successful deployment.

The direct bonding of MEMS sensors to the metal components being monitored is required for applications requiring strain monitoring, torque measuring, or pressure monitoring. For strain monitoring applications it is imperative that the strain from the component is being measured directly and that the strain transfer from the component to the sensor, through the bonding layer must be well characterized and repeatable. Yielding of the bond layer would affect the sensitivity of the sensor and limit the range of strains that could be measured. Similarly, for pressure sensing applications, the hermeticity of the bond connecting the sensor to the component is of major importance. For accelerometers and inertial strain sensors, it is paramount that the mechanical stress from the packaging operation does not affect the sensitivity and accuracy of the sensor, and further, that the bond can survive the shocks encountered in the application.

Packaging is responsible for the stability and performance of MEMS sensors and it requires great attention to mitigate the effects of thermal stress mismatches and the effect of the packaging process on the sensor. The packaging development cost for microsystems can range from 20% to 95% of the total production cost, depending on wether the MEMS device requires a simple plastic encapsulation or a highly-specialized packaging design and approach. Additionally, the design of the MEMS packaging has a significant impact on the sensitivity of device and its overall performance[17]. When considering the packaging and bonding of MEMS sensors directly to metals like steel, several issues arise, namely the distinct differences in material properties between ceramics, such as silicon carbide, and metals like steel.

The main obstacle encountered for the success of directly bonded MEMS sensors made from materials like crystalline silicon carbide is that the high temperature harsh environment components they are meant to monitor are typically made from materials like steel; a material with a significantly different coefficient of thermal expansion (CTE). With a CTE mismatch of around $13.3 \times 10^{-6}\,°\mathrm{C}^{-1}$ between steel and silicon carbide, large changes in temperature impart significant thermal strains as a result of the mismatch. This dissertation investigates an approach to overcome this problem and enable direct bonding of silicon carbide to steel.

1.2 A Survey of Existing Bonding Methods

A survey of existing technologies for joining MEMS substrates to steel reveals the benefits and drawbacks of each technology. When considering the joining of components several methods the most common engineering methods used are mechanical fastening, adhesive bonding, soldering, brazing and welding. Mechanical fastening consists of using bolts, screws, or rivets to provide friction and clamping forces to hold components together. This type of joining

method is suitable for operation over wide temperature ranges and in harsh environments; however, it is typically reserved for macro-scale applications and would be difficult to implement for interfacing MEMS-scaled devices. Furthermore, mechanical fastening of MEMS materials would obscure the measurement of mechanical strain, without a direct bond between the strain sensor and the object being monitored.

Adhesive bonding is a method suitable for many MEMS applications for lower temperature applications, below 250 °C. For many low temperature applications polymer-based adhesives are suitable and economically viable. At higher temperatures and longer service lives, however, these polymeric adhesives tend to degrade mechanically. When subjected to humid environments, these adhesives tend to absorb moisture, which interacts with the polymers and causes a reduction in cohesive and adhesive strength [18]. High temperature epoxies such as ceramic adhesives can be used for extreme high temperatures, ranging from 700 °C to 1100 °C. These adhesives can be designed to have high coefficients of thermal expansion, however they are best suited for joining materials closely matched in coefficient of thermal expansion. Ceramic adhesives tend to be brittle and do not accommodate the bonding of materials with mismatched CTE, such as silicon carbide and steel. Furthermore, if electrical contact from the sensor to the metal component being monitored is required (*i.e.*, for electrical grounding), non-conductive ceramics would not work for such applications.

Soldering is traditionally a reflow process which utilizes low melting-point metals with liquidus points below 400 °C and it is a technique widely used throughout the electronics and MEMS industry[19]. Typical solders have liquidus temperatures ranging from 100 °C to 400 °C and come in many different metallurgies suitable for different moderate temperature applications. In soldering, the temperature is raised above the melting point of the solder, at which point the liquid solder interacts with the components being joined, both mechanical and chemically. Upon cooling, the solder solidifies and a solid joint is made. Soldering is an acceptable for the joining of materials that are mismatched in CTE because with the low operating temperatures, the thermal strains generated are relatively low. Though suitable for joining metalized semiconductor materials such as silicon and silicon carbide with metals like steel, for high temperature applications most solders would reflow before reaching the harsh environment's operating conditions.

Brazing is a technique similar to soldering, however, it requires higher temperatures to melt the braze. In conventional brazing the components being brazed are both heated above the melting point of the braze used, and held close together. The braze alloys is then fed into the gap between the components and when heated and liquefied, capillary action pulls the liquid braze into the gap. Braze alloys range in melting point from 400 °C to above 1000 °C[20]. With the high bonding temperatures used in brazing several complications arise, namely oxidation and large thermally induced strains caused by CTE mismatch and a large temperature range. Oxidation of the metals in brazing material stack can be mitigated through the use of flux or inert environments. Fluxes are reducing agents that help prevent the formation of surface oxides during heating, and often these fluxes contain acids. Some fluxes are volatile and decompose when thermal energy is provided; however, if the flux residue does not fully escape during the bonding process corrosive impurities are left behind promoting corrosion and degrading the strength of the bond. One category of brazes that is recommended for joining ceramics and metals are Active Metal Brazes (AMB). AMB alloys typically contain metals such as titanium and aluminum which are capable of forming

compounds with ceramics such as silicon and silicon carbide to improve wetting; however the brazing temperature of most AMBs is upwards of 600 °C, reaching up to 980 °C for Titanium-Nickel brazes. Brazing temperatures that high would impart extreme thermal strains for materials not closely matched in CTE.

Finally, welding is a commonly used joining method that one would typically encounter when joining metals in large structures such as bridge trusses, automobile chassis and skyscrapers. It has been investigated as an appropriate method for joining materials on the micro-scale as well, and in certain applications it can be quite advantageous. However, when joining silicon carbide with metals, unlike other ceramics such as aluminum oxide (Al_2O_3) and Sillimanite ($Al_2O_3 - SiO_2$) which can be fusion welded, silicon carbide vaporizes [21]. In this regard, welding is not a viable technique for bonding silicon carbide MEMS directly to metals.

1.2.1 Lower Temperature Application Bonding: Below 250 °C

Many engineering applications exist that require highly sensitive and accurate measurements to be made at temperatures below 250 °C. Because of their sensing capabilities and small form factor, MEMS sensors are becoming ever more prevalent throughout the consumer electronics industry in products such as cell phones and tablet personal computers. Beyond consumer electronics, MEMS can also be used in other monitoring applications including pressure and acceleration sensing for automobiles, automotive shaft torque monitoring and pressure monitoring in deep sea oceanic conditions [22, 23, 24]. In these lower temperature applications, the concern of imparting large thermally induced strains is significantly reduced and polymeric adhesives and low temperature reflow solders can be used with satisfactory results.

For solder bonding of such MEMS and electronics components, many different methods of heating are readily available and well suited. Vacuum furnaces, rapid thermal annealing furnaces and hotplate ovens can be used for packaging MEMS in cleanroom environments, soldering irons and hot-air pencils can be used for spot heating in the research lab setting. Additionally, for solders there are several heating methods that are well suited for bonding MEMS to metals outside of the cleanroom setting in more high-throughput production environments. Induction heating, for example, is a non-contact, rapid and clean method of locally heating an area for bonding. Induction heating is a method already in widespread use in the automotive industry to heat-treat shafts and other various metal components. The direct bonding of silicon double ended tuning fork (DETF) resonant strain gauges to steels, as shown in Figure 1.2, was demonstrated by Chan *et al.* using inductive heating and 96.5Sn-3Ag-0.5Cu solder with a melting point of 217 °C [25] and could be used in situ to mount MEMS sensors to shafts in production environments. While solder bonding performs well in enabling many MEMS technologies for lower temperature applications, as aforementioned at high temperatures, these solders are insufficient for survival of the bonds at high temperatures as they would simply reflow and melt away.

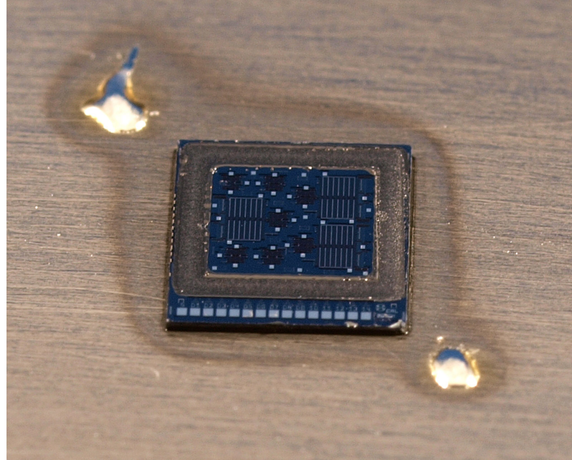

Figure 1.2: For moderate temperature MEMS applications, sensors such as this MEMS DETF resonant strain gauge can be bonded directly to steel using induction heating.

1.2.2 Higher Temperature Application Bonding: 300 - 500 °C

With the need and transition to bonding MEMS for higher temperatures and raising the bar on operational temperatures comes several challenges are introduced. The bonding materials chosen must have melting points exceeding the operational temperatures of the high temperature applications and those materials must be strong enough to make a robust bond. Additionally, with higher temperature bonding, oxidation of the materials being bonded and oxidation of the solders or brazes being used hinder the bonding process and weaken the adhesion of the bond. To combat the issue of melting at low temperatures, proper selection of materials for bonding is paramount. Materials chosen for bonding must be compatible with the processes used for bonding and with the other materials being bonded. To mitigate some the oxidation of the bonds at high temperatures, additional steps can be carried out such as performing the bonding in vacuum or using a chemical flux as a reducing agent to eliminate oxide formation. These additional steps and requirements for the bonding process add complexity and cost to bonding and depend highly upon the bonding application. In extreme harsh environment sensing applications, the additional cost of bonding complexities may be outweighed by the benefit the sensors provide.

In a survey of work performed on silicon and silicon carbide packaging for high temperature applications, it is apparent that the high temperature deployment of silicon carbide and silicon MEMS and electronics is of great interest. In literature there are many explorations of joining silicon to silicon for wafer level high-temperature packaging application using metal thin films and glass frit[26, 27]. In these studies the bonding temperatures run quite high and unlike the bonding of silicon carbide to steel, both top and bottom silicon substrates are matched in the coefficient of thermal expansion, so as they are heated to great temperatures, they expand equally and the produced thermal strains are balanced symmetrically in the bonding stack. Work has been performed in joining sintered (non-crystalline) silicon carbide composites to ferritic steel using a tungsten-palladium-nickel bond for high temperature macro-scale structural and mechanical applications; however, this type of silicon carbide is incompatible with the fabrication of microcircuitry and MEMS sensors [28]. Bonding pro-

cesses for joining silicon carbide with various components, such silicon nitride circuit boards that have been metalized with copper active metal brazes have also been studied though in these works, although the silicon carbide is bonded directly to the copper layer, the underlying silicon nitride circuit board aids in the absorption of some of the thermal strains distributed through the layer stack and balances the strains generated from bonding [29, 30].

These works have not explicitly explored the development of a direct bonding process for joining materials with large CTE mismatches, such as steel and silicon carbide. For the task of developing a bond that would survive high temperatures and be suitable for joining silicon and silicon carbide to steel, traditional brazing was initially investigated in this project. Several braze alloys and active metal brazes including silver-nickel brazes and commercially available S-Bond 400 ($Zn - Al - Ag$) alloy were tested for the bonding of silicon and silicon carbide dies to steel using induction heating and infrared lamp heating. In bonding attempts with the silver-nickel brazes, with melting points between 630 °C and 680 °C, fluxes had to be used, due to accelerated oxidation of the steel and braze alloys at high temperatures. When too much flux was used in the bonding process or when the flux could not escape from underneath the bond during heating, flux residue was often left behind, as shown in Figure 1.3. These flux residues can lead to deteriorated bond performance as the residual acids in the bond will promote corrosion.

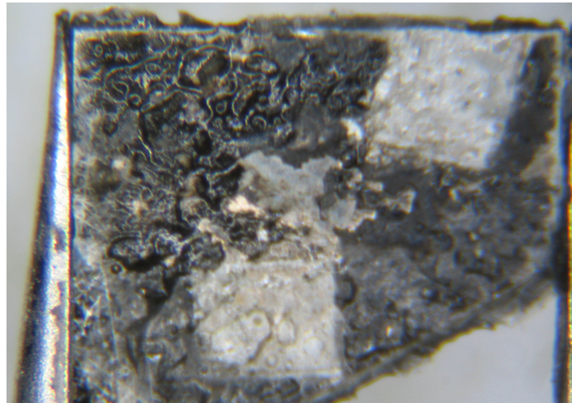

Figure 1.3: Brazing with fluxes introduces additional complications to the bonding of silicon carbide to metals. If the volatile fluxes do not fully escape during bonding, corrosive residues are left behind, impeding the survival of the bond.

When successful brazes with good adhesion and no flux residue was left behind, an additional complication was introduced. With the high temperatures used for brazing, the large thermal strains generated from the CTE mismatch between semiconductor and steel caused the rupture of the dies upon cooling to room temperature, 25 °C, as shown in Figure 1.4. The excellent adhesion of the bonded dies to the steel components was able to transfer thermally induced stresses to the dies greater than the ultimate strengths of the dies, which resulted in the destruction of the die.

Bonding attempts with the S-Bond 400 active braze alloy were also attempted to joining silicon and silicon carbide dies to engine intake valves as shown in Figure 1.5. In accordance with the manufacturer's recommendations, flux was not used for the bonding process and bonds were performed in ambient atmospheric conditions. With the S-Bond 400 active

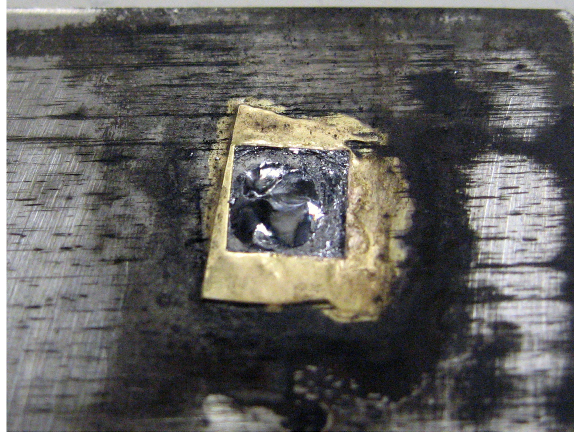

Figure 1.4: Breakage of a silicon die upon cooling back to room temperature after being brazed with silver braze alloy at a temperature of 630 °C. The bond that was made exhibited good adhesion to both the silicon die and the steel and upon cooling to room temperature, the thermal strains induced in the silicon die caused catastrophic rupture of the die.

braze alloy, the high concentration of aluminum present caused significant oxidation during the heating, and even when the braze had reached its liquidus temperature, mechanical agitation was required to break the surface of the oxide that formed. The bonding process was difficult to control and sometimes resulted of the spreading of the S-Bond beyond the desired area of bonding. Even with mechanical agitation, poor adhesion of the bond to the metal valves resulted.

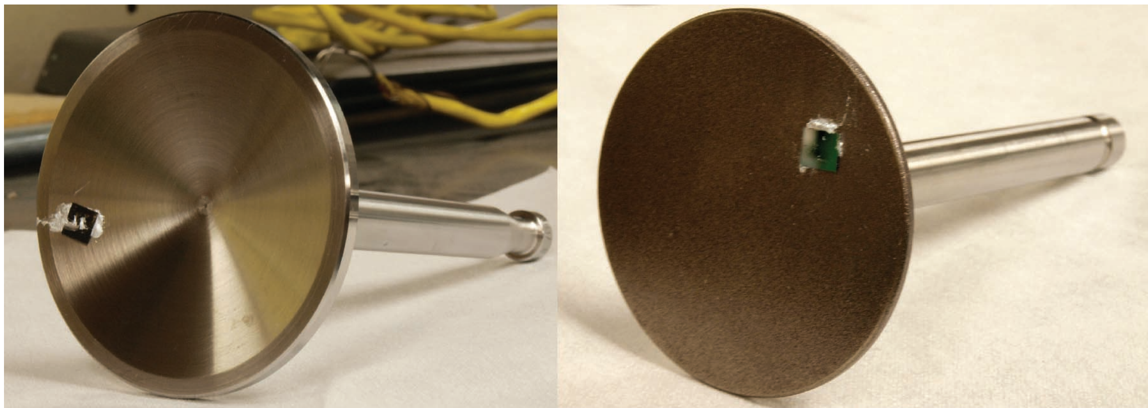

Figure 1.5: Attempts to bond silicon dies to steel engine intake valves were made using S-Bond 400 active braze alloy. Mechanical agitation was required to break up surface oxides, however this process was difficult to control and underlying native oxides covering the steel engine valves caused poor adhesion of the silicon dies.

The focus of this thesis, is the development and application of a bonding technique that can solve these issues of good adhesion and an bond survival at elevated temperatures over 400 °C. With this type of bonding application there are conflicting requirements: a bond must be able to survive high temperatures, yet not induce excessive thermal strains that

cause the bond to fail. This dissertation resolves this issue through the use of the solid-liquid interdiffusion bonding process, described in detail in Chapter 2.

1.3 Materials for Bonding

This dissertation investigates the bonding of silicon to silicon and the bonding of silicon carbide to steel. These two materials are important for sensor deployment of MEMS and circuits into traditional commercial electronics applications and high temperature harsh environment applications. The majority of today's MEMS sensors are made from silicon for commercial grade applications and for high temperature harsh environment applications, silicon carbide devices have drawn much attention for their mechanical, electrical, and chemical robustness. With myriad MEMS sensors for all different applications, the packaging requirements are not uniform across the wide range of applications.

Silicon to silicon bonding is widespread throughout the electronic industry and many types of bonding processes for joining silicon, including anodic bonding and solder reflow bonding, have been developed and well documented. The hermetic sealing of cavities and the direct bonding of silicon to silicon are typical packaging needs that must be fulfilled. This work starts with an investigation of silicon to silicon bonding using the SLID process because crystalline silicon wafers are significantly more cost effective and readily available than crystalline silicon carbide wafers. Bonding with silicon makes for a good starting point for the process development of a bonding method that could be translated to the silicon carbide material system.

For the high temperature harsh environment aspect of this project, the joining of silicon carbide to steel is extremely compelling. Steel is one of the world's most prevalent engineering materials, with uses in automobiles, pipelines, buildings and other aspects of the built infrastructure. The majority of engineering systems that handle or operate in high temperature harsh environments are fabricated out of various grades of steel. In this work, with an emphasis on harsh environment bonding, type-316 stainless steel was chosen for use as the base substrate material used for bonding. Type-316 stainless steel is an abundant marine-grade engineering material used when corrosion resistance is required [31]. In this work the 4H polymorph of silicon carbide was chosen for bonding because it's increased electron mobility and larger bandgap than the more commonly used 6H silicon carbide polymorph [32]. In the niche of high temperature harsh environment electronics, 4H silicon carbide is gaining significant interest for the development of new transistors and circuitry which will soon directly integrate with silicon carbide MEMS devices. This bonding research aims to pave the way to enable the direct bonding of such future circuits and MEMS.

1.4 Outline of Dissertation

This dissertation covers the solid-liquid interdiffusion bonding process in Chapter 2, followed by the theory used to design the bond in Chapter 3. The characterization and testing of the bond are presented to show that SLID bonding is an appropriate approach to solving thermal mismatch issues encountered with bonding for high temperature harsh environments

are discussed in Chapter 4. Lastly the conclusion is presented and some key directions for future works in high temperature harsh environment bonding are laid out in Chapter 5.

Chapter 2

Solid-Liquid InterDiffusion Bonding Process

Alloying in metallurgy is a technique that has been observed as early as 3000 BCE, during the Bronze Age and it has played an important role in both the development of technology and human history. The concept of melting metals together in various proportions to create alloys with different mechanical properties or to join materials together has a long history and has been well documented. Diffusion bonding as we know it was already explored in the 16th century by Italian goldsmith Benvenuto Cellini, who joined small decorative gold spheres onto ornate gold artwork using a reducing flame and copper oxide paint as a solder[33, 34]. The operating principles behind these old processes hold much value and have much value when applied to today's cutting-edge semiconductor packaging technology. The following sections detail the process and mechanism of the solid-liquid interdiffusion (SLID) bonding, the joining of silicon to silicon using SLID bonding and the joining of silicon carbide to steel.

2.1 The Process of Solid-Liquid InterDiffusion

The SLID process, sometimes also known as the transient liquid phase (TLP) bonding process or isothermal solidification bonding process, is a type of diffusion bonding process that differs from typical wide-gap brazing that is encountered in macro-scale engineering because it relies upon the interaction of solid and liquid phases with the bonding temperature held constant. The SLID process arose in the late 1950s and early 1960s and by that time significant amounts of work had been conducted on understanding soldering and brazing processes as well as the diffusion of metals. The basic SLID process involves the use of two metals, M_1 and M_2, which are capable of forming intermetallic alloys with one another. A hypothetical phase diagram for the M_1 and M_2 material system is presented in Figure 2.1 for clarity. As described by Tuah-Poku, the simplest case used to illustrate the SLID process consists of two layers of M_1 that are to be joined by an interlayer of M_2. It is accepted that there are four distinct steps that make up the SLID process and as described by Tuah-Poku these steps are: the dissolution of the interlayer used, homogenization of the liquid, isothermal solidification and homogenization of the bond region [35].

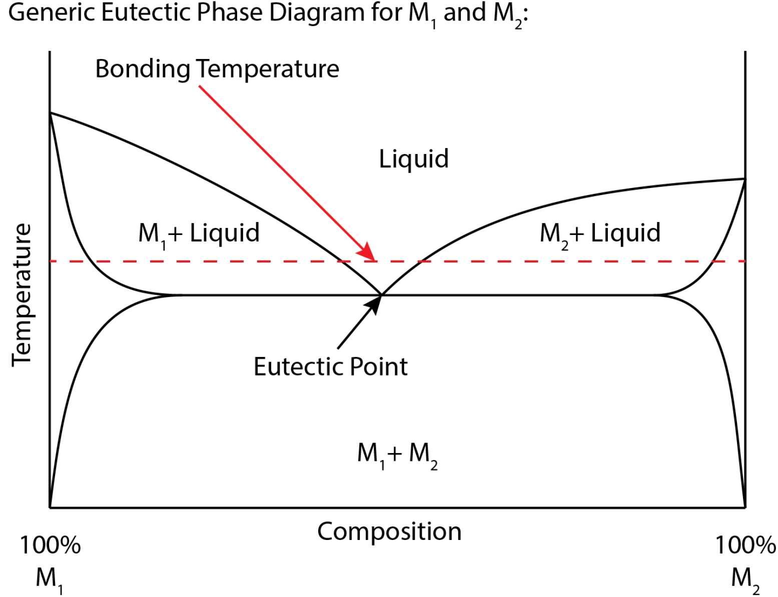

Figure 2.1: A generic binary phase diagram with one eutectic point is provided here for the explanation of the SLID bonding process. This hypothetical phase diagram is for two metals, M_1 and M_2 which are used as the SLID bonding layer in the described bonding process.

In the first step, one metal, M_2, is chosen to be the interlayer and the other, M_1, is used to sandwich the M_2 interlayer. Some bonding force must be applied to ensure excellent contact of the faying surfaces of M_1 with the M_2 interlayer. The temperature is raised above the melting point of the eutectic composition of M_1 and M_2, shown at the eutectic point in Figure 2.1, and is held at a constant temperature for the rest of the bonding process. Due to the intimate contact of the two metals, some of the solid M_1 dissolves into M_2 interlayer. This dissolving process continues because there is a concentration gradient with a surplus of M_2 and it is energetically favorable for the dissolution to continue at the bonding temperature. This process continues into the second step, the homogenization of the liquid, as more M_1 dissolves into M_2 until M_2 is completely and the liquid composition behind becomes homogenous and the liquid zone widens to its maximum thickness. Following this, the third stage of the SLID bonding process occurs: isothermal solidification. In isothermal solidification, the surplus of solid M_1 that contacts the liquid mixture of M_1 and M_2 begins to diffuse into the liquid mixture. As this happens, the liquid zone begins to shrink and solidify as its composition changes and completely freezes [36]. Fick's second law of diffusion governs the rates at which the diffusion reactions occur and the Gibbs free energy dictates the change of states. In the final stage of the SLID bonding process, solid-state diffusion continues with the homogenization of the bond until the system reaches equilibrium [37]. The final composition of the SLID bond depends on the thicknesses of the layers used at the start of bonding. Depending on how much M_1 and M_2 are supplied, after the bond homogenizes and the intermetallic alloys have been formed, there may be an excess of pure M_1 or pure M_2 left after bonding.

The SLID process has been the subject of focus for many research groups. Many macro-scale applications of the SLID process have been studied for the joining of titanium alloys,

nickel superalloys, stainless steel and aluminum [38, 39, 40]. In these large-scale structural applications the temperatures and metallurgy used for SLID bonding require the use of temperatures similar to those in traditional reflow brazing operations and the CTEs of the materials being joined are closely matched: for joining nickel superalloys, bonding temperatures above of 1090 °C are used; for joining stainless steel, temperatures over 870 °C were required; for titanium joining, the temperatures used exceed 700 °C; and for joining aluminum, bonding temperatures are over 550 °C [41, 42]. Additionally, with the thicker layers used, the times required for the diffusion of the bonds are increased to several hours [43], with homogenization of the bond taking up to 100 hours. In these works, the SLID bonding process involves the bonding of two pure metals with both relatively high melting points and whose phase diagrams have an low melting point eutectic point. By requiring the solid metals to form an intermetallic liquid through solid state diffusion, bonding times are significantly increased.

Several groups have specialized in using the SLID process for microelectronic packaging applications [44, 45, 46, 47, 48]. In these studies, the goal of SLID bonding is somewhat different from that of the aforementioned macro scale engineering systems. For these applications, the bonding utilizes the direct melting of a low melting point metal to form a liquid phase, instead of relying upon solid-state diffusion. Using this method, diffusion is approximately 3 times faster and bonding times can be reduced significantly [49]. With microelectronic devices, lower processing temperatures and faster bonding times are attractive due to the thermal budget of the components and so different metal systems are used. The SLID bonding process can not only be applied to the bonding of substrates to circuit boards but to the hermetic sealing of MEMS cavities. The SLID bonding process is achievable with metals commonly used in microelectronic fabrication, including gold, titanium, nickel, silver, tin and indium. One added benefit of performing the SLID bonding process with low melting point metals such as indium or tin is that if the bonding temperature is above the liquidus temperature of the low melting-point metal, the liquid metal will make good contact with the sandwiching layers and the need for applying high clamping forces during bonding is reduced. Additionally, with smaller scale components, bond layer thicknesses can be reduced and the processing time for bonding can be reduced.

One major benefit of the SLID bonding process, and the one that is of greatest importance to this study on SiC to steel bonding, is that with the right choice of materials for bonding the process can be tailored to achieve a low bonding temperature with much higher operational temperatures. This type of behavior has been studied in several material systems including copper-tin, copper-indium, silver-tin, silver-indium, gold-indium and gold-tin [50, 51, 52, 53, 54, 55]. With these material systems, the copper, silver and gold each serve as the high melting point metal while the tin and indium play the role of melting point depressants as they reduce the temperature required for bonding. As the solid-liquid interdiffusion process is carried out in these systems, intermetallic compositions with melting points greater than those of indium and tin are formed. This aspect of SLID bonding is highly appealing for microelectronics applications where subsequent elevated temperature steps are required while the bond remains intact.

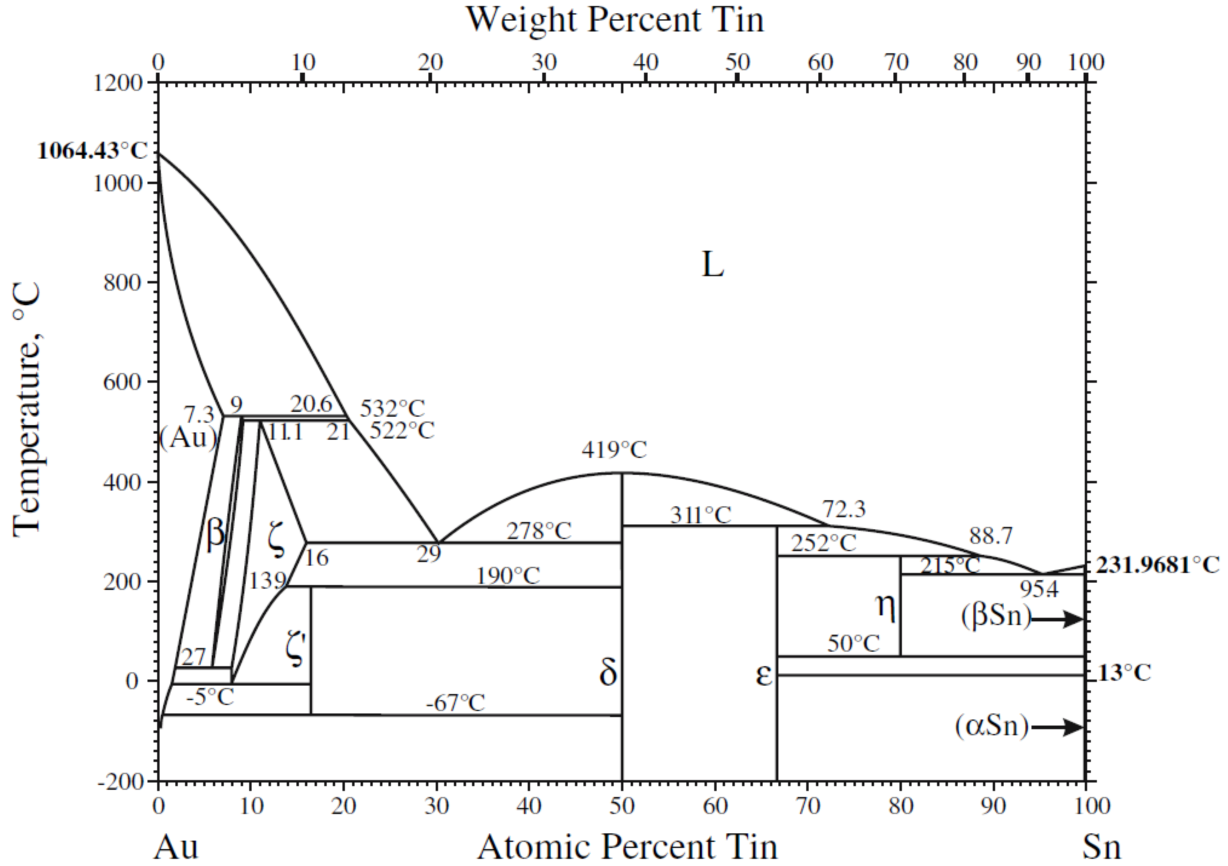

Figure 2.2: Okamoto's phase diagram of the gold-tin material system[59][1]

2.2 Material System Selection for SLID Bonding

For SLID bonding of silicon carbide to stainless steel for high temperature applications, the gold-tin material system was chosen. There are many benefits of the using the gold-tin material system for SLID Bonding. Gold is an inherently corrosion resistant material and does not easily oxidize. This enables the gold-tin SLID bonding process to be performed without the use of fluxes which can detrimentally affect the bond, as mentioned in Section 1.2. This oxidation resistance has enabled the gold-tin SLID bonding process to be performed in ambient atmospheric air environments, free from the use of forming gas or other processing gasses [56]. For commercial applications or bonding of silicon carbide sensors to components in the field, this aspect is highly attractive. With reported gold diffusivities of $5.8 \times 10^{-3} \exp^{-(11000/RT)} \mathrm{cm}^2\,\mathrm{s}^{-1}$ along the c-direction in the crystal structure of tin and $1.6 \times 10^{-1} \exp^{-(17700/RT)} \mathrm{cm}^2\,\mathrm{s}^{-1}$ along the a-direction of the tin crystal, gold quickly diffuse into tin at elevated temperatures which reduces the time required for bonding [57]. Along with the good diffusion rates, alloys of gold-tin exhibit good wetting with gold, ensuring that during the bonding process a good liquid layer can be formed, and large clamping forces for bonding are not required [58]. Additionally, there are intermetallic compositions of gold-tin that are suitable for high temperature survival, above 450 °C.

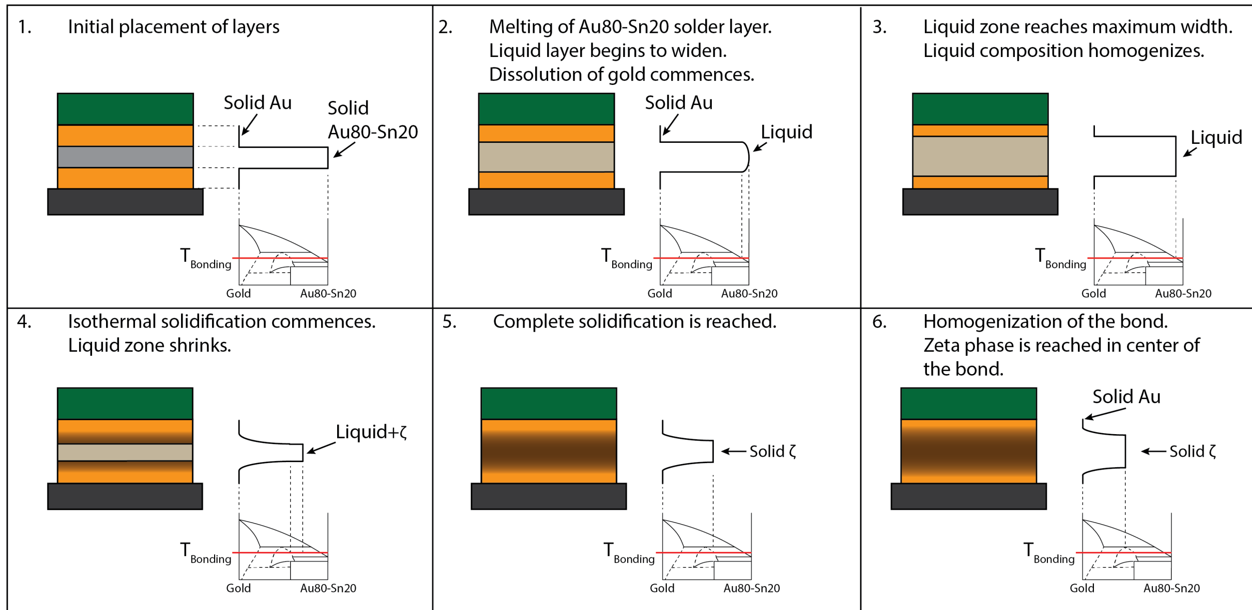

Figure 2.3: The steps of the solid-liquid interdiffusion bonding process, expanded into 6 images for clarity and completeness. In each step of the process, the layers of the SLID bond are shown on the left. The top layer in green is the silicon carbide die and the grey layer at the bottom of the stack is the type-316 stainless steel substrate. To the right of each material stack, the composition of the bond layers, as lined up with the phase diagram below, is presented to show the evolution of the SLID bonding stack as the process progresses. The phase diagrams provided show the Au - Au80%wt.-Sn20%wt. metal system.

Gold is also widely used throughout microelectronic and MEMS industries, so fabricating processes with gold are compatible with such applications. It readily adheres to commonly used adhesion layers such as nickel, titanium and aluminum. In the case of the gold-tin metal system, pure gold serves as the high melting point metal, with a melting point of 1064.43 °C, and pure tin or gold-tin eutectic (Au80%wt.-Sn20%wt.) can serve as the low melting point metal with respective melting points of 232 °C and 278 °C. The gold-tin material system consists of seven different stable intermetallic compositions: $Au_{0.970}Sn_{0.030}$ (α), $Au_{3.6}Sn_{0.4}$(β), $Au_{0.85}Sn_{0.15}$(ζ which exists above 190 °C), Au_5Sn(ζ' which exists below 190 °C), AuSn(δ), $AuSn_2$(ϵ), and $AuSn_4$(η). The phase diagram of the gold-tin metal system is provided in Figure 2.2. From analyzing this phase diagram it is evident that the β and ζ phases of gold-tin, with respective melting points of 532 °C and 522 °C, are attractive for high temperature harsh environment applications based on their high temperature stability.

In SLID bonding with the gold-tin system, if pure tin is used as the melting point depressant for bonding with pure gold with a thickness ratio of at least 3Au:2Sn, upon bonding at temperatures between 232 °C and 419 °C, the tin layer melts and turns completely liquid. The gold that is in contact with this molten tin dissolves into the liquid, as is prescribed by the SLID process. However, there is a tendency for the composition to to reach the δ phase and settle there and form a AuSn barrier layer, due to the minimizing of

[1]Figure reproduced with the expressed permission of Springer Link and ASM International

the Gibbs free energy of the system. With this system, if there is additional gold and the goal is to make a final bond composition that is more gold rich, the temperature must be raised above the 419 °C melting point of δ phase gold-tin in order for the diffusion to progress and run to completion [20]. To get around the issue of terminating the diffusion process at the δ phase, the Au80%wt.-Sn20%wt. eutectic composition can be used in substitution for pure tin. In soldering, the most commonly used gold-tin alloy is the Au80%wt.-Sn20%wt. eutectic solder and it consists of a mixture of the Au_5Sn (ζ') and AuSn (δ) phases. By starting the SLID process with the eutectic alloy on the gold rich side of the phase diagram, it is possible to drive the SLID reaction towards the ζ and β phases and bonding must be performed above 278 °C to liquefy the Au80%wt.-Sn20%wt. alloy. The process of SLID bonding with pure gold and Au80%wt.-Sn20%wt. eutectic solder is shown in Figure 2.3 along with a detailed schematic of the composition of the bond layers in each of the SLID process steps.

2.3 Fabrication Process for Silicon to Silicon Substrate SLID Bonding

An initial investigation was performed to understand the process of SLID Bonding using silicon dies. Silicon, being less expensive than silicon carbide, was deemed a good place to start for understanding the bonding process. Additionally, as outlined in Section 1.3, the bonding of Si to Si using the SLID process to package silicon based MEMS or microelectronics can provide additional freedom to the thermal budget of subsequent processing steps. Using readily available microfabrication techniques in the UC Berkeley Marvell Nanofabrication Laboratory, the bonding of silicon to silicon using thin metal films investigated the feasibility of thin film SLID bonding.

Two prime grade silicon wafers with {1 0 0} crystal orientation and p-type doping with different thin-film metallizations were chosen for bonding to one another. The thicknesses of the metallization are provided in Table 2.1. The metal thin-films were deposited onto the wafers sequentially under continuous vacuum using an Edwards Auto-306 electron beam evaporation tool. Film thicknesses during deposition were monitored using a crystal growth-rate monitor and later verified using scanning electron microscopy.

Table 2.1: The thicknesses used for the metallization of Si substrates in Si to Si SLID Bonding experiments.

Wafer Name	Chromium Adhesion Layer Thickness (nm)	Gold Film Thickness (nm)	Tin Layer Thickness (nm)
TLP3	20	200	250
TLP6	50	275	305

Following film deposition, the wafers were coated with a protective coating of OCG

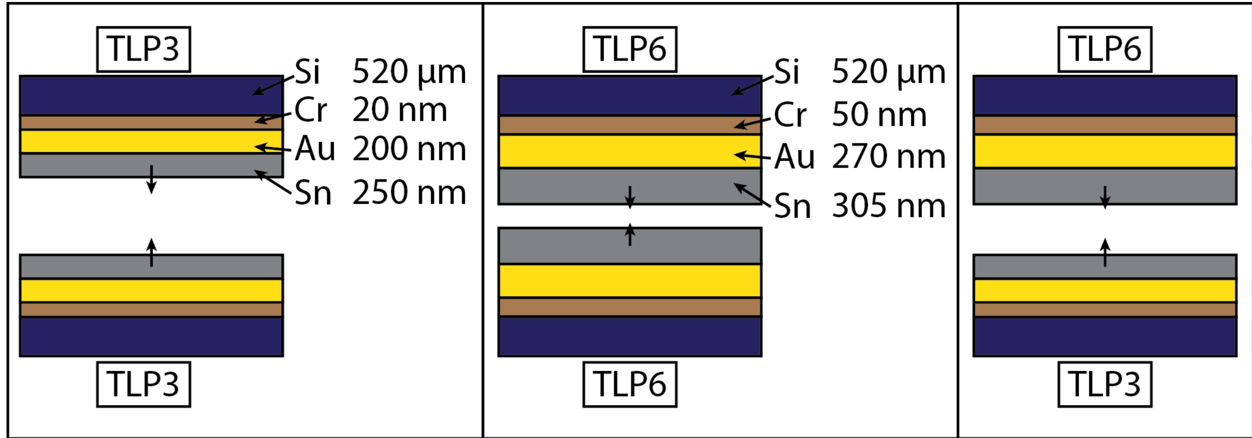

Figure 2.4: Bonding combinations with different metal layer thicknesses used in Si to Si SLID bonding. Three gold-tin metal layer thickness variations were tested: TLP3 to TLP3, TLP6 to TLP 6 and TLP6 to TLP3.

OiR-700 10 i-line Photoresist, 2 µm thick, to protect the evaporated films during the dicing process. A Keteca K3T20L45 dicing blade was used to cut the Si wafers into 1 cm by 2 cm rectangles. A cutting speed of $1.0\,\mathrm{mm\,s^{-1}}$ was chosen to reduce potential chipping of the silicon dies, and a dicing height was selected to cut completely through the bottom of the silicon wafer. The dies were cleaned with acetone, isopropanol, and methanol and dried with an N_2 spray gun. The metalized dies were not dried using a hotplate because the elevated temperatures for drying would initiate the premature diffusion of the gold into the tin film.

For this study, a Yield Engineering Systems vacuum oven was used for the bonding of the Si samples. The samples were placed in contact with one another as shown in Figure 2.4 and a 500 g weight was placed on top of each sample to provide a constant low clamping force during the bonding. The bonding chamber was pumped down to a pressure of 200 torr prior to the start of heating. The heating program ramped the temperature from ambient room temperature, 25 °C, to 350 °C in 1 hour, followed by 30 minutes of dwell at 350 °C and a cooling back down to 25 °C. The cooling of the chamber from 350 °C to 25 °C was very gradual and took 6 hours. The details of the analysis and characterization of the silicon to silicon bonds are discussed in Chapter 4.

2.4 Fabrication Process for Silicon Carbide Substrate to Steel SLID Bonding

The fabrication process for making the SiC to steel SLID bonds was a bit more involved than that for the initial Si to Si SLID bonding investigation; however it consisted of three primary steps: the deposition of gold layers onto the faying surfaces of the substrates being bonded, the selection and placement of the low melting-point metal, and the heating process. This section details the specific process steps that were developed for the fabrication of the silicon carbide to steel SLID bonding process.

2.4.1 The SiC Substrates

For this work, commercially available 4H silicon carbide substrates, (model number: W4NRF0X-0D00), were purchased from Cree. These wafers were 100 mm research grade SiC with nitrogen N-type doping, double-side polished and 523 µm in thickness. Silicon carbide in the 4H polymorph was chosen for this work because of its suitability for use in fabricating silicon carbide electronics for high temperature applications. The silicon carbide wafers are manufactured and cut with one of the polished sides having a carbon-rich face and the other having a silicon-rich face. In this work, the silicon-rich face was used for bonding and the subsequent metal layers and processing was performed on the silicon-rich face.

The deposition of a high-quality seed layer ensures good adhesion of the subsequent metal layers that are deposited onto the Si and SiC substrates. This adhesion is critical for the survival of the bond. E-beam evaporation was chosen as the method to deposit the adhesion layers onto the 4H SiC substrate, using the Edwards Auto-306 electron beam evaporator tool. Prior to deposition the Edwards Auto 306 vacuum chamber housing the e-beam evaporator was purged and vented with nitrogen before pulling vacuum to 5×10^{-6} torr. The purging, in combination with a liquid nitrogen trap, ensured that residual water vapor in the chamber would not interfere with the deposition process and degrade the quality of the films being deposited. During deposition, the film thicknesses were measured using a resonating crystal monitor with a tooling factor of 0.5. This tooling factor was calibrated by measuring the film thicknesses on test wafers using scanning electron microscope.

While several metals such as nickel and chromium are commonly used for adhesion of metal films to Si and SiC, titanium was chosen to be the metal used for the adhesion layer. Gold interacts with Ni and Cr by rapidly diffusing into the Ni or Cr to form intermetallic films and such films have been observed to form during high temperature bonding[60, 61]. With this rapid diffusion, the formation of voids were observed by Tsai and Bohan. Titanium adhesion layers, on the other hand, have been demonstrated to work well with gold films without such drawbacks [62]. Using high purity (99.9 % pure) titanium pellets from Alfa Aesar a titanium adhesion layer of 50 nm in thickness was deposted. Immediately following the deposition of the titanium adhesion layer a 50 nm thick seed layer of gold (99.9 % purity) was also deposited using electron-beam evaporation. Vacuum was not broken between titanium and gold depositions to minimize potential contamination and to ensure good adhesion between the layers.

2.4.2 The Type-316 Stainless Steel Substrate

As the aim of this project is to directly bond silicon carbide dies to stainless steel a fabrication process for electroplating stainless steel dies that could eventually be transferred to locally electroplating large steel components was developed. The work in this dissertation focuses on bonding silicon carbide dies to stainless steel substrates, which could then be joined onto other steel components. For this project, type-316 stainless steel sheets, 762 µm thick, were used as the substrates to which the silicon carbide dies would be bonded. The steel was punched into 1 cm by 1 cm squares in the UC Berkeley Mechanical Engineering Machine shop using a hydraulic press. After punching, the steel was flattened using another press to ensure flatness. The surface of the stainless steel was them mechanically sanded

using 800 grit sandpaper followed by 1200 grit sandpaper to reduce the surface roughness to approximately 5 µm. Following sanding, the stainless steel samples were cleaned with acetone, isopropanol, and methanol.

2.4.3 Electroplating of Soft Gold

Physical vapor deposition techniques, such as evaporation and sputtering, are capable of depositing high purity metal films onto a substrate; however, during thick-film depositions much metal would be spent coating the walls of the evaporation chamber instead of the actual substrate. With precious metals such as gold, such waste would be inexcusable and so electroplating was chosen as the method for the deposition of thick gold films. Electroplating is a cost-effective deposition method and it reduces the amount of wasted metal; however, with electroplating there are added challenges to obtain high quality films with good purity. Electroplating of gold is typically conducted using either direct current (DC) or pulsed current electroplating.

Several gold electroplating chemistries are readily available and these include cyanide-based solutions, acid-based solutions and non-cyanide solutions [63, 64]. Of these plating baths, alkaline cyanide baths are not well suited for use with the photoresists used in semiconductor processing. Alkaline cyanide electroplating solutions have a tendency to attack the photoresist used for patterning the substrate being plated because of their high pH and high concentration of free cyanide. Acidic cyanide baths, while suitable for electroplating with photoresists, can exhibit a tendency to co-deposit cobalt and potassium complexes [65]. Non-cyanide baths can be used as an alternative to toxic cyanide based solutions, however they also introduce issues with stability and plating consistency [66]. Electroless gold plating methods are also available, however, these methods are not well suited for the deposition of thick gold films.

For this work, Technigold 434RTU, a commercially available soft gold and neutral pH electroplating solution, was chosen. Soft gold is pure 24 Carat gold, in contrast with hard bright gold which has added nickel and cobalt to improve hardness and luster. In gold electroplating, the deposition of gold at lower current densities and higher mass transport, from agitation, reduces the porosity of the gold films, however, it also increases the chances of depositing impurities that may be present in the electroplating bath. Higher current densities may be used to reduce the presence of impurities at the tradeoff of increasing metal grain size. The ideal high quality gold film would have small grain sizes and no impurities present.

For the deposition of the soft gold, an electroplating bath setup was built, shown in Figure 2.5. Before using the electroplating tank, the setup was cleaned and leached with sulfuric acid according to the manufacturer's recommendation. The plating setup utilized a hot water bath to heat the electroplating solution in a non-reactive polypropylene container to the temperature of 62 °C, within the manufacturer's recommended range of 60 °C to 65 °C. Temperature of the electroplating solution was monitored using a glass thermometer placed inside the solution. Mechanical agitation of the plating solution to improve mass transport of the electrolyte to the plating work was achieved using a magnetic stirrer. A 5 cm by 5 cm titanium electrode platinized with 125 µm thick platinum cladding was used for the electroplating anode. The lid of the polypropylene container was modified to accommodate

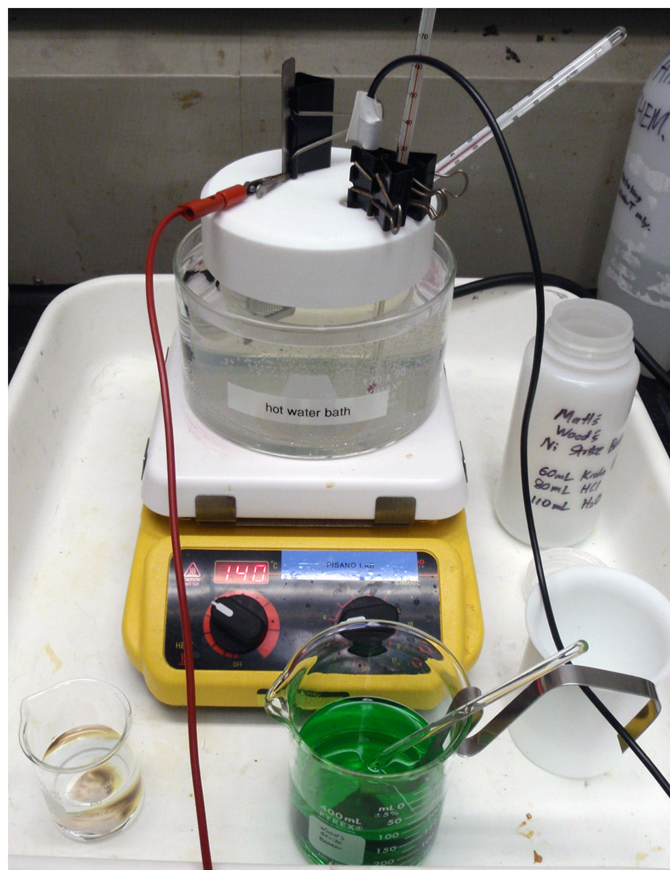

Figure 2.5: The electroplating bath used for depositing gold onto semiconductor substrates and stainless steel substrates. A nickel strike solution, shown in the foreground, was used to improve adhesion of the electroplated gold onto the stainless steel.

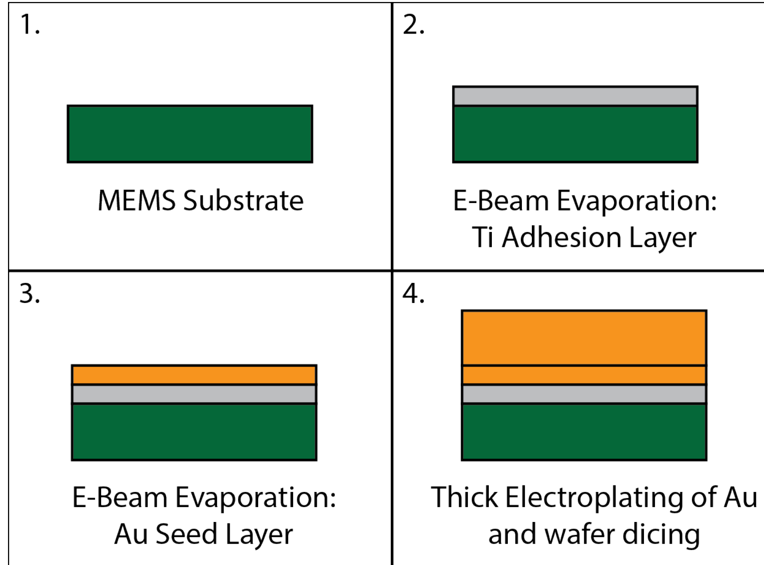

Figure 2.6: The four steps of the fabrication process used to prepare the MEMS substrate for the SLID bonding process.

the placement of the platinized anode and allow for the insertion of a workpiece for plating. The separation between anode and workpiece was set at 5 cm. To monitor the current and voltage used for electroplating, a Keithley 2400 Source-Meter was used to provide the constant-current used for electroplating while measuring the voltage potential. A recommended current density of $0.3\,\frac{\mathrm{A}}{\mathrm{dm}^2}$ was used to electroplate at a deposition rate of $0.19\,\frac{\mu\mathrm{m}}{\mathrm{min}}$. A LabVIEW virtual instrument was programmed to record the voltage potential and current versus time, to monitor the electroplating conditions.

Electroplating on SiC Substrates

The electroplating of the silicon carbide substrates involved two steps, the dicing of the silicon carbide wafer into smaller, more manageable samples, and the electroplating of the substrates in the previously mentioned electroplating bath setup. Following the evaporation of the 50 nm titanium and 50 nm gold seed layers on the 100 mm silicon carbide wafer, the samples were diced. To ensure an anode-to-cathode area ratio of at least 1:1, the silicon carbide wafer was diced into 23 mm by 23 mm squares. Prior to dicing the samples were coated with 2 µm of OCG OiR-700 10 i-line Photoresist to protect the surface of the e-beam evaporated titanium and gold layers.

Dicing of the samples was performed using a Disco DAD 3420 automatic dicing saw. A Dicing Technologies CX-010-270-090-H blade was used for the cutting of silicon carbide samples. A dicing speed of $0.65\,\mathrm{mm\,s^{-1}}$ was used to reduce chipping and scalloping of the edges of the samples. Chips and scallops in the substrate could cause unnecessary stress concentrations that would affect the quality and performance of the subsequent bonds during testing. Following dicing, the samples were cleaned in acetone to remove the protective photoresist, then rinsed with isopropanol, rinsed with methanol, and dried on a hotplate at 110 °C for 3 minutes to remove any residual moisture from the samples.

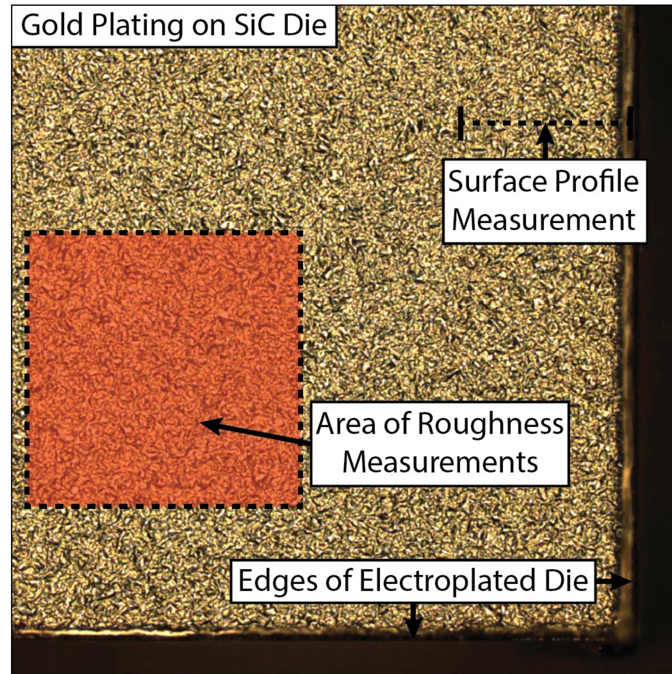

Figure 2.7: Confocal microscopy of the electroplated SiC die as performed to measure uniformity across the surface of the die as well as to measure the thickness of the plated film.

With the silicon carbide samples diced into 23 mm by 23 mm samples and cleaned, these samples were alligator clipped in a corner to make contact with the e-beam evaporated gold seed layer and placed into the electroplating bath. The alligator clip was positioned so that it was not submerged in the plating solution. For the size of the sample, a plating current of 12.55 mA was used to electroplate according to the manufacturer's recommended current density with a rate of 0.19 $\frac{\mu m}{min}$. The duration of time used for electroplating was varied in order to adjust the thickness of the deposited gold films. Electroplating times and the resulting gold film thicknesses are discussed in Chapter 4. Following the electroplating of thick gold onto the silicon carbide squares, the samples were again coated with a 2 µm thick protective coating of OCG OiR-700 10 i-line Photoresist, and diced into 3.8 mm by 3.8 mm squares for bonding with the SLID process. A complete overview of the fabrication process used to prepare the silicon carbide substrates for SLID bonding is shown in 2.6.

After the final dicing of the electroplated into square dies for bonding, the dies were optically inspected using an Olympus LEXT OLS4000 confocal microscope to verify the thickness of the plated gold and the surface uniformity of the plated film, as shown in Figure 2.7. It was found that the film thickness uniformity was good across the die, and the average surface roughness and root mean square roughness were 0.247 µm and 0.331 µm respectively. The skewness and kurtosis of the area was 0.327 and 6.385 respectively. These values show that the surface of the electroplated gold was quite smooth, however there were localized areas that had slight peaks. During the SLID bonding process, the liquid layer formed would dissolve these areas first and the homogenization of the bond would even out the composition of the bond. Additionally, as a result of the final dicing process, there was a slight raise in the gold electroplated film thickness near the edge of the dies. During dicing, it is suspected

that the dicing saw smears the soft pure gold during cutting and causes a slight bulge in the gold film at the edges of the dies. The average raise in film thickness at the edge of the dies was found to be 1.58 µm. Though this raise in height at the edges of the die would cause initial contact at the periphery and initiate diffusion at the edge of the bond, during the SLID bonding processes the liquefied solder would be able to make uniform contact across the bond surface.

Electroplating on Type-316 Stainless Steel

An electroplating process was developed to metalize the type-316 stainless steel with pure gold. With the potential transfer of fabrication process from metalizing 1 cm by 1 cm steel dies to much larger real-world engineering components, a method of locally electroplating the steel was developed. A photolithography process was used to pattern an area on the stainless steel substrate for electroplating. This photoresist would serve as a mask for the subsequent electroplating process, protecting the underlying steel from electroplating. Following the cleaning of the steel samples discussed in Section 2.4.2, the steel samples were coated with a thick layer of Rohm-Hass Megaposit™SPR™220 Photoresist. A manual photoresist spinner was used to coat the steel substrates with 15 µm of photoresist. After coating the backs of the stainless steel samples, the photoresist was hardened by baking on a hotplate at 80 °C for 60 minutes. Following this bake step, the front sides of the stainless steel were manually coated with another 15 µm thick layer of SPR 220 photoresist. A prebake of this new photoresist coating was performed for 300 seconds at 115 °C. A lithography mask with an 31.67 mm^2 opening in the center was used to pattern the opening for electroplating and a Karl Suss MA6 mask aligner was used to expose the prebaked photoresist with a does of 300 $\frac{mJ}{cm^2}$. Following exposure, the samples were allowed to hold in darkness for 120 minutes to ensure proper photo-reaction before performing the post-exposure bake. The post-exposure bake consisted of heating the steel dies to 115 °C for 6.5 minutes and then gently cooling back to room temperature. Rohm-Hass Megaposit™MF™-26A Developer was used to develop the patternedphotoresist. Following this, a final hardbake for 15 minutes at 80 °C was performed to harden the patternedphotoresist in preparation for direct electroplating. The sequence of processing steps is outlined in Figure 2.8.

Electroplating gold directly onto stainless steel is not as straightforward as electroplating it onto metalized silicon carbide substrates. Stainless steel is inherently more resistant to corrosion than ferretic steels because of its higher chromium content, which is capable of forming a passive film of chromium (III) oxide (Cr_2O_3). This thin protective oxide has a relatively low resistance and hence plating layers can form on top of it; however, in terms of adhesion, these plated films exhibit poor adhesion to the native oxide present on stainless steel. Initial electroplating experiments with gold films directly on stainless steel dies revealed poor adhesion. This poor adhesion was characterized using an ASTM adhesion test (D3359-09) of the electroplated gold, as shown in Figure 2.9. Pressure sensitive tape was used to adhere to the gold plated film and in accordance with the ASTM testing standard, the tape was pulled back at an acute angle, as close to 0° as possible, in relation to the surface of the sample. The poor adhesion of the film was characterized by the delamination of the gold from the steel.

To overcome this obstacle in gold film adhesion, a pickling step and a plating strike

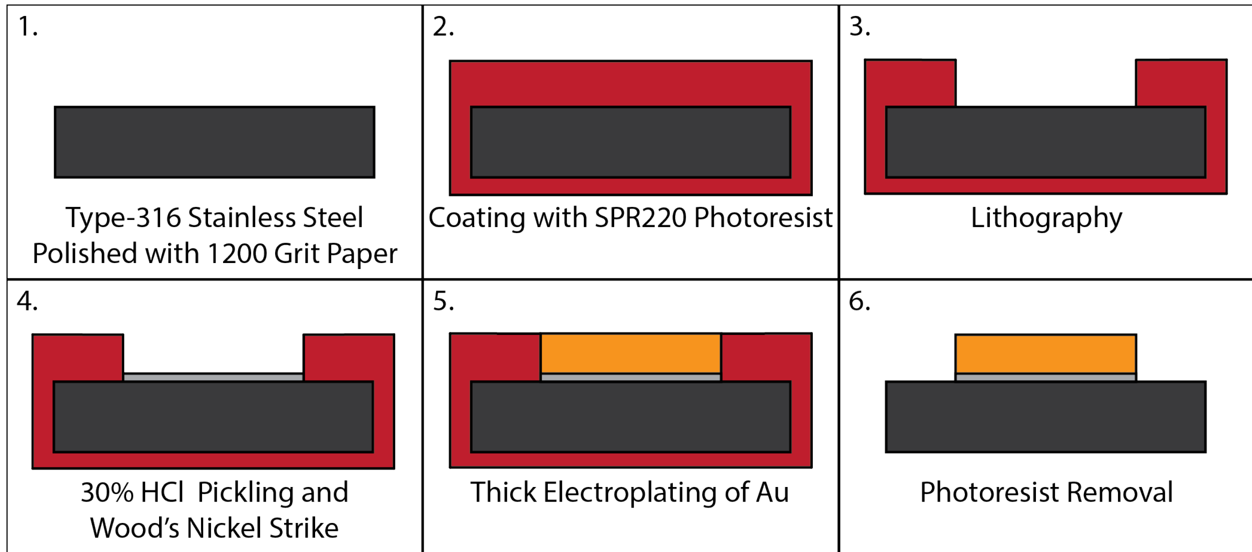

Figure 2.8: The six steps of the fabrication process used to prepare the type-316 stainless steel for the SLID bonding process.

were used to prepare the steel. The pickling of steel consisted of immersing the photoresist patterned stainless steel in 30% hydrochloric acid (HCl) for 60 seconds. This process etches surface oxide that forms on the exposed stainless steel. Immediately after pickling, the steel was connected to an alligator clip and placed in the nickel strike bath, and electroplated. The nickel strike solution consisted of $60\,\mathrm{g\,L^{-1}}$ of commercially available Krohn Nickel Bright Plating Solution and $80\,\mathrm{mL\,L^{-1}}$ HCl. The nickel bright plating solution contained nickel chloride ($NiCl_2$) and nickel sulfate ($NiSO_4$), and the proportion of Krohn Nickel Bright Plating Solution to HCl was determined to have the proper concentration of nickel chloride to HCl as called for in the recipe for Wood's Nickel Strike bath. For the electroplating of stainless steel, Wood's Nickel Strike is a plating solution with low ion concentration that is used in conjunction with high electroplating current densities, to electrodeposit a thin film onto the stainless steel to improve the adherence of subsequent electroplated layers. As studied by Dini *et al.*, following the use of Wood's Nickel Strike or Nickel Sulfamate Strike on stainless steel, adhesion of the plated layers was significantly improved, and maximum bond strengths were achieved when a current density of $1076\,\mathrm{A\,m^{-2}}$ was used [67]. In the nickel strike process used for preparing the stainless steel for the SLID bonding process, a current of 31.67 mA and plating time of 120 seconds were used to deposit the thin nickel layer, of a few nanometers in thickness. This current, given the size of the electroplating area, corresponded to a current density of $1076\,\mathrm{A\,m^{-2}}$. To make electrical contact with the stainless steel sample, the protective photoresist was scratched off in a corner of the die, so that an alligator clip could make direct contact to the steel. The stainless steel was held in place so that only the exposed area for SLID bonding was submerged in the electroplating solution. A stainless steel anode, 1 cm wide and 3 cm long, was used for this strike process and mechanical agitation was provided by stirring with a glass rod.

Following the nickel strike process, the stainless steel was rinsed in deionized water before immersion in the gold electroplating bath. Gold electroplating was performed in the same

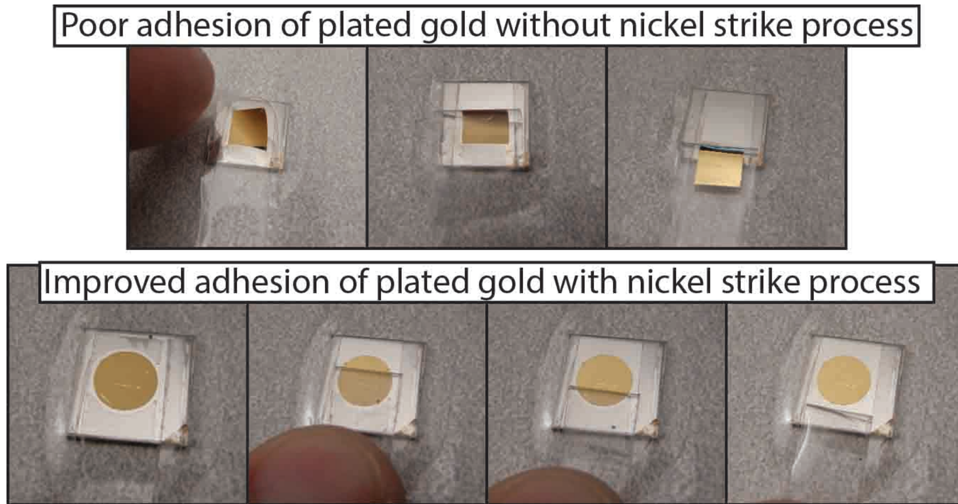

Figure 2.9: Adhesion testing was performed on the electroplated gold films. In the electroplating of the sample shown in the top row, the HCl pickling and nickel strike steps were omitted. From left to right, the progression of the ASTM D3359-09 testing is shown. For the sample shown in the bottom row, both HCl pickling and nickel strike steps were used. From left to right, the adhesion test shows significant improvement of adhesion.

electroplating setup used for electroplating the silicon carbide substrates. Thorough rinsing in the deionized water would help to reduce the likelihood of contaminating the gold plating bath. For the plating of gold films on the stainless steel, a current of 1.2 mA, with a current density of $0.37\,\frac{\mathrm{A}}{\mathrm{dm}^2}$. The electroplating times were varied to change the thickness of the films.

Following electroplating, the deposited gold films on the stainless steel were characterized using an Olympus LEXT OLS4000 confocal microscope. Step heights and surface roughness measurements of the films were made as shown in Figure 2.10. For these gold films plated on stainless steel, the averaged root mean square roughnesses and the average roughnesses for the electroplated samples were 0.310 µm and 0.229 µm respectively. The average skewwness and kurtosis were 0.5815 and 7.647 respectively. As a result the topography of the electroplated gold films on stainless steel were quite similar to the films deposited onto the silicon carbide substrates.

2.4.4 Selection and Preparation of Low Melting-Point Metal

With the gold-tin material system chosen for SLID bonding, and the selection of Au80%wt.-Sn20%wt. eutectic solder as the chosen melting point depressant, solder preforms were obtained for bonding. Preforms in sizes 1 cm by 1 cm by 5 µm and 1 cm by 1 cm by 12.7 µm were purchased from AMETEK. For SLID bonding, the preforms were cut into 5 mm by 5 mm squares using scissors. These preforms were cut larger than the silicon carbide dies, so that full contact across the bonding area would be ensured when the bonding stacks were assembled. As later discussed in Section 3.1, the choice of eutectic solder preform thickness dictates the final composition of the SLID bond.

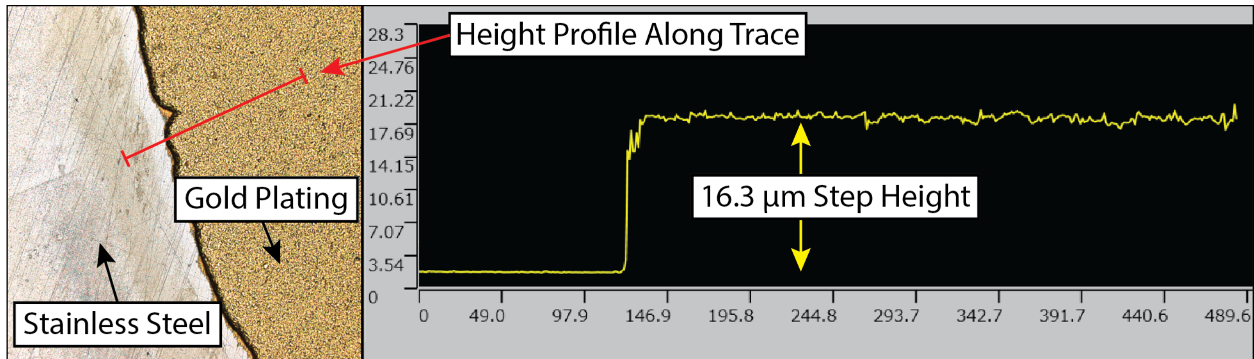

Figure 2.10: Confocal microscopy was performed to measure the step height and the surface profile of the gold electroplating film on the stainless steel substrate after the electroplating process. On the left, an 20× microscope image shows the gold electroplated steel and on the right, the step profile measured along the trace is provide.

2.4.5 Heating Process for SLID Bonding

The heating process for the SLID bonding consists of heating the bond to a temperature above the melting point of the eutectic alloy, in the case of this bonding research, the Au80%wt.-Sn20%wt. alloy. The bonding process also requires that the temperature be held constant while the bond isothermally solidifies and homogenizes. To perform these steps, a bonding setup was designed and fabricated.

In the heating process there are several factors of key importance: the heating rate of the samples, the duration of the applied heating, and the environmental conditions of the bonding chamber. The heating rate of the bond must be high enough to ensure that melting of the eutectic layer and resolidification of the generated intermetallics do not happen at temperatures much lower than the desired bonding temperature. If solid state diffusion and non-uniform solid-liquid interdiffusion occur too soon and form high melting point intermetallics, voids can be left behind in the bonding layer [68]. These voids, known as Kirkendall Voids, are a result of differences in diffusion rates of metals.

In this work various heating rates were tested and the best compromise between thermally shocking the materials in the bond and accomplishing a good bond was found to be a heating rate of 50 °C min^{-1} to bring the bond from room temperature, 25 °C, to the bonding temperature of 300 °C. The bonding time used for the bonding of silicon carbide to steel was chosen to be 12 minutes. As reported by Tollefsen *et al.* in his studies of SLID bonding with the gold-tin material system, good bond strengths were achieved with a bonding temperature of at least 300 °C and a bonding time of at least 6 minutes. Increasing the bonding temperature and bond times beyond that showed no significant improvment of bond strenghth [56].

The construction of the heater setup is in Figure 2.11. Two stainless steel ConFlat vacuum flanges were machined and modified to fit the resistive heater and hold the samples in place for bonding during the heating process. The base of the heater was machined to fit two insulating ceramic disks that would help hold the generated heat in and prevent excessive conduction from the resistive heater to the bonding setup and bonding chamber. The ceramic chosen for this was a low thermal conductivity alumina silicate ceramic. On

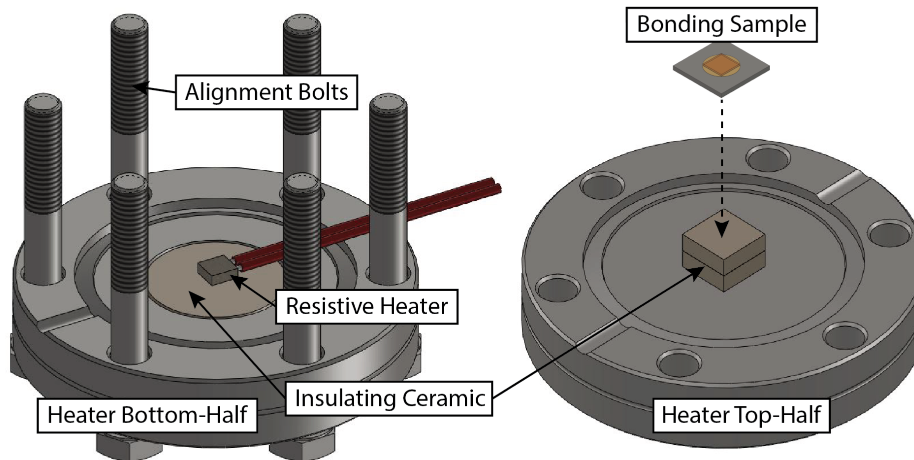

Figure 2.11: Schematic of the top and bottom halves of the bonding setup.

the top half of the heater, these low conductivity ceramics were also placed to thermally isolate the bonding samples and prevent excessive heat escape to the bonding setup. On the top surface of these ceramic blocks, a K-type thermocouple was mounted to monitor the temperature at that location in the bonding stack. The temperature response of the system to different voltage inputs to the heater was characterized and it was calibrated so that a repeatable 300 °C bonding temperature, ±5 °C, could be obtained by following the heating schedule.

To place the gold-metalized silicon carbide, Au80%wt.-Sn20%wt. solder preform and gold-metalized stainless steel substrate for bonding, the top half of the heater setup was placed flat. The stainless steel was first placed on the insulating ceramic layer, followed by the solder preform and the silicon carbide die. The electroplated gold layers of the silicon carbide and stainless steel were placed in direct contact with the solder preform. Alignment of the edge of the silicon carbide die and the edge of the stainless steel was performed visually. After alignment of the bonding layers, the base of the heating jig, with the resistive heater in place, was turned upside down and placed onto the top half of the heating jig, sandwiching the layers of the bond in place and in direct contact with the heater. Six hex-cap bolts were used as alignment pins to mate the top half of the heater setup to the bottom half, and to allow for additional weight, in the form of an additional ConFlat vacuum flange, to be added for increased bonding pressure. Figure 2.12 shows the fabricated components of the heater and the assembled setup in operation.

Once the layers were brought into contact and alignment of the heater with the silicon carbide die was confirmed, the assembly was brought into contact and the entire assembly was inverted so that the top half was on top and the bottom half was on the bottom. With the additional ConFlat flange in place, the total weight pushing down on the bond was 720 g, equivalent to a 49.86 kPa bonding pressure distributed evenly across the 3.8 mm by 3.8 mm bond area. During bonding, an additional K-type thermocouple was used to probe the silicon carbide die and the stainless steel substrate and measure the temperature of the bonding process at the location of the bond. A Stanford Research SR630 Thermocouple reader was used to monitor the temperatures measured by the thermocouples using a LabVIEW virtual

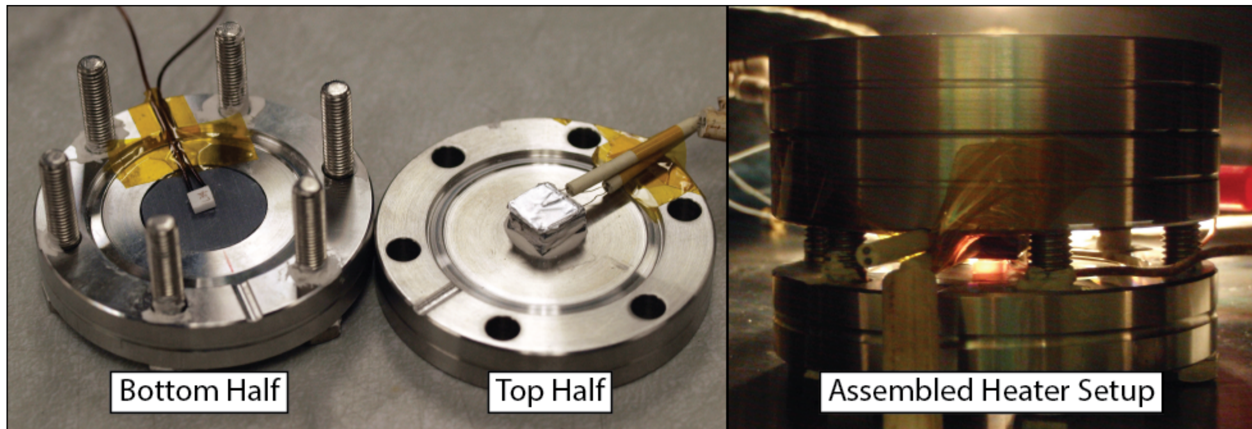

Figure 2.12: The assembled bonding setup in operation.

instrument.

In this study a 5 mm by 5 mm Sakaguchi E.H Voc Corp. MS-M1000 micro ceramic heater was used to heat the samples to the bonding temperature. A Hewlett Packard 6263B DC power supply with a 0 V to 20 V and 0 A to 10 A limit was used to provide power to the resistive heater. To heat the sample, the Power supply was operated in a voltage limited mode and voltage was increased from 0 V to 8.5 V according to a calibrated heating-time schedule. During the raising of the voltage, the current draw from the heater was an almost constant 1.2 A. The heating-time schedule for the bonding is provided in Appendix B in Section B.4. Figure 2.13 shows the heating profile obtained when following the developed heating recipe with the resistive heater and power supply.

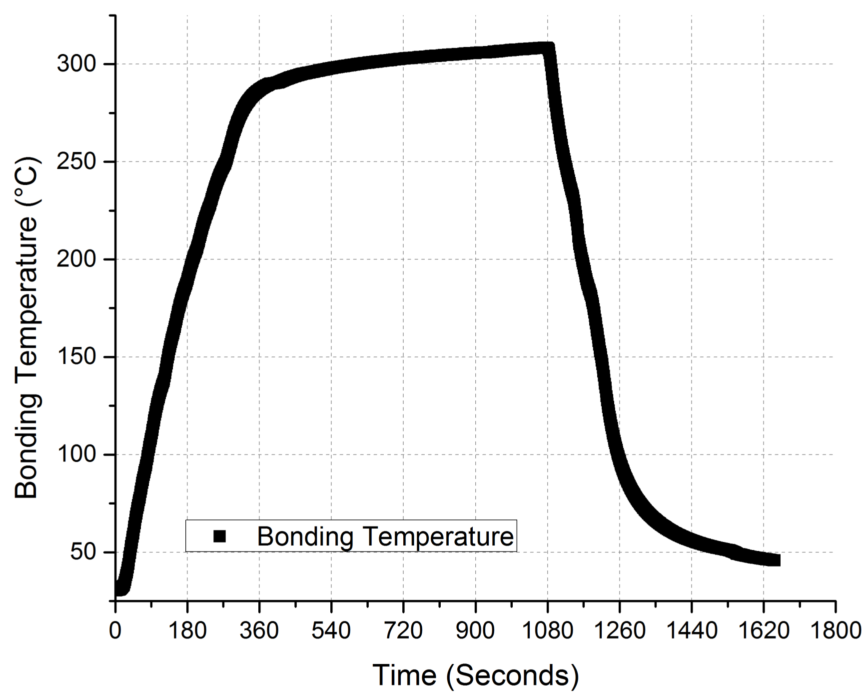

Figure 2.13: The temperature profile of the SLID Bond interface versus time, using the vacuum chamber heating setup.

Chapter 3

Design and Theory of SLID Bonds for High Temperatures Applications

As described in Chapter 2, to achieve the desired SLID bond and to have the proper alloy composition for the desired melting point, the thicknesses of the SLID bond must be carefully tailored. In addition to the adjusting the metallurgical composition of the bond in order to achieve a high enough melting point for successful bonding, the mechanical properties of the different layers of the bond must also be considered to ensure proper bond survival. In this chapter, the theory and reasoning behind the layer thicknesses of the SLID bond are discussed. Additionally, the analytical calculations and the finite element analysis models that were used to support the design of the SLID bond are presented.

3.1 Tailoring the Thicknesses of the SLID Bond Layer

The amount of gold and tin present in the layers of the bond dictate the bond's final composition after the SLID bonding process is performed. The phase diagram of the gold-tin system, covered in Section 2.2, provides a roadmap for what intermetallic alloys will be formed depending on the quantities of materials present during bonding. To predict the composition of the silicon to silicon SLID bonds and the silicon carbide to stainless steel SLID bonds calculations were performed based on the atomic composition of the films used in SLID bonding and the thicknesses of the films. For the silicon to silicon SLID bonds, composition calculations were performed for different thickness layers of electron beam evaporated gold and tin thin films. For the silicon carbide to steel SLID bonds, based on the two different thicknesses of commercially available Au80%wt.-Sn20%wt. eutectic preforms, calculations using different thicknesses of gold electroplating were performed to determine how much gold would be required to form the high melting point intermetallics and how much excess gold would remain. In addition to determining the composition of the bond after diffusion, the layer thicknesses play an important role in the mechanical transfer of stresses and thermally induced strains in the bond. Varying the thicknesses of the different layers shifts the neutral stress axis in the system and alters the distribution of in-plane stresses through the bond [69].

3.1.1 Layer Thicknesses in Silicon to Silicon SLID Bonding

For the initial investigation of SLID bonding with silicon dies using pure layers of electron beam evaporated gold and tin, Equation 3.1 was used to determine the atomic percentage of gold and tin present in the bond. In the equation, t is the thickness of the layers, ρ is the density of the of materials and M is the molar mass of the materials. For the silicon to silicon bonding samples discussed in Section 2.3, for the TLP 6 to TLP 6 wafer the total composition of the bond layers would be 64.5%at. and for the bonding of TLP 3 to TLP 3 the composition would be 61.7%at.

$$\%at.\text{Gold} = \frac{t_{Gold}\rho_{Gold}/M_{Gold}}{t_{Gold}\rho_{Gold}/M_{Gold} + t_{Tin}\rho_{Tin}/M_{Tin}} \tag{3.1}$$

Based on these calculated bonding compositions and the gold-tin phase diagram, it is evident that the amount of gold evaporated on the TLP 3 and TLP 6 samples would not be great enough to generate the β or ζ gold-tin phases; however the δ and ϵ phases of gold-tin could be formed, raising the melting temperature from the melting point of pure tin, 231.96 °C to 311 °C for the ϵ phase and 419 °C for the δ phase. Rearranging the calculation and solving for how much thicker the e-beam evaporated gold layer should be compared to the e-beam evaporated tin layer in order to form the ζ phase composition, it is found that the gold layer must be at least 3.05 times thicker than the tin layer.

3.1.2 Layer Thicknesses in Silicon Carbide to Steel SLID Bonding

For the bonding of silicon carbide to steel, the layer thicknesses of the electroplated gold on the silicon carbide and stainless steel components as well as the thickness of the Au80%wt.-Sn20%wt. eutectic solder determine the composition of the final bond. With gold-tin SLID bonding, the β and ζ phases are preferred for high temperature applications and to obtain those phases in bonding the proper layer thicknesses of the bonding layers must be used. At the expected 375 °C operating temperatures of geothermal wells, the β phase of gold-tin consists of between 5%at. to 8%at. tin while the ζ phase consists of between 10%at. to 14%at. tin.

In the bonding process, diffusion begins at the boundary of the eutectic solder preform and the pure gold and continues outwards through the silicon carbide and steel metalization layers. If the layers of the pure gold are thicker than what is required to form the ζ or β phase, the remainder will stay pure gold after the intermetallic phases homogenize. This pure gold serves an important role as a buffer material that can aid in the absorbing of thermally induced strains and relieve stresses in the bond through plastic deformation. To calculate how much gold is consumed by solid-liquid interdiffusion reaction when bonding with the 5 µm or 12.7 µm thick preforms the atomic ratios and layer thicknesses were computed. For the calculation it was assumed that the diffusion reaction would propagate equally from the center of the bond formation and the excess gold would be left above and below.

To calculate how much gold and tin was present in the SLID bonding system Equation 3.1 was reorganized to determine the effective thicknesses of pure tin and pure gold present in the solder preforms. Additionally, the fact that the effective thickness of pure gold and the effective thickness of pure tin present in the solder preform would add up to the total

thickness of the solder was used to develop a system of two equations and two unknowns to determine the thicknesses of gold and tin present, as shown in Equations 3.2 and 3.3.

$$(\%\text{at.Gold} - 1)\frac{t_{Gold}\rho_{Gold}}{M_{Gold}} + (\%\text{at.Gold})\frac{t_{Tin}\rho_{Tin}}{M_{Tin}} = 0 \tag{3.2}$$

$$t_{Gold} + t_{Tin} = t_{PreformThickness} \tag{3.3}$$

The atomic percentage composition of the Au80%wt.-Sn20%wt. eutectic solder is 70.7%at. gold and 29.3%at. tin. Using this information, for the 5 µm thick solder preform the equivalent film thicknesses of pure tin and pure gold are 2.276 µm and 2.724 µm respectively. For the 12.7 µm thick preform, there is an equivalent 5.781 µm of pure tin and 6.919 µm of pure gold. With the equivalent compositions of pure tin and gold in the preform known, it can be further calculated to see how much additional pure gold from the electroplated layers would be required to form the ζ and β phases.

With the effective layer thicknesses of pure tin in the preforms, it is possible to determine how much additional pure gold would be consumed in making the ζ and β phases. For the case of the 5 µm thick eutectic preform, a total gold layer of 6.934 µm thickness would be required to form the ζ phase intermetallic, and for the β phase intermetallic it would take 12.981 µm. In addition to the gold already in the solder preform, an additional 4.21 µm thick layer of gold from the electroplated gold layers on the steel and silicon carbide would diffuse to form ζ phase gold-tin and an additional 10.257 µm of gold would be required for the β phase gold tin intermetallic. For the 12.7 µm eutectic preform, to form the ζ phase and β phase intermetallics it would require 17.612 µm and 32.972 µm thick layers of pure gold, respectively. In addition to the gold already present in the 12.7 µm preform, it would require 10.693 µm and 26.053 µm of gold from the electroplated layers to form the ζ and β phases of gold tin. It is apparent from these calculations that a large amount of pure gold is required to form these gold-rich intermetallic compounds. Additionally, if the electroplated gold layer thickness is not large enough on the silicon carbide or steel side, then the diffusion of the tin will reach the silicon carbide or steel. The choice of electroplating layer thickness should be made to ensure enough gold is present on either side of the bond.

3.2 Analytical Modeling of Thermally Induced Strains

To calculate and understand the thermally induced stresses encountered by bonding the SiC samples to steel, an analytical model was created to determine the in-plane stresses occurring at different locations of the bonding stack as a result of bonding the SiC dies to stainless steel. The analysis, developed by Hall *et al.* and based upon the works published by Timoshenko and Goodier, was used to determine the amount of in-plane stresses present in the different layers of the bond. These in-plane stresses arise from the differences in thermal expansion of the various materials present. With the SLID bonding process, it is assumed that since the bond is formed isothermally at the bonding temperature of 300 °C, no thermally induced strains are present in the bonding stack. When cooling or heating the sample to temperatures away from the bonding temperature, however, thermally induced strains are developed.

For the analysis of the films, the layers of the bond that were considered were the silicon carbide die, the excess gold layer of the silicon carbide die, the ζ phase gold-tin, the excess gold layer on the stainless steel and the stainless steel substrate, as shown in Figure 3.1. The thicknesses of the layers used in this analysis were taken from the physical thickness dimensions of the silicon carbide and steel components. Based on the calculations of layer composition in Section 3.1.2, it was assumed that the thickness of the excess gold left on the silicon carbide and steel substrates from the electroplating process would be 14.5 µm and the thickness of the formed ζ' phase gold-tin would be 11 µm in thickness. In this investigation, the ζ' gold-tin intermetallic was considered for the intermetallic present in the SLID bond layer because at that atomic composition of gold-tin it is the phase that is stable below 190 °C. At temperatures above 190 °C the ζ' phase of gold-tin changes to the ζ phase.

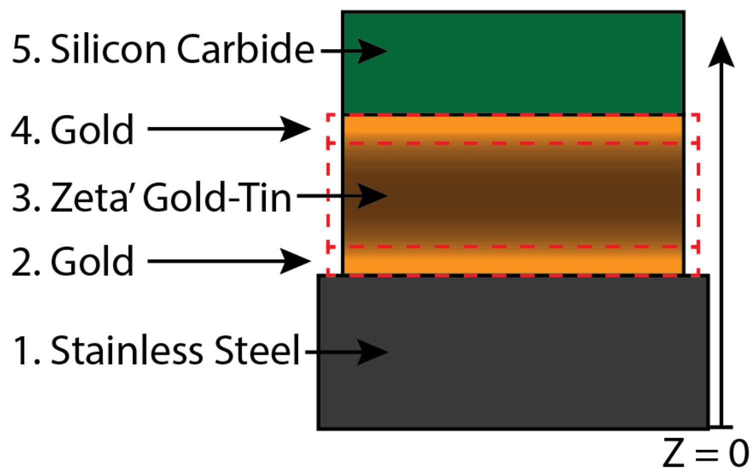

Figure 3.1: The analytical analysis of the thermally induced strains incorporated properties of the materials comprising the SLID bonding stack. The bonding stack consists of the stainless steel substrate, a gold layer, a ζ' gold-tin layer, another gold layer, and the silicon carbide substrate.

Material properties including the Young's modulus of elasticity and coefficients of thermal expansion were tabulated from literature for the steel, gold, ζ phase gold-tin and 4H SiC as shown in Table 3.1 [70, 71]. The values of these properties are tabulated in Table 3.1 for the various materials used in the SLID bond. For the analytical analysis, the Elastic Modulus, the Poisson's Ratio and the coefficient of thermal expansion were used to perform the calculations.

Table 3.1: The material properties of the silicon carbide to steel SLID bond components used for the analytical analysis and finite element analysis. (For the ANSYS material properties macro, refer to Section A.4).

	4H-SiC [72]	Type-316 Stainless Steel [73]	Au	β Gold-Tin $Au_{10}Sn$ [44, 74]	ζ' Gold-Tin Au_5Sn [44, 74, 75]	ζ Gold-Tin $Au_{0.85}Sn_{0.15}$ [44, 74, 75]
Melting Point (°C)	2700	1371	1064	532	-	522
Density ($g\,cm^{-3}$)	3.2	7.99	19.32	-	16.3	-
CTE (ppm/K)	3.21	15.7	14.4	-	18.0	20.0
Young's Modulus (GPa)	340	193	77.2	88	69	58
Shear Modulus (GPa)	130.8	82	27.2	33.1	22	20
Poisson's ratio	0.3	0.3	0.42	0.33	0.4	0.4

The analytical model used in this investigation utilizes the general equations and relations of stress and strain with the inclusion of strains arising from thermal expansion mismatch. The model assumes that the in-plane stresses are a linear function of vertical position, z, in the bond stack, and are independent of their position in plane. It is assumed that the total deflections encountered from the bending or curving of the bond layers are no larger than the overall thickness of the bond stack. Lastly, it is assumed that the system behaves uniformly in the plane of the structure, perpendicular to the vertical z-position in the bond. The bond is assumed to behave uniformly in the x and y directions and the materials are assumed to behave isotropically in-plane, reducing this analysis to a one-dimensional analysis.

For the analytical analysis of thermal strains, the general equation used to relate stress and strain, with the inclusion of thermal expansion is given by Equation 3.4. This equation shows that the total strain present is a combination of the thermally induced strains as well as the stress-induced strain. In this equation ϵ is the strain, σ is the in-plane stress, α is the coefficient of thermal expansion, E and ν are the elastic modulus and Poisson's ratio respectively, and ΔT is the change in temperature.

$$\epsilon = \alpha\Delta\mathrm{T} + \frac{\sigma(1-\nu)}{\mathrm{E}} \tag{3.4}$$

From the assumption that the strains are a linear function of vertical position, z, an equation for strain can be formed in terms of strain present at the top of the entire bonding stack at the top of the silicon carbide substrate, ϵ_T, and the strain present at the bottom of the bonding stack on the bottom surface of the stainless steel substrate, ϵ_B. Equation 3.5 shows this relation of strain as a function of ϵ_B and ϵ_T. In this equation the term h is the total thickness of the bonding stack from the bottom of the steel to the top of the silicon carbide.

$$\epsilon = \epsilon_B + \frac{z}{h}(\epsilon_T - \epsilon_B) \tag{3.5}$$

Equation 3.4 holds for each layer present in the bonding stack and so Equations 3.4 and 3.5 can be combined to form a stress-train relation, presented in Equation 3.6, in terms of the aforementioned parameters and material properties where the subscript, i, corresponds to the i-th layer of the bonding stack, as shown in Figure 3.1.

$$\sigma = \frac{E_i}{1-\nu_i}\left[(1-\frac{z}{h})\epsilon_B + \frac{z}{h}\epsilon_T - \alpha_i\Delta T\right] \tag{3.6}$$

In this equation, the values of ϵ_T and ϵ_B are not initially known. By using the known material properties and establishing two relations for the radial force component and the moment the values for the strains at the top and bottom of the bonding stack can be determined. These two relations, given in Equations 3.7 and 3.8 respectively, provide an equation for the radial force and moment in the i-th layer of the bonding stack. In these equations the limits of integration z_i and z_{i-1} correspond to the position at the top of the i-th layer and the position at the bottom of the i-th layer respectively. For the bottom-most layer, $z_{i-1} = 0$.

$$P_i = \int_{z_{i-1}}^{z_i} \sigma \, \mathrm{d}z \tag{3.7}$$

$$M_i = \int_{z_{i-1}}^{z_i} z\sigma \, \mathrm{d}z \tag{3.8}$$

Expanding these two equations for the radial force and moment by substituting the stress relation from Equation 3.6 produces the following two expanded equations, Equation 3.9 and 3.10.

$$P_i = \frac{E_i}{1-\nu_i}\left[(\epsilon_B - \alpha_i \Delta \mathrm{T})(z_i - z_{i-1}) + \frac{1}{2h}(\epsilon_T - \epsilon_B)({z_i}^2 - {z_{i-1}}^2)\right] \tag{3.9}$$

$$M_i = \frac{E_i}{1-\nu_i}\left[\frac{1}{2}(\epsilon_B - \alpha_i \Delta \mathrm{T})({z_i}^2 - {z_{i-1}}^2) + \frac{1}{3h}(\epsilon_T - \epsilon_B)({z_i}^3 - {z_{i-1}}^3)\right] \tag{3.10}$$

In these two equations, the two unknowns are ϵ_B and ϵ_T, and to solve for their values and to calculate the stresses and strains in each layer, two boundary conditions are required. With no external forces or moments applied to the system, it can be shown that the sum of forces and the sum of moments are equal to zero, as shown in Equations 3.11 and 3.12.

$$\sum_{i=1}^{n} P_i = 0 \tag{3.11}$$

$$\sum_{i=1}^{n} M_i = 0 \tag{3.12}$$

These two boundary conditions allow for Equations 3.9 and 3.10 to be solved for ϵ_B and ϵ_T. The calculation requires quite a bit of arithmetic and introducing variables for the terms that sum up through the i-layers of the material stack to simplify the system of equations. The MATLAB script used to perform these calculations is provided in Appendix A in Section A.2, as well as in Hall's work on, and the details of these constructed variables are presented there [70]. With the determination of ϵ_B and ϵ_T, the radius of curvature of the entire bonding stack can be calculated using Equation 3.13.

$$\frac{1}{\rho} = \frac{\epsilon_T - \epsilon_B}{h} \tag{3.13}$$

Additionally, using the radius of curvature, the deflection of the center of the material stack was calculated using Equation 3.14, where R is the radius of a cylindrical material stack from the center of the stack to the edge. For the analysis to be valid, the deflection of the center of the material stack should not be on the same order of magnitude as the entire thickness of the stack. In the analysis, the radius of this cylindrical bonding stack was assumed to be 2.5 mm

$$\delta = \frac{R^2}{2\rho} \tag{3.14}$$

Table 3.2: The calculated maximum and minimum in-plane stresses from the Analytical Model in each layer of the SLID bond are presented here for the cases of initially cooling the bond down from 300 °C to 25 °C and heating the bond past 300 °C to 375 °C.

Stresses Given in (MPa)	Layer 1: Stainless Steel	Layer 2: Gold	Layer 3: ζ' Gold-Tin	Layer 4: Gold	Layer 5: Silicon Carbide
Max. Stress from Cooling	447.3	180.9	305.2	192.6	405.6
Min. Stress from Cooling	-229.4	174.3	300.4	185.9	-758.2
Max. Stress from Heating	625.6	-47.5	-81.9	-50.7	206.8
Min. Stress from Heating	-122	-49.3	-83.2	-52.5	-110.6

Performing the analytical analysis of thermal strains with the aforementioned bonding stack thicknesses and material properties, it was found that for the cooling of the stack from the bonding temperature of 300 °C to 25 °C, ϵ_T was found to be -799×10^{-6} and ϵ_B was found to be -5.2×10^{-3}. Using the equations for the radius of curvature, ρ, was found to be 0.298 m. The deflection, δ, was calculated to be 10.5 µm, which is 0.8 % of the total thickness of the assembly, ensuring that the analytical model was not invalid. The in-plane stresses in the bonding stack were calculated using the strain values at the top and bottom of the stack and the results are plotted in Figure 3.2.

For the case of heating of the bond to the operating temperature of 375 °C, a ΔT of 75 °C, the calculations were performed again and the values for in-plane stress were also plotted in Figure 3.2. For the heating case, the strain at the bottom of the material stack was found to be 1.43×10^{-3} and the strain at the top of the stack was found to be 218.0×10^{-6}. The radius of curvature was found to be -1.09 m and the deflection was found to be -2.86 µm. The results for the in-plane stresses from heating the bond are plotted in Figure 3.2 and the maximum and minimum stresses for the cooling and heating case are presented in Table

Upon analyzing the stresses generated from the cooling and heating of the bonding stack away from the bonding temperature, it is apparent that significant stresses are induced in the layers. First of all, it is noted that although the stresses in the silicon carbide and steel layers are quite significant, they are within the ultimate strength limitations of the materials. The magnitude of the induced stresses in the layers of the bond is much greater for the cooling process in comparison to the heating process and this is simply due to the change in temperature when heating being about 27 % that of the cooling ΔT. The analytical simulation was carried out with different thicknesses of the layers to determine the effect of varying layer sizes. It was found that varying the thicknesses of the silicon carbide and steel had the most impact on the distribution of stresses in the layers of the bond.

When thinning the silicon carbide substrate from 500 µm to 300 µm, but keeping the rest of the layer thicknesses constant, there was a significant reduction in the stress in the silicon carbide layer. The maximum stress in the silicon carbide layer decreased by 296 MPa and

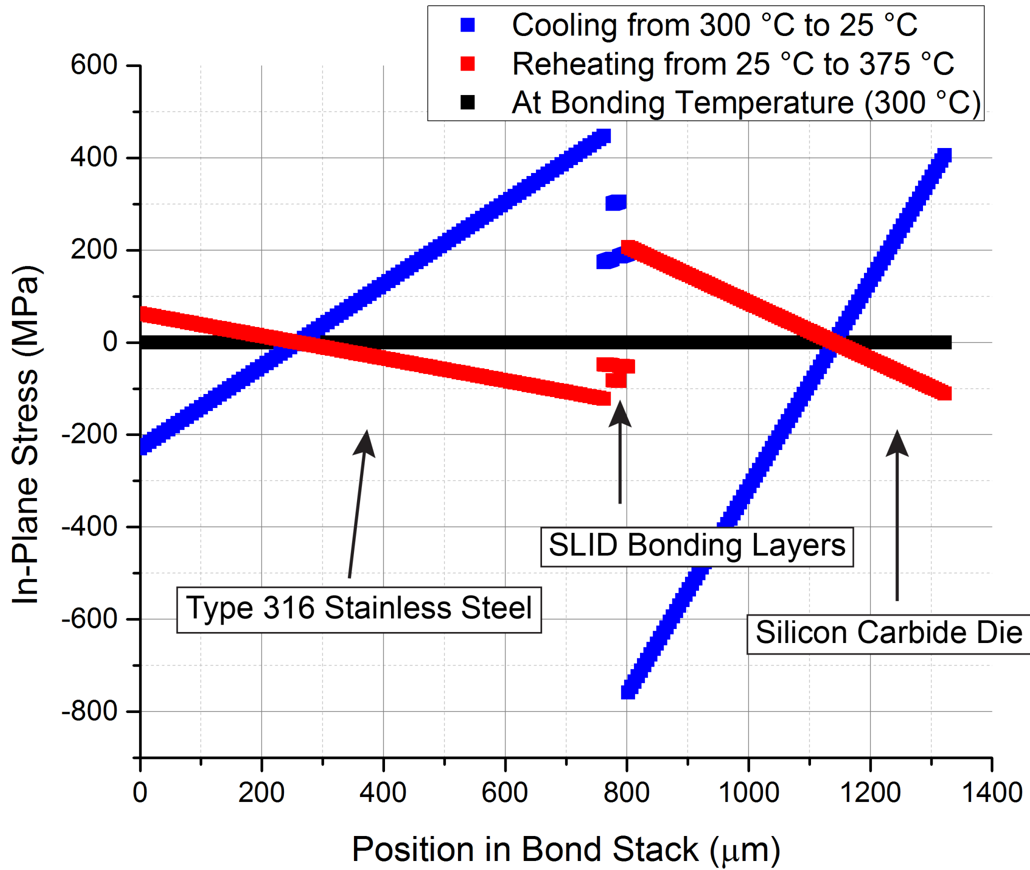

Figure 3.2: The in-plane thermal stresses analytically calculated as a function of position in the bond stack, starting from the bottom of the steel and moving upwards to the top surface of the SiC die. The cases of cooling the bond and reheating the bond are shown. At the bonding temperature of 300 °C the system is at equilibrium so no thermal stresses are induced.

the minimum stress also relaxed by 100 MPa. The stresses in the steel substrate; however, increased significantly. Conversely, with the original bonding layer thicknesses and original silicon carbide thickness but with the thickness of the stainless steel increased from 762 µm to 3 cm, compressive stresses were calculated to be about 1.67 GPa, a significant increase, in the silicon carbide layer when cooling and the stresses in the stainless steel layer relaxed.

Increasing the thickness of the gold layers and the ζ' gold-tin layer formed during SLID bonding causes the thermally induced stresses in them to increase, while reducing the magnitude of stresses in the silicon carbide and steel layers. However, the thicknesses of the gold layers must approach 50 µm to 100 µm and the thickness of the formed ζ' gold-tin layer would have to increase between 50 µm to 150 µm in order for adequate reduction of stresses in the silicon carbide and steel layers.

The analytical model presented here did not account for the effects of plasticity, and so

due to yielding and plastic deformation, the stresses encountered in the layers of the bond should be reduced. Additionally, the bond geometry assumed in the study was that of radial disks of the bonding materials stacked on top of one another; effects of stress concentrations and non-uniform geometries were not analyzed in this analytical model. To account for these geometries and the effects of plasticity, an improved model would be required. However, from the simplistic model it is clear that the thickness of the steel substrate can easily dominate the stress effects encountered in the bond. By thinning the silicon carbide die, it is possible to reduce the in-plane stresses in the silicon carbide, but the stresses in the steel component will increase. Tailoring the thicknesses of the layers causes great changes in the stress state of the bond.

3.3 Computer Modeling of Thermally Induced Strains

To investigate the stresses induced in the SLID bond, from the thermal expansion mismatch between the silicon carbide and steel components and to include the geometries of the bonding stack, a finite element analysis ANSYS 14.0 model was created to simulate the thermal strains. The model simulated the stresses induced when cooling th SLID bonding stack from the bonding temperature of 300 °C to room temperature, 25 °C, and then bringing the sample back up to the operating temperature of 375 °C which would be encountered in geothermal environments, as was performed in the analytical calculation model in Section 3.2. It was assumed that since the bond was fabricated at 300 °C, that the system would be at mechanical equilibrium and free of induced thermal strains.

Material properties for the different materials present in the bond were taken from experimental values reported in literature and were reported in Table 3.1. For the Au80%wt.-Sn20%wt. alloy and ζ-phase gold-tin alloy the material properties found in literature, such as the yield strength and Young's Modulus, were determined from microindentation testing [76]. For the type-316 stainless steel, material properties were taken from the ASM International Atlas of Stress-Strain Curves [77]. To include the effects of plasticity, for the material properties of the gold and stainless steel, a bilinear kinematic hardening option was used in the ANSYS model. This option takes into consideration the yield stress of the material and

For the simulation, one quarter of the bond was modeled and symmetry constraints were applied to the boundaries to simplify the model and reduce the number of required calculations necessary for the simulation. Along these boundaries, the displacement degree of freedom allowing the nodes to pass through the plane was fixed. The geometry of the materials in the bonding stack were based off the physical dimensions of the silicon carbide and steel samples, and the layer thicknesses of the SLID bonding layers were based off observations made in initial experiments. In these geometries, the quarter of the silicon carbide die was given a thickness of 520 µm, a width and length of 1.9 mm. The type-316 stainless steel was modeled with a thickness of 762 µm and a width and length of 5 mm. In the SLID layer, it was simulated that an excess layer of pure gold, 15 µm in thickness, would be present and in contact with both silicon carbide and steel substrates after the SLID bond process was completed. In between these pure gold layers, a layer of ζ-phase gold-tin, the alloy formed during SLID bonding, 15 µm in thickness was simulated. The different layers of the model were created using block volumes.

Meshing of the elements was performed using the Solid 185 element type as shown in Figure 3.3. This element type is a structural solid capable of accepting plasticity and large strain inputs and thermal loads. Meshing of the model was performed from the bottom up, starting in the stainless steel layer and moving upwards through the silicon carbide die to ensure that the mesh was fine enough near the edge of the bond on the stainless steel substrate. ANSYS simulation code provided in A.3 and the properties of the materials used in this investigation are presented in A.4.

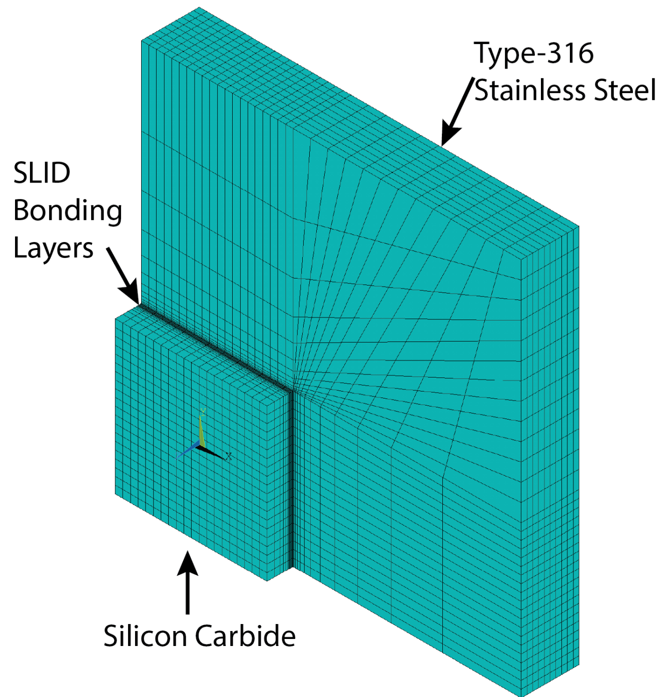

Figure 3.3: The mesh used for the finite element analysis of the bonded SiC die on steel. The mesh is finer near the areas of interest, such as the die corner, and more sparse towards the periphery of the stainless steel substrate.

The type of analysis performed in the ANSYS model was a static analysis. After meshing all the nodes were assigned with a uniform reference temperature of 300 °C. This reference assumed that the layers in the bond would be at the same temperature at the time of bonding, making for an isothermal bonding stack. In the various analyses performed the load applied to the system was a thermal load. All nodes in the model would be set to a constant final temperature and the change in temperature would drive the thermal strains. After the simulation had completed and a simulation had been converged upon, the deformed shape of the bonding stack was plotted to visualize the deflections and displacements of parts of the bond that arose form expansion or contraction. The Von Mises stresses calculated at each node were plotted on the deformed model's shape. For this analysis, the Von Mises stress was of the greatest interest because it combines the effects of the principle stresses and can be used to check if yielding and failure of the materials would occur.

3.3.1 Bond Shape Geometries of the SLID Bond

Several bonding geometries were investigated to determine how different shapes of the SLID bond would affect the distribution of thermally induced stresses in the sample. The primary geometry of the SLID bond that was investigated was that of a complete square SLID layer, fully contacting the square silicon carbide die and steel. In this model the SLID layer was given the same length and width as the silicon carbide die, 1.9 mm by 1.9 mm. The complete underside of the silicon carbide die is in contact with the bonding layer in this configuration, ensuring a robust connection of the silicon carbide across the entire bond. This geometry of the bond corresponded to the dimensions of the silicon carbide dies after the dicing process and would be the most suitable for joining a wide variety of different sensors, such as strain, pressure, acceleration and temperature sensors or harsh environment electronics to the steel.

The second bond geometry that was investigated was a cross-shaped SLID bond layer. In this configuration the SLID bond was designed to not join the corners of the silicon carbide die to the steel. In the corners, the silicon carbide die would hang freely over the steel substrate below, while a cross-shaped region in the center of the bond would contact the silicon carbide and steel. A schematic showing the different investigated bonding geometries is shown in Figure 3.4. The third geometry investigated was the center-only SLID bond, with a square bond region joining the silicon carbide die and steel substrate. A common approach to reducing the thermal strains encountered through bonding materials mismatched in CTE is to only bond the center portion of the die and allow the bulk of the die to expand or contract freely. In this investigation the center-only SLID bond was given a length and width that was a fraction of the silicon carbide die's area. The dimensions used for these alternate geometries are presented in Section 3.3.4. For each of these bonding configurations, the same material properties used for each layer of the SLID bond and the same meshing procedure was used. Lastly, in addition to the effects of different bond pad shapes, the effects of varying the thickness of the silicon carbide die, the steel substrate and the gold-tin bond layers were also investigated.

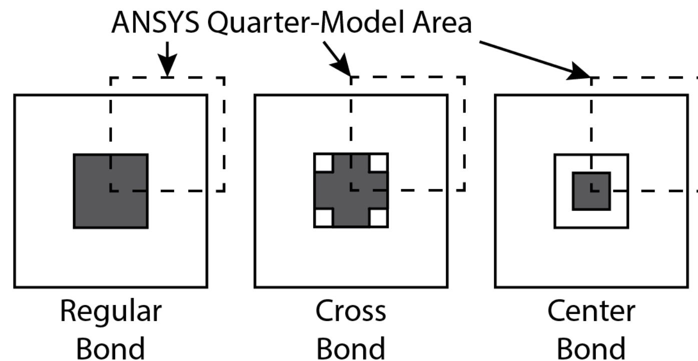

Figure 3.4: Three different SLID bond geometries were modeled in ANSYS to determine how the shape of the SLID bond would affect the distribution of stresses in the bonding stack.

3.3.2 Cooling the Square Shaped SLID Bond After Bonding

For the cooling of the square geometry SLID bond, the thermal body force load was applied to bring the system back down to room temperature at 25 °C. Stresses in the layers of the bond were noted and the simulation was performed a second time with a finer mesh to ensure that the original meshing size was adequate to capture all the details. The result of the cooling simulation is shown in Figure 3.5 with the Von Mises stresses plotted on the layers of the bond.

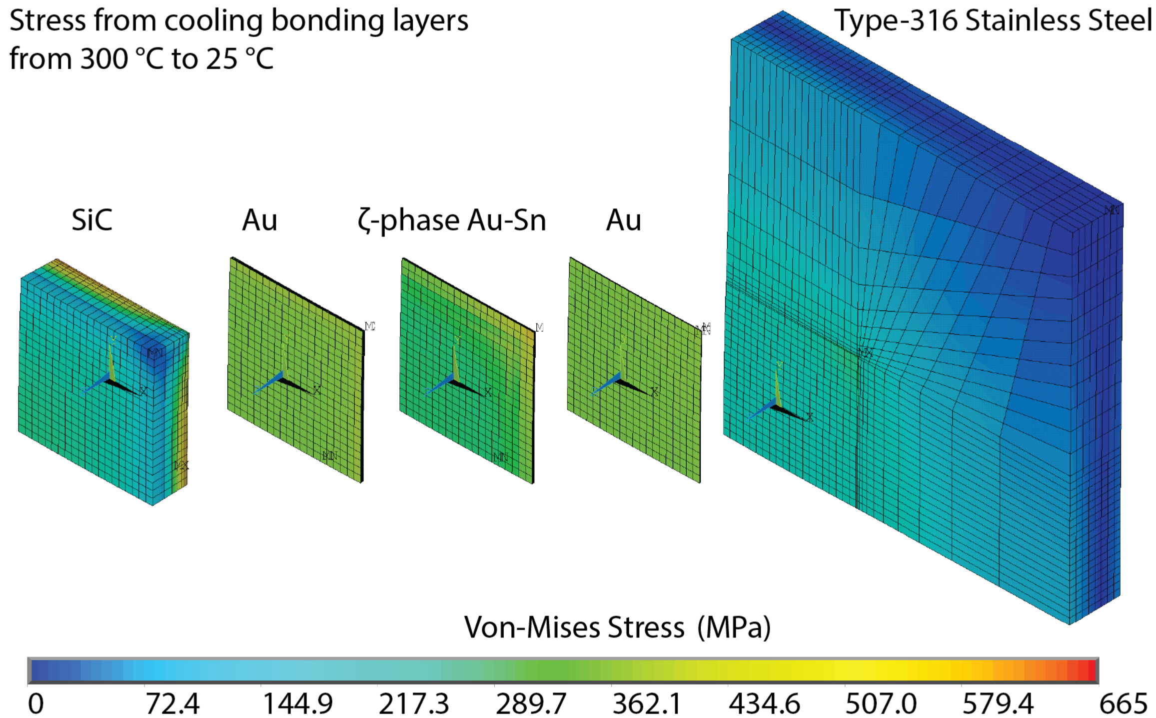

Figure 3.5: Thermal stresses modeled for the cooling of the bonding stack from the bonding temperature of 320 °C to room temperature, 25 °C.

As shown in Figure 3.5, upon cooling from the bond temperature of 300 °C to room temperature, (25 °C), the thermally induced stresses are quite significant. The maximum Von Mises stress encountered was 661 MPa, located at the edge of the silicon carbide die, along the line of symmetry. This stress, while quite large, is within the material limits for 4H silicon carbide [78]. Within the stainless steel layer, as expected the minimum stress was located at the free corner of the die, farthest away from the bonding area. The maximum stress in the steel was located in the corner of the bonding area, in direct contact with the gold layer.

In comparison with the analytical model, which did not include the effects of plasticity or shape of the bond, that the magnitude of stressed generated in the different layers are indeed reduced. The stresses presented in this analytical model are within the limits of the materials used in the bonding, so it is reasonable to say that this bond geometry configuration could be used for the SLID bonding of silicon carbide to steel. In the layers of the SLID bond, the

stress distribution in both the gold layers and the ζ' gold-tin layer was quite uniform and the maximum stresses occurredin the corner of the bonding area, farthest from the center of the quarter model.

3.3.3 Reheating the Square Shaped SLID Bond to Operational Temperature

In the reheating of the SLID bond, before the new thermal load was applied to all the nodes the coordinates of all the nodes were updated. This process ensured that the existing plastic deformations and deformed shape of the modeled bond layers would be accounted for when reheating the bond. A thermal load was applied by selecting all the nodes and setting their temperature to the operational temperature of 375 °C. With the ΔT between the operational temperature and the bonding temperature being smaller than that of the cooling case, smaller stresses were expected. The result of the reheating analysis is presented in Figure 3.6.

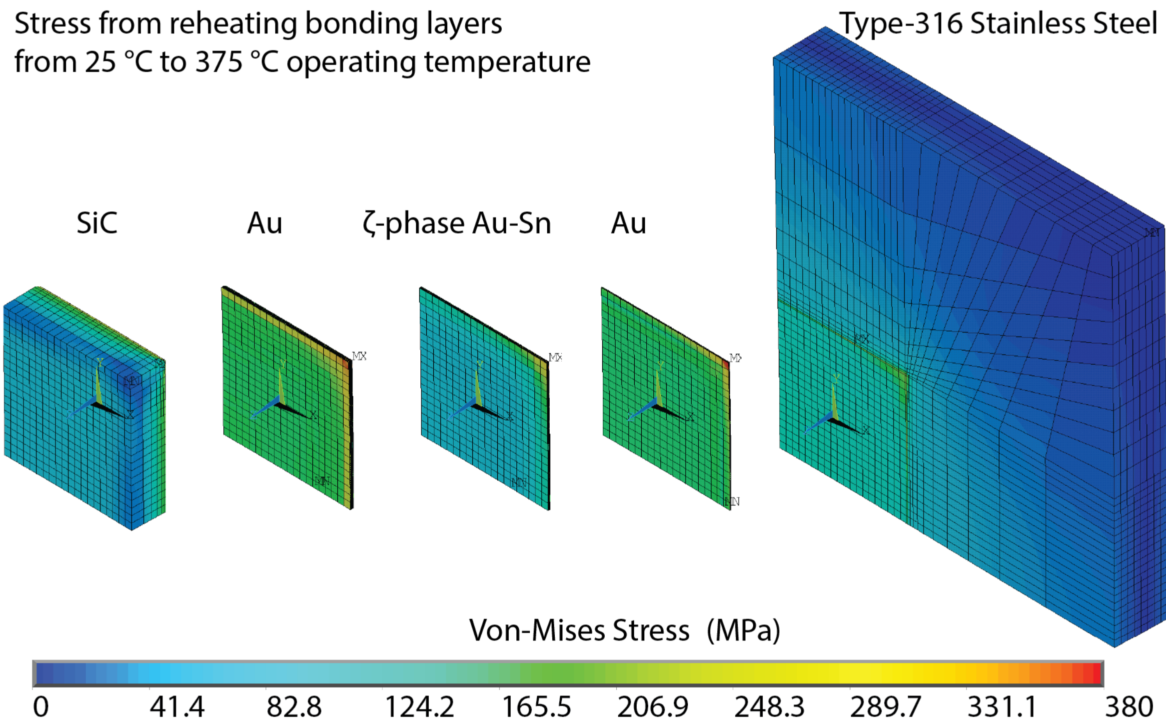

Figure 3.6: Thermal stresses modeled for the reheating of the bonding stack from room temperature,25 °C, after initial cooling, back to the operating temperature of 375 °C.

With the reheating of the sample, the Von Mises stress distribution was analyzed and it was found that the steel substrate and the silicon carbide die had significantly reduced stress. The maximum stress in the silicon carbide layer was calculated to be 299.0 MPa and was located at the bottom of the silicon carbide die at the corner of the silicon carbide die. In the steel layer, the maximum stress was also found to be in the corner of the bonding area

and the Von Mises stress there was 238.6 MPa. The highest Von Mises stresses present in the bond, with a value of 378.9 MPa, were found to occur in the corner of the gold/ζ' gold-tin/gold layers of the SLID bond in the corner of the bond. Again, the stresses simulated in the reheating of the bond satisfied the limitations of the materials and were in favor of the materials surviving the stresses induced at the operating temperature. A side-by-side comparison of the thermally induced stresses and their distribution due to the heating and cooling of the materials is provided in Figure 3.7.

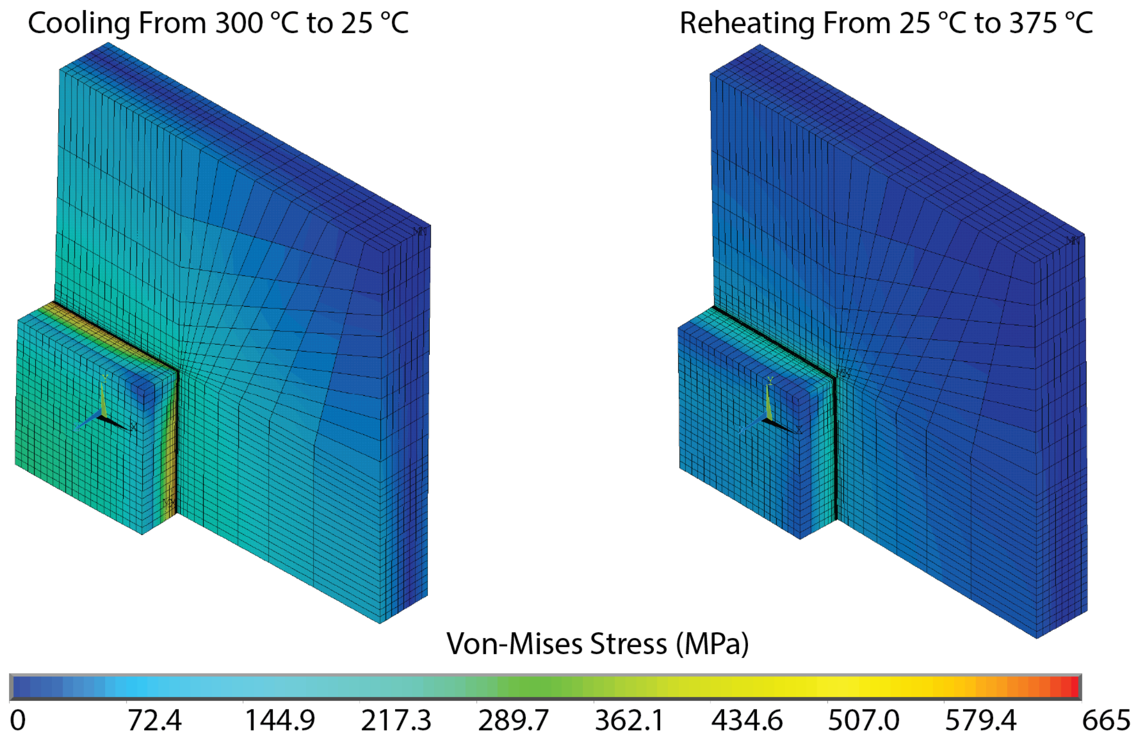

Figure 3.7: Comparison of the thermal stress generated when cooling and reheating SLID bond for the primary square-shaped, full-coverage SLID bond.

3.3.4 Modeling of Alternate Bond Geometries

Depending on the type of silicon carbide sensors being bonded to stainless steel, it is possible to consider other bonding geometries and different bond pad shapes, and so finite element modeling of the stress distributions generated by these geometries. For this modeling work, the same material properties were used but the shape of the SLID bond layer was changed to match the geometries shown in Figure 3.4. The geometries used in this model and the results of the finite element analysis are presented here.

For the consideration of the center-only SLID bond, two different dimensions for the SLID bond were considered. In the first, the gold and gold-tin layers of the SLID bond was modeled to extend outward to one-half of the silicon carbide die's width. In the quarter-model that was used, the length and width dimensions of the gold and gold-tin layers were 950 µm for

this geometry. In the second, the SLID bond layer was extended to only one-quarter of the silicon carbide die's width, with the lengths and widths of the gold and gold-tin layer being 475 µm. The results for the cooling and reheating of the larger center-bond geometry are shown in Figures 3.8 and 3.9. The modeling results for the cooling and reheating of the smaller center-bond geometry are shown in Figures 3.10 and 3.11.

With these two bond geometry configurations, it was found that the stress in the stainless steel and silicon carbide layers were reduced for both cooling and reheating the bond, as they were allowed to expand and contract more freely away from the bonding area. The gold and gold-tin bonding layer also experienced reduced stress during initial cooling and reheating. The greater freedom that was given to the silicon carbide die and stainless steel's expansion by the smaller sized center-bond, the lower the stresses were found to be. However, in real-world applications, with the reduced footprint of the bond area the durability and overall strength of the bond would be detrimentally affected. For high temperature integrated circuit die-attach applications , where electrical connection is the primary goal, a simple post structure, or set of posts, could be use to reduce the negative effects of the thermally induced stresses.

To determine if an alternate bond pad geometry could increase the contact area between the silicon carbide die and the stainless steel substrate, the cross-shaped bond geometry was analyzed. In this model, from the center of the bond the arms of the cross shape extend to the edge of the silicon carbide die. The length of the sides of the cross were designed to be 950 µm, one-half the width of the silicon die. The corners of the silicon carbide die were allowed to protrude freely over the stainless steel, while the rest of the die was able to maintain a reasonable amount of contact with the layers below. The results of the finite element analysis of the cross-bonded geometry are presented in Figures 3.12 and 3.13.

Upon cooling, the maximum stresses observed in the cooling of the cross-shaped SLID bond occurred in the corners of the cross, closest to the corner of the silicon carbide die. In the steel substrate, a stress of 312.9 MPa was observed at these locations. In the gold and gold-tin layers, the stresses were quite uniform through the cross and the maximum Von Mises stress found in those layers was 484.8 MPa, at the corners of the cross. In the silicon carbide die, the maximum Von Mises stress of 629.7 MPa was still located along the sides of the die, on the bottom side of the die which contacts the gold of the SLID layer. Being unrestrained in the corner of the die, minimum stress in the silicon carbide die was found along the edges.

From reheating the cross-shaped SLID bond, the Von Mises stresses were found to lower than those calculated in both of the center-bonded cases. The maximum stress in the stainless steel layer was 238.3 MPa, in the SLID bond layer, the maximum stress was 387.4 MPa and in the silicon carbide layer, the stress maximum stress was 350.6 MPa. In comparison with the primary full-square bond, the cross bond did provide a slight reduction in maximum Von Mises stress upon cooling. After reheating, the stresses calculated in both cases were quite comparable, except that the maximum stress in the silicon carbide die increased by about 17 % due to the concentrations at the corners of the cross. The stresses calculated for each of the bonding geometries analyzed are within the material limits of the materials and so thermal stresses alone should not cause the failure of the bonds.

Since the amount of contact area between the silicon carbide die and steel was not compromised with the regular square bond area and the stresses were manageable with the

materials, it was the chosen geometry for SLID bonding. The choice of the square bond over the cross and center bonded geometries added the benefits of simpler preform fabrication and reduced effort to align and place the silicon carbide die on the bond. To determine how changes in the layer thicknesses would affect the performance of the square SLID bond, several more simulations were performed. One variable at a time, the Von Mises stresses were simulated for cases with the silicon carbide die thinned to 250 µm, the steel substrate increased to a thickness of 3 cm, the gold layers increased to 100 µm thick and the ζ' gold-tin layer increased to 100 µm.

The effects of varying these parameters were recorded and it was determined that by thinning the silicon carbide die, Von Mises stresses in all the layers decreased, in comparison to the primary case of the square bond. However, thinning the silicon carbide die also caused the Von Mises stresses in the gold and gold-tin layers of the SLID bond to be greater as distance from the silicon carbide die decreased. In agreement with the analytical model of Section 3.2, as the steel substrate was increased to a thickness of 3 cm, the stresses in the layers increased significantly. The increased thickness of the steel caused its thermal expansion to dominate in the system. With the thick steel, the Von Mises stresses in the gold and gold-tin layer of the SLID bond increased by 18 % from the primary bond simulation with the original dimensions. Lastly, by increasing the thicknesses of the gold and the gold-tin films, the maximum Von Mises stresses in the silicon carbide and steel layers 5 % during the cooling and both decreased by about 13 % during reheating, in comparison with the original model.

From these observed trends in the finite element model, it is possible to determine the set of parameters that would best facilitate the bond. In terms of bond geometry and practicality during the implementation of SLID bonding, the square-bond with full area coverage is a good candidate. With the thicknesses of silicon carbide and stainless steel discussed in Chapter 2 a bond that does not exceed the limits of the bonding materials should be achievable. Although the increased thicknesses of the modeled gold and gold-tin layers does reduce the stress in the system, it also requires a significant amount of additional processing to form layers of such thick pure gold, and so there is an engineering tradeoff to make the gold-tin SLID bond work with thinner layers.

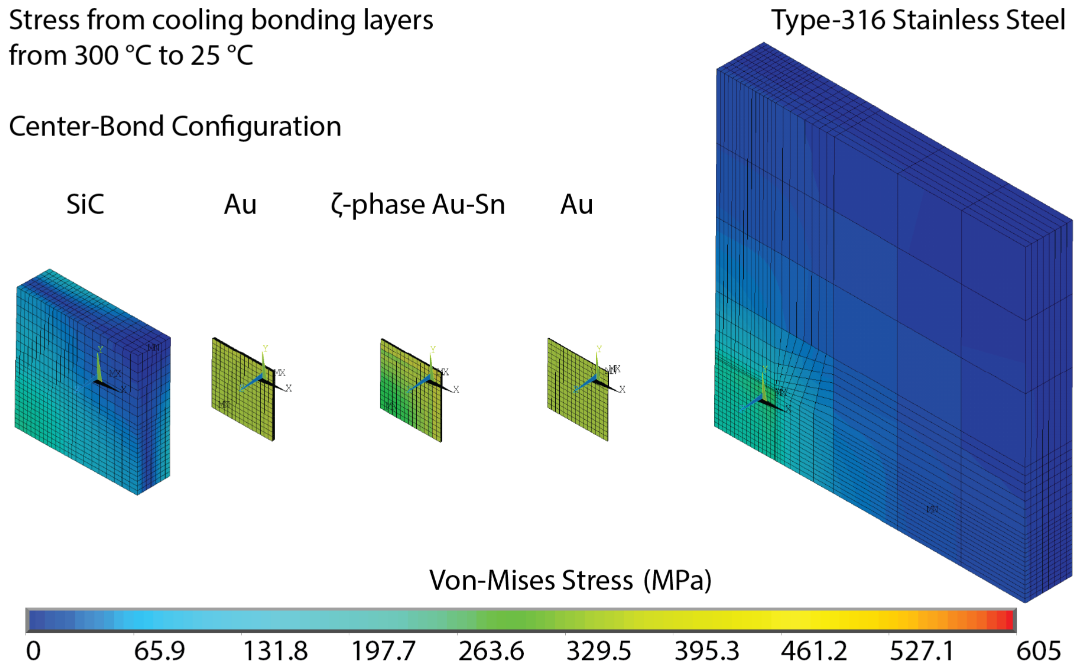

Figure 3.8: Thermal stress analysis of cooling the center-bonded silicon carbide to steel from 300 °C to 25 °C.

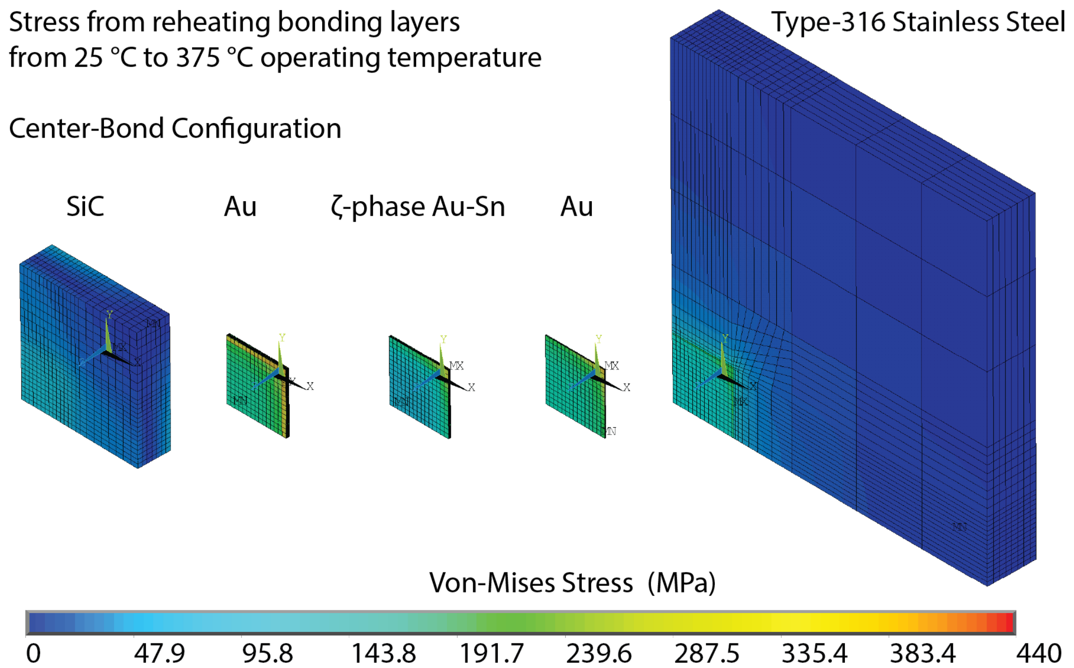

Figure 3.9: Thermal stress analysis of reheating the center-bonded silicon carbide to steel from 25 °C to 375 °C.

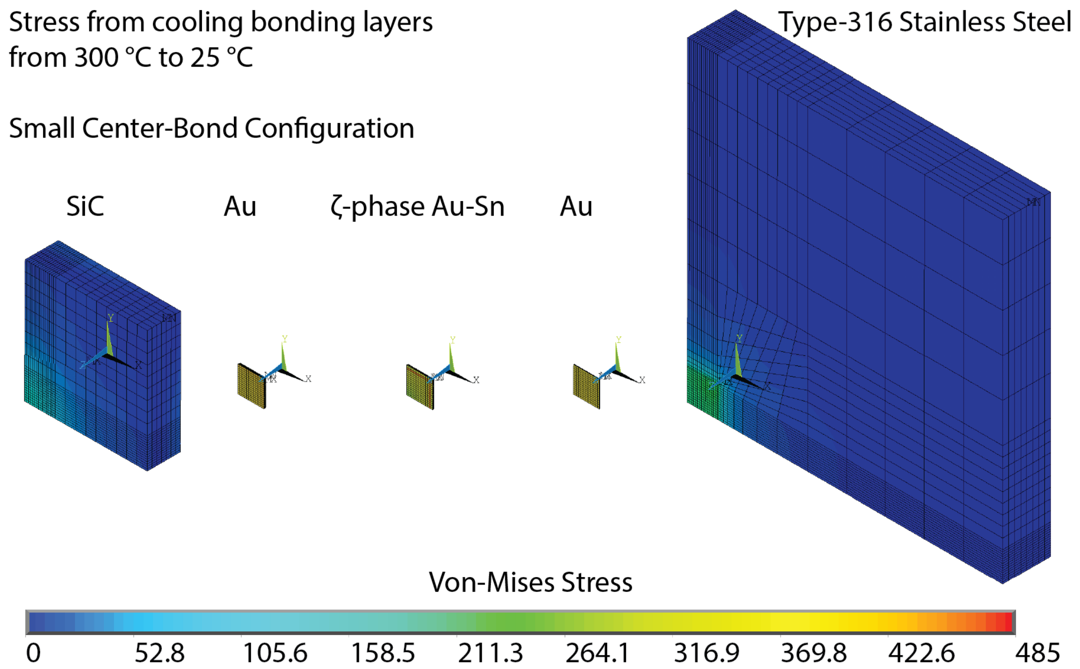

Figure 3.10: Thermal stress analysis of cooling the smaller center-bonded silicon carbide to steel from 300 °C to 25 °C.

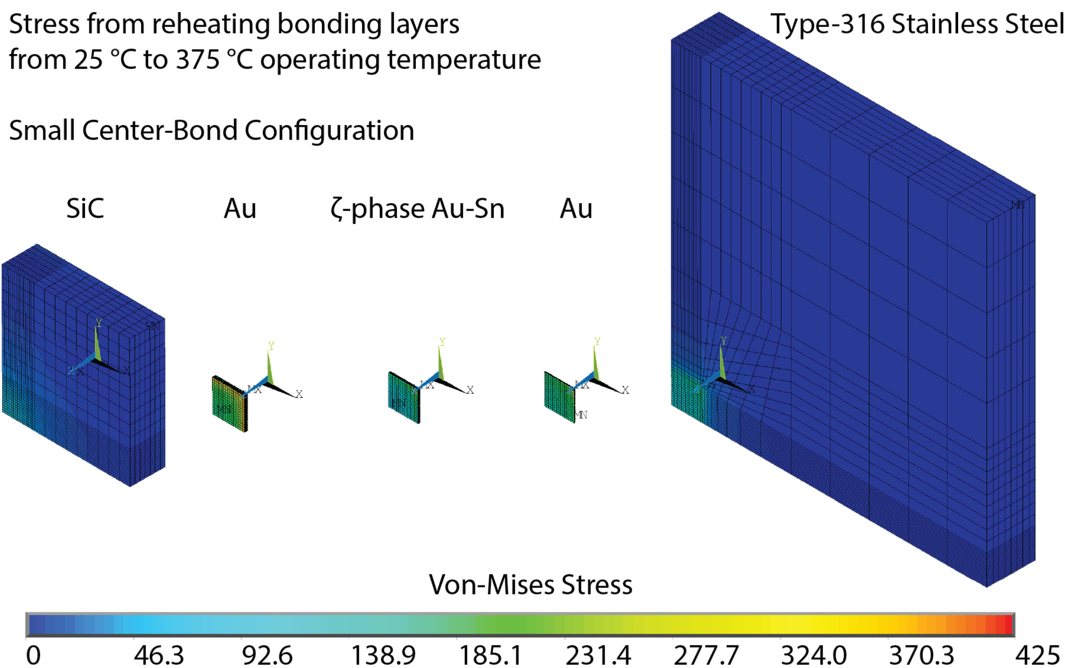

Figure 3.11: Thermal stress analysis of reheating the smaller center-bonded silicon carbide to steel from 25 °C to 375 °C.

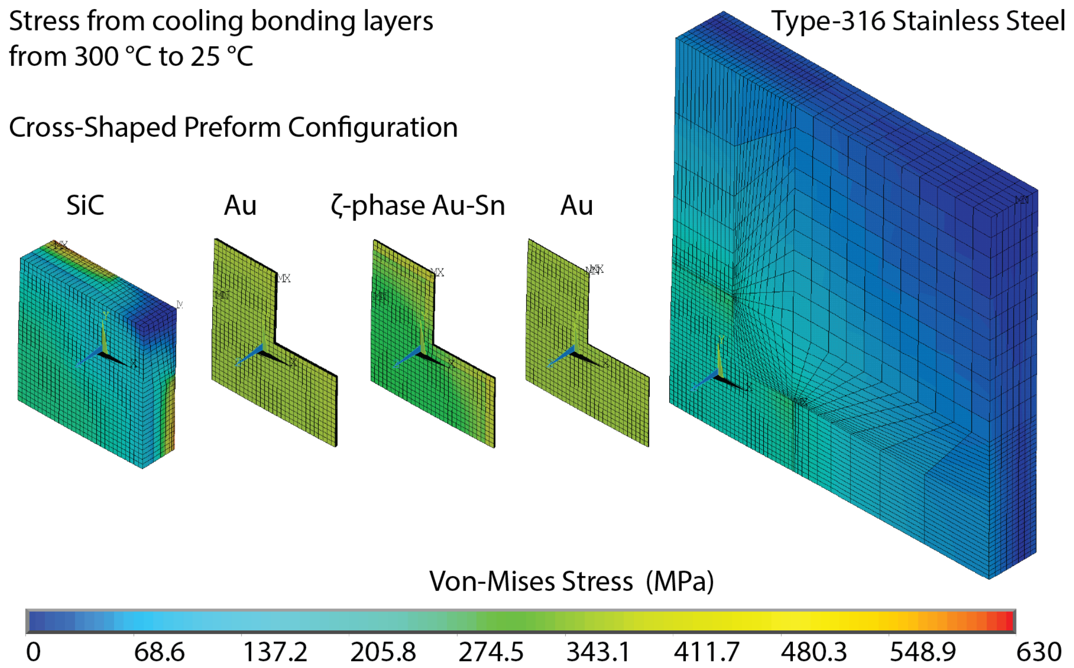

Figure 3.12: Thermal stress analysis of cooling the cross-bonded silicon carbide to steel from 300 °C to 25 °C.

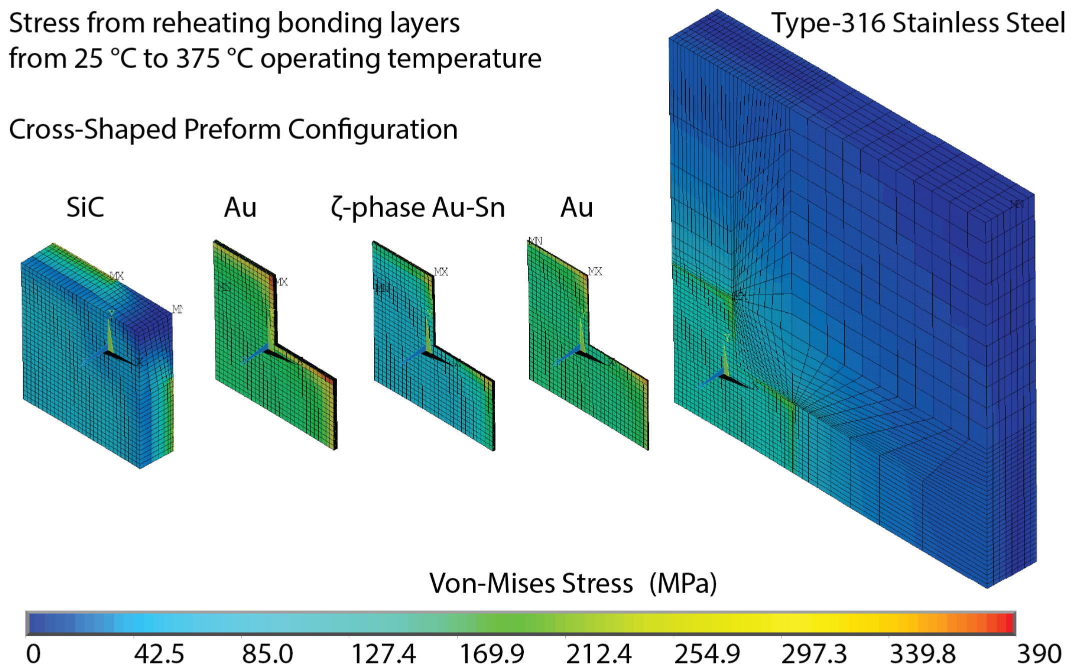

Figure 3.13: Thermal stress analysis of reheating the cross-bonded silicon carbide to steel from 25 °C to 375 °C.

Chapter 4

Characterization and Testing of the SLID Bonds

For the MEMS sensors to operate in high temperature harsh environment conditions, it is imperative that the SLID bond joining them to the metal components be able to survive the same conditions. To evaluate the bond strength of the SLID bonded samples and to characterize how varying the different bonding parameters affected the overall bond strength, destructive testing of the bond was performed. The bonds were tested mechanically at room temperature and at elevated temperatures. Cross-sectional compositional analysis of the bonds was performed before and after subjecting the bonds to high temperatures. The effect of high temperature aging and its effect on bond strength and metallurgical composition of the SLID bond were also studied. A rigorous testing protocol was developed to measure the strength of the silicon carbide to steel bonds. In some of the testing the bonds were subjected to temperatures which would be encountered in geothermal well monitoring applications to ensure that the bond would survive high temperatures beyond the bonding temperature. The cross sections of the bonds were inspected and the mettalurgical compositions of the SLID bonds were investigated to understand how prolonged high temperature exposure would affect the integrity and composition of the gold-tin SLID bond. This chapter outlines the bonding parameters that were varied, the testing performed on the SLID Bonds, and the characterization of the SLID bonding process for SiC to steel.

4.1 Die Shear Testing Method

A crucial metric for the performance of the SLID bond is the strength of the bond. In the packaging industry, the strength metric of a bonded die is typically given by the ultimate die shear strength of the bond when tested in accordance with Military Standard 883, method 2019.7 [79]. This standard outlines the protocol used to investigate the integrity of the bond materials and the bond quality by destructively testing the bond to failure. It also classifies the separation of the bonded die from the underlying substrate into three categories: cohesive failure of the bonded die, in which residual parts of the die are left bonded to the substrate; adhesive failure between the bonded die to the die-attach medium, in this case the gold-tin SLID bond layer; and adhesive failure between the SLID bond layer and the underlying

stainless steel substrate.

Cohesive and adhesive failure mechanisms refer to the way the bond or bonding materials break when tested. Cohesive failures occur within a given material, such as the within the SiC die or within the gold-tin SLID bond layer, in the case of silicon carbide to steel SLID bonding. During die shear testing, if the SLID bond layer separates while remaining adhered to both the SiC die and the stainless steel, the failure is considered to be a cohesive failure within the SLID bond layer. Similarly, cohesive failures can occur within the SiC die, in which case part of the die would fracture while leaving behind SiC material bonded to the SLID bond. In contrast with cohesive failures, adhesive failures occur at the interface between two different materials, such as between the SLID bond layer and the underlying steel sample. Adhesive failures would include the SLID bond layer separating from the stainless steel.

The military standard's strength requirement of the bond, based on the size of the bonded die, is outlined in Figure 4.1. Based on a the size of the bonded SiC dies being 3.8 mm by 3.8 mm in area, (0.0224 in) to fulfill the 1.0×, 1.25×, and 2.0× standards, the bond must survive shear forces of 25.53 N, 30.66 N and 49.05 N respectively, which translate to to respective shear stresses of 1.698 MPa, 2.123 MPa and 3.397 MPa.

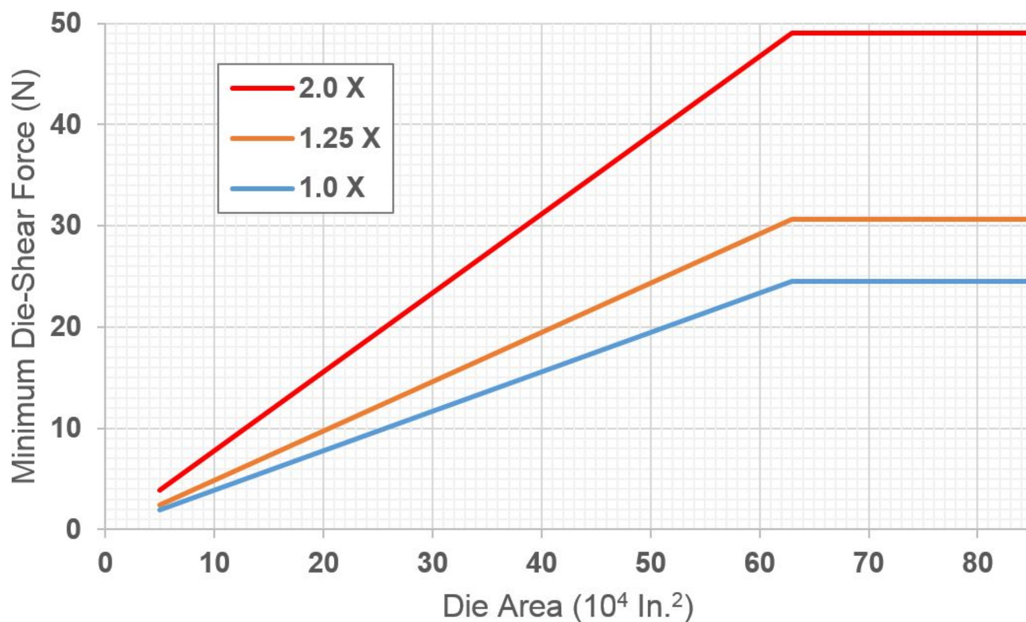

Figure 4.1: The MIL-STD 883J die shear strength requirements for microelectronics devices bonded to substrates. Die shear strengths versus die bond area are plotted to satisfy the standard's 1.0×, 1.25×, and 2.0× strength requirements.

To perform the die shear testing two bond testers were employed; a Nordson DAGE 4000 Bondtester and a XYZTec Condor Sigma Bondtester. Both systems were used to destructively evaluate the ultimate shear strength of the bonded samples. These die shear testers were equipped with a shearing wedge, which was designed to be wider than the part being sheared to ensure that contact would be made to the entire surface of the part being sheared. In the testing process, the sample being sheared would be secured onto a stage consisting of vise jaws or a vacuum chuck stage, as shown in Figure 4.2. With the sample

secured to the stage, the stage was aligned to the die shear wedge to ensure that the flat of the wedge would be parallel to the edge of the component being sheared. Errors in the alignment would cause a significant concentration of stress in the small area initially contacted by the tester.

The height at which the die shearing wedge contacts the sample is also of critical importance. If the shear height is too great and the wedge contacts bonded samples too high, excessive stress is developed in the top part of the sample, and if the sample is brittle like silicon or silicon carbide they tend to fracture before the bond fails. If the shear height is not high enough, wedge will scrape into the bond layer, measuring the cohesion of the bonding layer instead of accurately measuring the total bond strength of the sample. The load was applied to the dies using a die shear speed of $300\,\mu m\,s^{-1}$; a speed commonly used in industry for the testing of solder strength in microelectronic components. In each test performed, the shear wedge would back away from the edge of the die, lower itself until it contacted the underlying substrate, raise itself to the assigned die shear height, and then process forward into the sample at the prescribed die shear rate. For the application of loads, both the Nordson DAGE 4000 and XYZTec Condor Sigma were equipped with 100 kg weight cartridges, capable of applying and measuring up to 981 N of force in the shear direction.

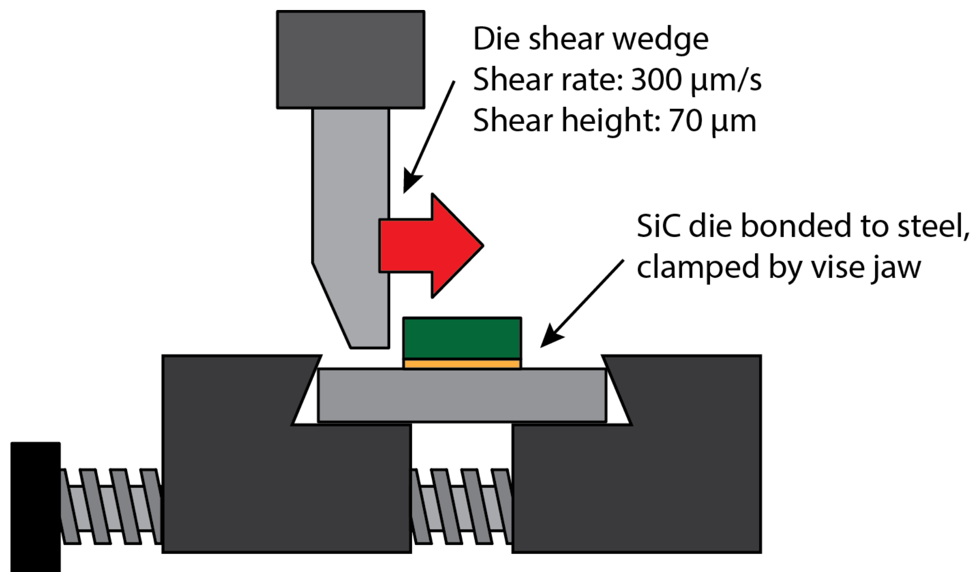

Figure 4.2: Operation of the high temperature die shear testing apparatus. The load-applicator block passes over the stainless steel substrate and contacts the SiC die.

In die shear testing, the profile of the force application versus time is recorded and presented as shown in Figure 4.3. The force versus time graph gives some insight as to how the bond yields and when combined with optical inspection during the die shear testing, it can be used to distinguish if damage occurs to the die before the bond fails. When total failure of the bond occurs and it has been successfully sheared, the force rapidly decreases.

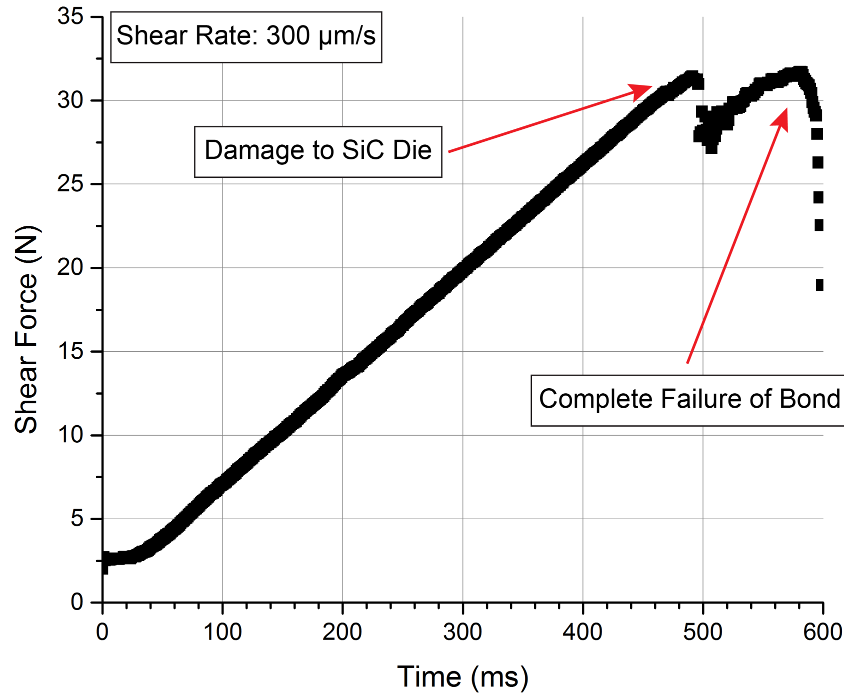

Figure 4.3: Plot of the die shear force versus displacement for a die-shear test of a SiC die bonded to stainless steel substrate. The maximum force registered before the failure of the die or bond is used to determine the strength of the bond.

4.2 Microscopy and Chemical Composition Analysis Methods

To improve the understanding of what occurs in the SLID bonding layer, optical microscopy, scanning electron microscopy and energy dispersive x-ray analysis were employed to investigate the appearance of the bond layers, where fractures occurred during die shear testing and to determine the chemical composition of different areas of the bond. These visual inspection techniques offer great insight as to how and where a particular bond failed as well as visually identifying differences in alloy composition in the bond. Chemical compositional analysis further aids in identifying the materials present in the bond and provides additional information to characterizing the failure of the bond. Metallographic polishing of the samples was performed to enable the inspection of the cross-section of the bonds for both chemical composition as well as physical appearance.

4.2.1 Optical microscopy

An Olympus LEXT OLS3000 3D laser confocal microscope was used to inspect the fracture surfaces and cross sections of the bonds. Using 10×, 20× and 50× objective lenses

provided high resolution optical images of the bond in color. The ability to distinguish color and luster significantly aids in the determination of how far the gold-tin diffusion spreads in the gold-tin SLID bond. There are noticeable visual differences in color between pure gold, Au80%wt.-Sn20%wt., and ζ' gold-tin phases. Additionally, the software integrated with the LEXT microscope allows for the measurement of distances which was used to verify the thickness of the formed SLID bonds and to measure features within the bond.

4.2.2 Scanning Electron Microscopy and Energy Dispersive X-Ray Analysis

Scanning electron microscopy was used to analyze the fracture surfaces of the die-shear tested bonds as well as the cross-sections of the bonded samples after metallographic polishing. Scanning electron microscopy offers the ability to image the areas of interest in the bond with magnifications much greater than optical light microscopy. Although the image produced by the SEM is black and white, the high magnification and the slight difference in contrast between materials enables the distinction between some phases of gold-tin. A FEI Quanta scanning electron microscope, equipped with an Oxford energy-dispersive x-ray (EDX) detector was used to determine the species of elements present in regions of the bond.

Although several other chemical compositional analysis tools were available, such as X-ray photoelectron spectroscopy (XPS) and Auger electron spectroscopy (AES), EDX analysis was chosen as the method for analyzing the SLID bond because of its spatial resolution. XPS analysis would provide a highly accurate compositional analysis of the layers in the bond, however, the preparation of the layers would be quite difficult and require the careful stripping away of the bonded silicon carbide die and careful removal of material through the gold-tin bond layers to get an accurate compositional profile versus depth into the bond. EDX spectroscopy, on the other hand, provides a better spot measurement of a localized area and can be performed on various regions of a cross section to determine the composition of the metal. EDX spectroscopy operates by using a high-energy beam of charged particles to strike the specimen being studied. The high energy excites electrons present in the atoms electron shells to a higher energy state, and as those electrons return to recombine in the electron shell, X-rays are emitted. The number of X-rays and the energies of the emitted X-Rays provide a signature for the elements present and are used to determine the composition of the scanned area.

For EDX analysis, after finding the area of interest for analysis and zooming in as far as possible with the SEM, an excitation voltage of 30 keV was used for the X-ray analysis. In EDX analysis, as the accelerated particles hit the specimen being analyzed, there is some tunneling and penetration into the sample. Due to this phenomenon, instead of measuring an exact spot of material in the specimen, an excitation volume is analyzed. The equations used to calculate the depth of this excitation volume is given in 4.1, and the width of the excitation volume is calculated using Equation 4.2, where the density, ρ (in $\mathrm{g\,cm^{-3}}$), of the material being analyzed and the acceleration voltage, E_o (in keV), are accounted for.

$$\mathrm{x}(\mu\mathrm{m}) = \frac{0.1{E_o}^1.5}{\rho} \tag{4.1}$$

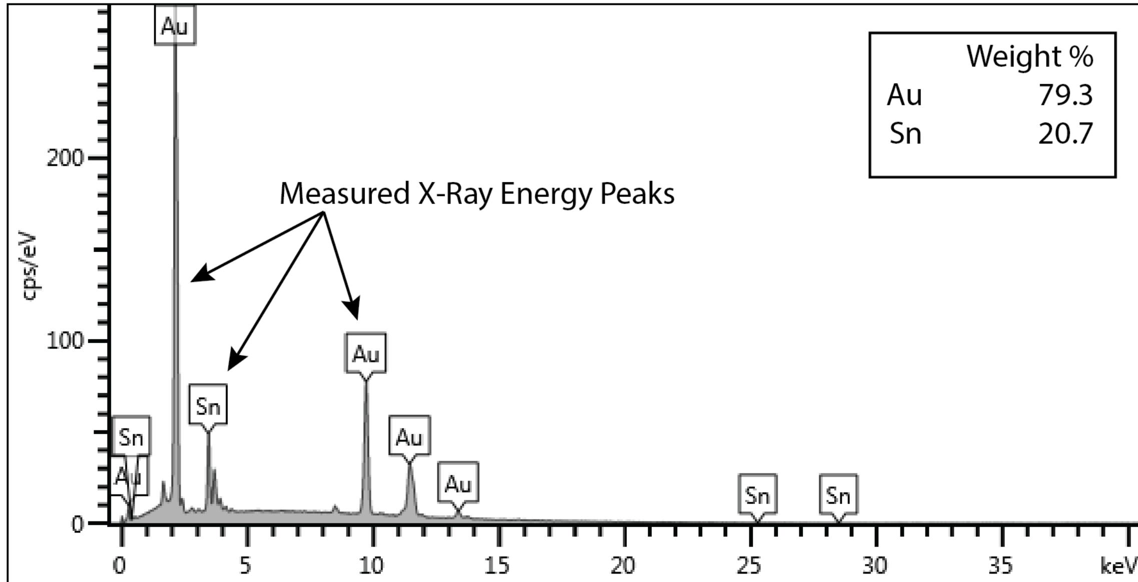

Figure 4.4: An EDX analysis spectrum for the analysis of a Au80%wt.-Sn20%wt. solder preform is shown here. The overall EDX analysis accuracy is around ±2% due to scattering and the software's corrections applied to the raw data.

$$\mathrm{y(\mu m)} = \frac{0.077\mathrm{E_o}^{1}.5}{\rho} \tag{4.2}$$

For a 30 keV acceleration voltage, this translates to an excitation volume depth of 0.851 µm and a width of 0.656 µm. The accuracy for EDX spectroscopy compositional analysis is about ±2% due to the scattering events during measurement and the statistical corrections that the software applies to the raw data collected by the X-ray detector. An example of an EDX analysis spectrum for Au80%wt.-Sn20%wt. is shown in Figure 4.4.

4.2.3 Metallographic Polishing

Metallographic polishing is a destructive inspection tool that enables the inspection of cross-sections and internal compositions, such as the grain structure of metals. In this research the application of metallographic polishing is highly relevant in that it can expose the cross-section of the completed SLID bond and enable characterization of the bonds composition as a function of position in the bond. Preparation of the samples for cross-sectional analysis after bonding consisted of casting the samples in an epoxy resin, as shown in Figure 4.5. The samples were held in place with plastic clips as the epoxy was poured into the mold. After pouring, the samples were placed in a vacuum chamber and allowed to outgas for 5 minutes before the chamber was vented. The epoxy was allowed to harden overnight in ambient laboratory room conditions. Due to the geometry of the Silicon carbide dies being bonded to the center of the steel square, after casting in epoxy a lathe was used to remove the excess epoxy leading up to the cross section. Care was taken to avoid cutting into the stainless steel and the silicon carbide dies as machining into them would cause severe

shock and the mechanical deformation of the steel would cause the silicon carbide substrate to fracture and dislodge from the bond layer, thus invalidating the sample for later analysis. Following lathing a manual rough sanding with coarse 180, 320 and 400 grit sand papers with water cooling was performed to abrade the remaining steel and epoxy preceding the SiC to Steel bond interface. Water cooling during the sanding ensured that the temperature rise of the steel due to the abrasion would not cause significant heating that would affect the state of the SiC to Steel SLID bond. Excess heating would considerably raise the temperature of the steel and could provide enough thermal energy to alter the composition of the SLID Bond.

Figure 4.5: Bonded SiC to steel samples were casted in epoxy for metallographic polishing operations to enable detailed analysis of the cross section of the bond.

After the rough preparation, a Pace Technologies Nano 2000 metallographic polisher with 8 inch wheels was used to finish preparing the final sanding and the polishing of the sample [80]. If planarity issues were encountered between the silicon carbide and the steel substrate, a Cermesh™metal mesh abrasive cloth was used for polishing in conjunction with 30 µm abrasive grit. The final sanding procedure consisted of manually sanding the epoxy-cast samples by hand with 800 grit SiC sandpaper at 300 rpm, followed by 1200 grit sandpaper at 200 rpm, bringing the surface roughness of the sample down to approximately 9 µm. The polishing procedure was carried out with 6 µm and 1 µm polycrystalline diamond suspensions in colloidal silica on respective low-napped polymer polishing pads. After polishing, the samples were thoroughly rinsed with water to remove any remnants of the polishing grit and dried with compressed air before performing an inspection of the cross-section.

4.3 Characterization and Testing of Si to Si SLID Bonds

For the silicon to silicon SLID bonded dies whose fabrication process was outlined in Section 2.3, die shear strength testing as well as chemical compositional analysis was performed. These silicon to silicon bonds were part of the initial investigation to understand the SLID bonding process and observe the SLID process in action. The results of the characterization are presented in this section.

4.3.1 Die Shear Testing of Si to Si SLID Bonds

Die shear testing of the initial Si to Si SLID bonds were performed in the microfabrication facilities at Vestfold University College in Norway using a Nordson Dage 4000 Bondtester. The dies tested were the silicon samples metalized with chromium-tin-gold as described in Section 2.3. For testing, due to the gripping limitations of the available vise jaw stage, the bottom surface of the bonded silicon to silicon samples were glued to a larger ceramic circuit board substrate using a cyanoacrylate adhesive. After allowing the adhesive to set, the bottom half of the bonded stack was securely attached for die shear testing. Following the setting of the glue, the vise jaws of the tester were aligned so that their 1 cm edge was parallel to the die-shear wedge. A die shear testing height of 570 µm was used to ensure safe clearance over the bottom silicon die and the bond layer.

During testing of the bonds of samples TLP6 to TLP6 the average force the bonds survived was 37.37 N, or a 186.83 kPa shear stress based on the 1 cm by 2 cm die area). Based on the size of these dies the bonds of TLP6 to TLP6 surpassed the 1.25× requirement of MIL-STD 883J, but not the 2.0× requirement. For the bonds of TLP3 to TLP3, the bonded dies survived an average of 20.38 N force in the shear direction, or a 101.90 kPa shear stress. The bonds of TLP3 to TLP3 did not meet the MIL-STD883J requirements. Lastly, the bonds of TLP6 to TLP3 generated no force measurements when they were tested. The top substrate simply glided off the bottom substrate with minimal force applied, resulting in no measurement. The bond strengths of these silicon to silicon samples was relatively and so an optical analysis of the fracture surface was performed to understand what the fracture surface looked like and to see if the underlying cause of the weakness of the bond could be determined.

4.3.2 Optical and Compositional Analysis of Si to Si SLID Bonds

After die shear testing, the surface of the sheared silicon substrates and the cross-section of other TLP6 to TLP6 and TLP 3 to TLP3 samples were inspected using optical microscopy as well as scanning electron microscopy and energy dispersive x-ray analysis. Upon inspection of the die-shear tested surface it was evident that the bond layer was not uniform. An optical microscopy image of the bond taken at 250×, shown in Figure 4.6, shows that the bond layer was not a continuous layer of metal and that mounds of gold-tin alloy had formed. Figure 4.6 compares the surface of the e-beam evaporated silicon surface before bonding and after bonding, and shows the mounds of metals that were generated during the bonding process.

Additionally, the cross section images of the silicon to silicon SLID bonding samples, shown in in Figure 4.7, processed alongside the samples that were die shear tested, revealed

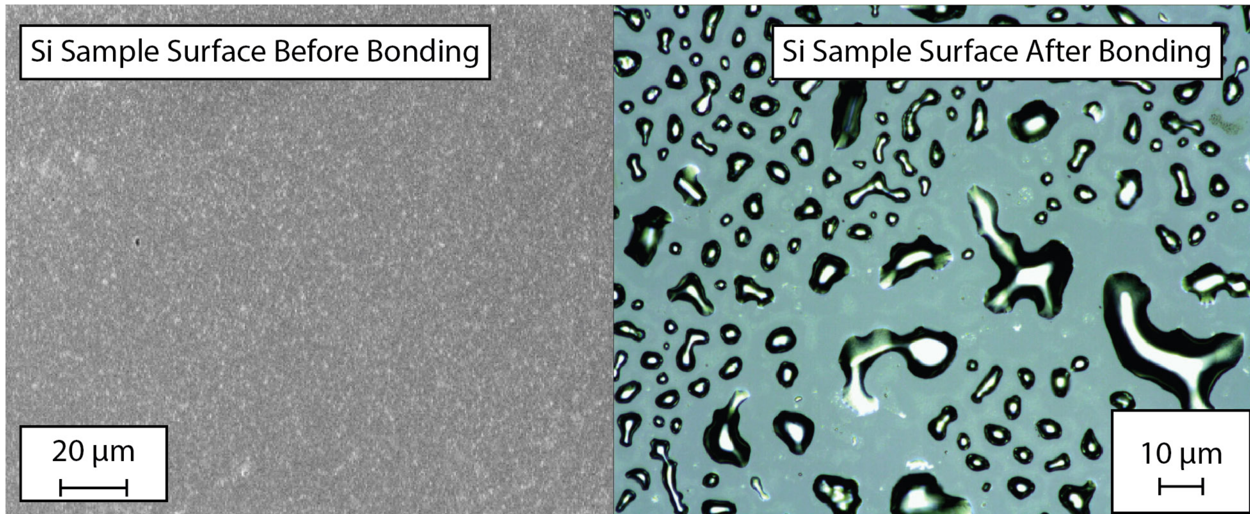

Figure 4.6: On the left, a SEM image Optical microscopy image, taken at 250x magnification, of the surface of the silicon die after die shear testing. This image and images from other portions of the Si die were used to determine the true contact area between the bonded silicon dies.

that many voids were present in the bond. The excessive voiding accounted for a significant reduction of area, and using the software measuring tool to calculate the total amount of area covered with the gold-tin intermetallic the true cross-sectional area of these Si to Si SLID Bonds was measured. Four different regions of the samples were optically inspected and the percent coverage of gold-tin intermetallic on the silicon substrate was found to be 32.9 % in the TLP6 to TLP6 bonds and 24.9 % in the TLP3 to TLP3 bonds. A MATLAB script presented in Chapter A.5 was used to calculate the true area of the gold-tin intermetallic. Considering that the shear stresses from testing were applied to a much reduced area, the actual shear strengths survived by the bonds were 562 kPa for the TLP6 to TLP6 bond and 409 kPa for the TLP3 to TLP3 bond.

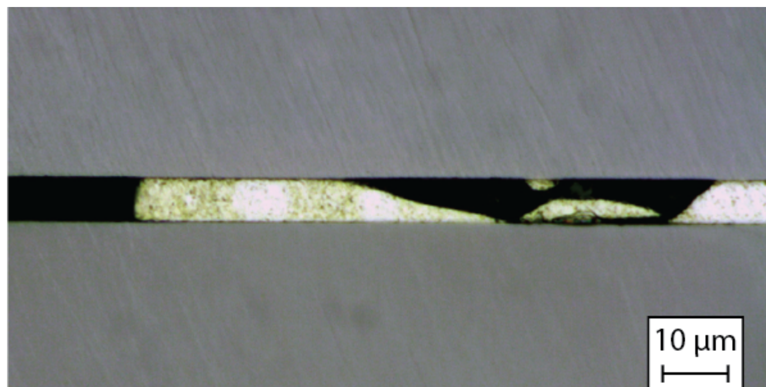

Figure 4.7: Metallographic polishing of the Si to Si bonds using the SLID process outlined in Section 2.3. Optical analysis confirmed that many voids were present in the bond between the islands of gold-tin intermetallic alloys.

To determine the composition of the intermetallic mounds that had formed during bonding, EDX analysis was performed on different regions of the mounds as shown in Figure 4.8. In the top-down inspection of the surface after die-shear testing, the peaks of the mounds and the bases of the mounds were scanned to see if there was a difference in composition. Additionally, in the cross section analysis, sections of the gold-tin intermetallic were analyzed closer to the silicon substrate as well as in the middle of the intermetallic. In the regions nearer the silicon substrate, there was a higher concentration of gold present, and the EDX analysis recorded a composition of Au66%at.-Sn33%at, which corresponds to the ϵ gold-tin phase ($AuSn_2$). The remaining 1%at. was measured as a trace amount of silicon measured by the scattered electron beam. Farther away from the silicon die, it was determined that the composition was Au51%at.-Sn48%at., which given the accuracy of EDX analysis suggested the δ phase of gold-tin (AuSn).

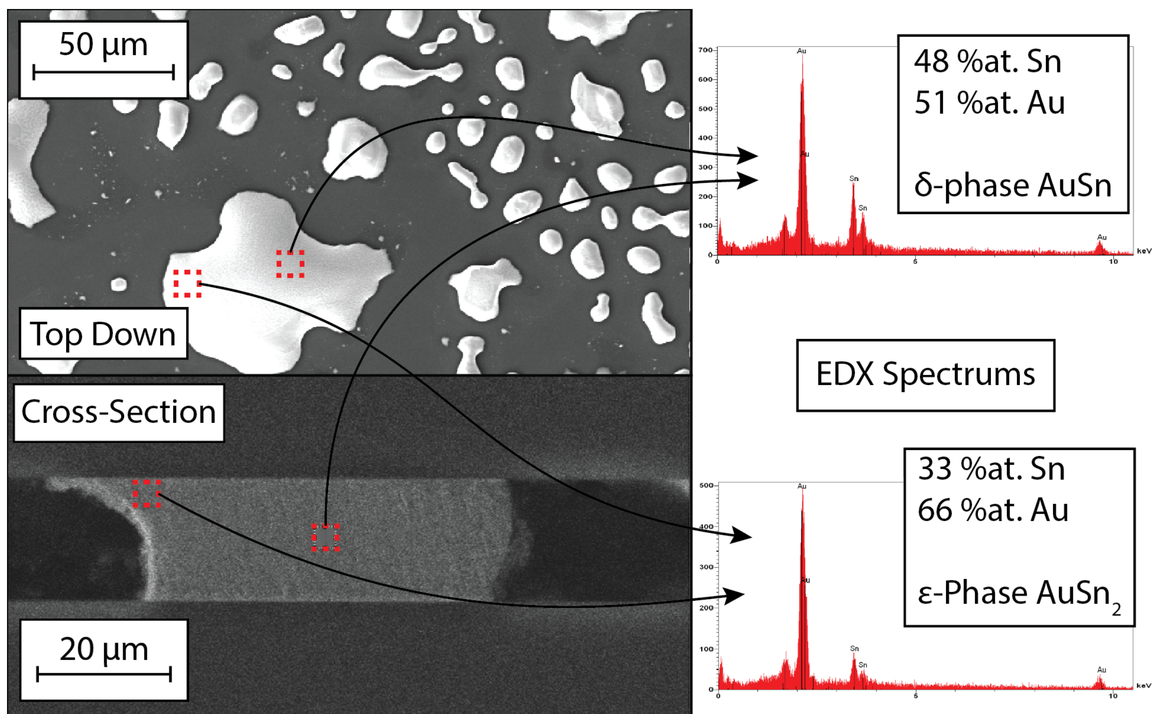

Figure 4.8: On the left, a SEM image Optical microscopy image, taken at 250x magnification, of the surface of the silicon die after die shear testing. This image and images from other portions of the Si die were used to determine the true contact area between the bonded silicon dies.

Referring back to the phase diagram of the gold tin metal system, it is apparent that the gold layer did diffuse into the tin and formed the δ phase closer to the center of the bond, where there was an excess of pure tin. Nearer to the silicon substrates, where the e-beam evaporated films were originally pure gold, the ϵ phase was formed. With the 350 °C bond temperature used in the preparation of the TLP6 and TLP3 bonds, not enough thermal energy was provided to bring the system through the stable δ gold-tin phase. During the bonding process, it appears that as the temperature in the bonding chamber rose, the diffusion of gold into tin formed the δ phase alloy locally, before the pure tin layer could

completely melt and form a uniform liquid layer. As the δ phase solidified and as diffusion continued it was increasingly difficult for the bond layer to become even and the mounds of intermetallic were formed. In order to overcome this limit of the δ phase gold tin, a temperature greater than 419 °C and a faster heating rate would have been required for bonding when using pure tin as the melting point depressant. Additionally, for this type of bonding, with evaporated thin films of gold and tin, the thickness ratio should have been closer to 3Au:2Sn in order to form the higher melting point β, ζ and ζ' gold-tin intermetallics, based on the thickness calculations performed in Section 3.1. The use of pure gold and pure tin thin films shows promise for wafer level and die level attachment schemes for high temperature survival as long as the proper film thicknesses are used.

4.4 Characterization and Testing of SiC to Steel SLID Bonds

A thorough investigation of the silicon carbide to steel bonds was performed and the suitability of the bond for high temperature harsh environment applications was analyzed. The effect that the thicknesses of the SLID bonding layers had on the strength of the bond was characterized and the composition of the SLID layer after bonding was analyzed. Die shear testing was performed at room temperature after the bonds had cooled after bonding along with a thorough analysis of the bond's chemical composition. The effects of high temperature aging on the bonds strength was investigated along with how the composition of the SLID bond reacted to prolonged high temperature exposure. Additionally, the bond strength of the silicon carbide to steel SLID bonds as well as their survivability at high temperatures was tested. This section documents the characterization and testing performed on the silicon carbide to steel SLID bonds.

4.4.1 Die Shear Testing of SiC to Steel SLID Bond After Cooling

After the fabrication and bonding of the silicon carbide dies to stainless steel, the die shear strengths of the bonds were characterized at room temperature. An orthogonal array of experiments, shown in Table 4.1, was designed to determine the effect of gold thickness on steel, gold thickness on the silicon carbide substrate and the thickness of the Au80%wt.-Sn20%wt. eutectic solder preform on the strength of the bond. Eight sets of experiments were made to understand the effect of these parameters on the bond's shear strength using a two-level full factorial design of experiments.

In this design of experiments the examined gold-plating thicknesses on steel were 10 µm and 20 µm. The two tested thicknesses of pure gold, electroplated on the SiC substrate, were 20 µm and 40 µm thick. These films were electroplated and prepared using the procedures described in Section 2.4.3. The gold-plated steel samples were fabricated using the electroplating procedure discussed in Section 2.4.3. The Au80%wt.-Sn20%wt. solder preform thicknesses that were tested were 5 µm and 12.7 µm thick. The different thicknesses of Au80%wt.-Sn20%wt. eutectic would affect the required amount of gold to form the ζ and β phases of gold-tin, and alter the amount of remaining pure gold left over after the SLID bonding process. These 8 combinations of experimental parameters were organized in such

Table 4.1: The design of experiments used to determine the effect of SLID bonding parameters on the strength of the bond.

Experiment	Au80/Sn20 Preform Thickness (µm)	Au Thickness on Stainless Steel (µm)	Au Thickness on SiC (µm)
1	5	10	20
2	12.7	10	20
3	5	20	20
4	12.7	20	20
5	5	10	40
6	12.7	10	40
7	5	20	40
8	12.7	20	40

a way that the effects of the three independent variables, (solder preform thickness, gold thickness on steel and gold thickness on silicon carbide) could be characterized and their individual contributions to how they affected bond strength could be analyzed.

For the determination of the bond strength an XYZtec Condor Sigma and Nordson DAGE 4000 were used. The wedge used to apply shear force to the die was flat and measured 10 mm wide, larger than the 3.8 mm width of the SiC die, to ensure that the wedge would not impart a localized stress concentration to the SiC. A die shear height of 70 µm was used for testing to ensure clearance over the SLID bond, so that contact would be made solely between the die shear wedge and the flat edge of the SiC die.

The die shear strength results from the testing of the eight variations of parameters are shown in Table 4.2. Several samples of each bonding configuration had to be fabricated and tested to account for minor variations in the die shear testing process and the fabrication steps. From this set of raw data it is evident that for the die size of 3.8 mm by 3.8 mm all the tested configurations of bond thicknesses, except the 5th experimental combination, surpassed the 2.0× MIL-STD 883J die shear requirement outlined in Section 4.1. The average strength for the 5th experimental configuration surpassed the military standard's 1.25× but not the 2.0× benchmark.

From the results of testing these 8 combinations of the parameters, the main effect of each parameter can be calculated [81]. For a particular variable, Au80%wt.-Sn20%wt. thickness for example, the calculation involves averaging the die shear strength data collected in which the thick 12.7 µm preforms were used, and subtracting the average die shear strength for the experiments in which the thin 5 µm preforms were used. A MATLAB script, presented in Section A.6 was used to aid in performing the effect calculation for each of the variables. It was found that both thicker electroplating on the silicon carbide die and a thicker gold-tin eutectic preform improved the overall bond strength. Analyzing the effect of the electroplated gold thickness on bond strength showed a slight trend that that the thicker plated films on steel did not improve the overall bond strength. This result was counterintuitive to the

Table 4.2: The average die shear strengths (in MPa) are given for the samples tested using the parameters stated in Table 4.1.

Experiment	Number of Samples Tested	Average Die Shear Strength (MPa)
1	3	15.8
2	3	8.03
3	4	13.5
4	4	6.34
5	3	3.90
6	3	32.2
7	4	6.36
8	4	28.7

finite element analysis calculations from Chapter 3, and so further investigation into the composition and integrity of the bonds were performed.

4.4.2 Compositional Analysis of SiC to Steel SLID Bond After Cooling

Before bonding the samples, the cross-section of an assembled silicon carbide to steel bond was imaged, as shown in Figure 4.9. The cross section of the bonds were investigated as shown in Figure 4.9. In the SEM image alone, the difference between the gold-tin eutectic preform and the pure electroplated gold can be seen. The eutectic solder contains dark regions corresponding to the δ phase of gold-tin and the lighter region surrounding the δ phase is the ζ' phase of gold tin. In the layer of pure gold that has been electroplated to the steel, there are a few voids present in the electroplated film. These voids could have arisen during the electroplating process, as larger metal grains form with applied current densities applied, as discussed in Section 2.4.3. After bonding, the cross section of an identically prepared and bonded sample shows that the SLID process does occur and there is a cohesive joint formed between the silicon carbide and steel substrates. EDX analysis of the layers before the bond verified that the composition of the electroplated layers on the silicon carbide and stainless steel substrates were indeed pure gold and that the eutectic solder composition was correct. Following the bonding, spot analyses set 5 µm apart from one another were performed to determine the composition of the bond as a function of vertical position in the bonding stack. Layers of pure gold were present on either side of the SLID bonding region, where the ζ' phase of gold-tin was formed. The proportions of pure gold on either side of the SLID bond layer to the ζ' gold-tin intermetallic corresponded to what had been modeled in the simulations of Chapter 3.

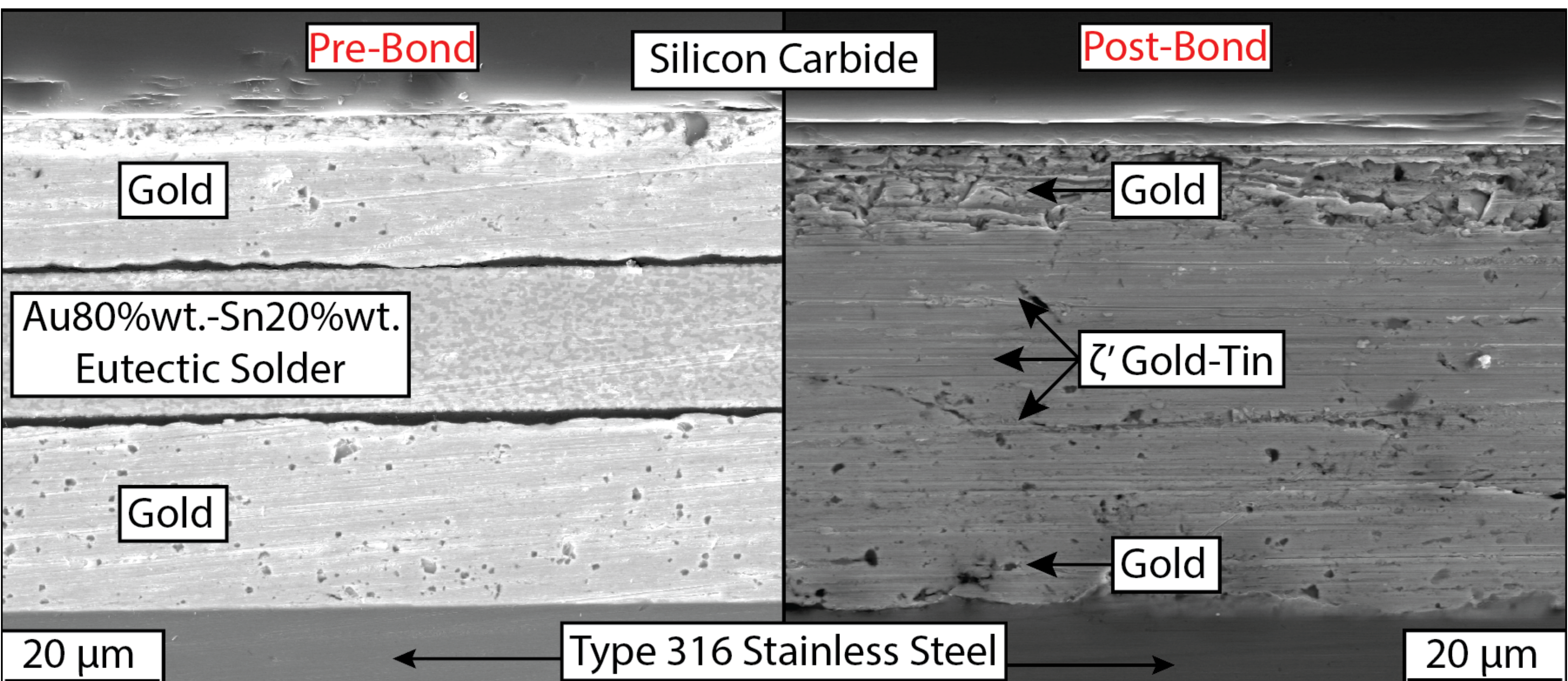

Figure 4.9: An SEM image of the SLID Bond before bonding, left, and after bonding, right, shows how the diffusion of the gold into the tin layer occurs and how the composition of the bond changes after being subjected to the SLID bonding process.

After investigating the cross section and seeing how the diffusion of the gold into the eutectic solder was distributed in the bond, the fracture surfaces of the bond were investigated on both the silicon carbide side as well as the stainless steel side. Using the FEI Quanta SEM and the Oxford EDX the fracture surfaces were analyzed and compositional analyses were performed on various parts of the fracture surface. With an understanding of how the materials were distributed through the bond from the cross-sectional analysis, looking at the fracture surface would provide insight as to where the bond failed and what parts of the bond were the weakest. Example top-down SEM images taken of the fracture surfaces of the stainless steel and silicon carbide halves of the bond are shown in Figures 4.10 and 4.11 respectively. The material composition of the different features in the Figures were determined using EDX analysis.

From the fracture surface analysis, in the strongest of the bonds tested, it was made apparent that both cohesive and adhesive failures occurred in the bond. On the steel sides of the bonds, in some regions within the bonding area, bare stainless steel was found, indicating that the adhesive Nickel Strike and gold layer had been sheared off. Gold was also found adhered to the stainless steel in other areas, indicating that there were some adhesive failures withing the gold layer that was electroplated onto the stainless steel. Some peeling of the ζ' gold-tin was observed, indicating that there could have been an adhesive failure between the gold tin intermetallic and the pure gold layer or a cohesive failure within the ζ' intermetallic. Due to the accuracy limitations of the EDX it was difficult to determine the extent of the particular separation. Higher up in the bonding stack, pure gold with a trace of titanium was found, signaling that the electroplated gold had come off the silicon carbide die. Because not all the gold from the silicon carbide die had been torn off, there was some cohesive failure in the gold film.

Looking to the surface of the silicon carbide die to verify the findings, the same trends in cohesive and adhesive failures were noticed. There was shearing of the SLID bond layers off the silicon carbide substrate in areas, as was noticed from the inspection of the stainless steel sample. Similarly, in some areas on the silicon carbide die, the electroplated gold from the stainless steel sample was found. For these strong bonds, the multiple types of adhesive and cohesive failures are characteristic of a strong bond, as when failure occurs, it does not simply occur in one material interface, but in a variety of locations and in a variety of materials. Intermetallic alloys, such as the β phase and ζ phases of gold-tin have a reputation for being somewhat brittle, however, as demonstrated by the methods of failure encountered from this testing, there is some evidence that they are more robust than how they are typically viewed in literature, as argued by Lee *et al.* [82].

Analyzing the fracture surfaces for the cases with the weakest bonds, the failure seemed to occur most often from the adhesion of the gold layer to the stainless steel, in spite of the nickel strike efforts to improve adhesion. Though the same processing steps were used for the investigation across all of the stainless steel samples, it is possible that the electroplating process used for fabricating the steel side of the bond experienced issues that were not encountered with the electroplating of the silicon carbide. The plating area of the steel sample was $31.67\,\text{mm}^2$ while the area of the silicon carbide sample was $529\,\text{mm}^2$ and although the same current densities were used, mass transport of the electrolyte to the steel surface due to the patterning of the thick photoresist mask could have been affected. Additionally, the difference in anode to cathode surface areas could have resulted in the differences

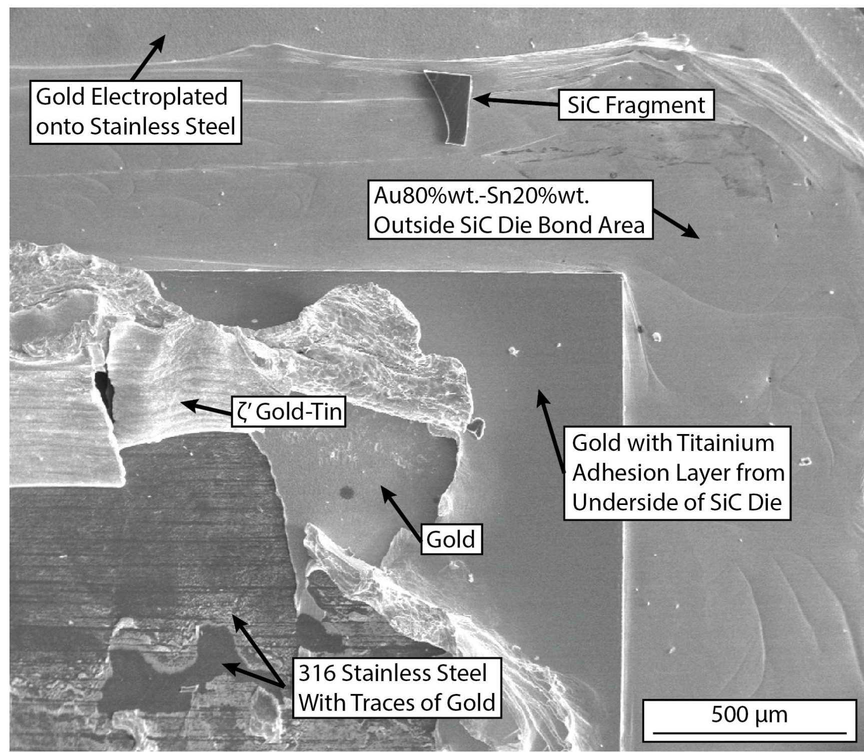

Figure 4.10: An inspection of the fracture surface on the stainless steel half of the bond revealed compositions at the location of failure as well as some information bout the types of failure modes. Cohesive failures were noticed within the ζ' gold-tin layer in addition to adhesive failures between the gold and the stainless steel, and the titanium and silicon carbide die.

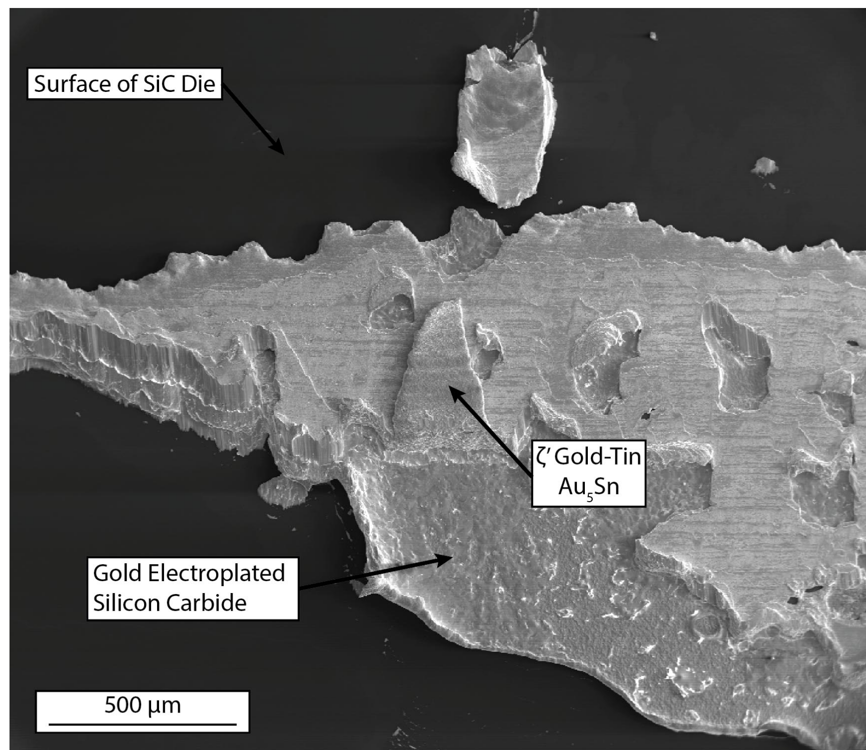

Figure 4.11: An inspection of the fracture surface on the silicon carbide half of the SLID bond confirmed that there was adhesive failure within the ζ' gold-tin layer as well as adhesive failure of the titanium layer on the silicon carbide substrate.

encountered.

4.4.3 Die Shear Testing of SiC to Steel Bonds after High Temperature Aging

To investigate the effects of prolonged exposure to high temperatures that would be characteristic of geothermal well environments, high temperature aging was performed in ambient atmospheric conditions using the Thermo Scientific Thermolyne furnace shown in Figure 4.12. The furnace was designed with a thermocouple feedthrough that was used to manually connect a k-type thermocouple to the samples being tested and to ensure that the proper temperatures were being applied to the samples. The samples were placed on a larger stainless steel block that was placed inside the high temperature furnace. This block acted as a heat-sink and was intended to provide some thermal stability to the dies during the exposure and retard any thermal fluctuations caused by the heater's periodic heating to maintain a constant temperature. The high temperature heating recipe consisted of raising the temperature to 386 °C at a rate of $25\,°\mathrm{C\,min}^{-1}$. In this investigation the slow heating rate was used to ensure that the furnace would not significantly overshoot the desired holding temperature. The temperature was held at 386 °C for a duration of 100 hours. After 100 hours, the composition of the SLID bond would have reached equilibrium and homogenization would have completed [37].

In the high temperature aging investigation, the two sets of samples tested both had 20 µm thick gold metallizations on the stainless steel substrate and 40 µm thick gold metallizations on the silicon carbide dies, but one set of samples was bonded with 5 µm thick eutectic solder preforms and the other set was bonded with 12.7 µm thick preforms. The bonding technique used for bonding these samples were the same as discussed in Section2.4.5.

Die shear testing was performed on the aged samples to determine if the aging process affected the strength of the bond; however, the die shear tests were performed at room temperature. In the testing of the aged samples, there was no apparent decrease in bond strength of the samples in comparison with those that had been tested after cooling, with no further processing after bonding. In fact, out of the aged group of samples tested, one sample with 20 µm thick gold plating on the steel, 40 microm gold plating on the silicon carbide and a 5 µm thick eutectic solder preform, demonstrated the second highest recorded die-shear strength, with a 431.7 N shear load (an equivalent shear stress of 29.9 MPa. In all the cases of die shear testing the high temperature aged, the samples all surpassed the 2.0× Mil-STD 883J requirement.

The compositional change and homogenization of the bond's cross section was investigated to determine what materials were present. Using regular optical microscopy, as shown in Figure 4.13, it was clearly visible that the bond had homogenized, as the distinction between the ζ' gold-tin layer and the pure gold layer was less pronounced. Before aging, the pure gold layers exhibited a darker yellow luster, while the areas rich in tin exhibited a lighter more silver tone of yellow. After the high temperature aging, the entire bond appeared to be a of a homogeneous composition, and so EDX analysis was used on the cross sections before an after aging, to track the progress of the diffusion.

Before analyzing the cross section of the aged bonds, the periphery of the SLID bonding

Figure 4.12: The Thermo Scientific Thermolyne furnace used for the high temperature aging of bonded samples operated in atmospheric conditions and enabled the use of a external thermocouple to monitor the temperature inside the chamber.

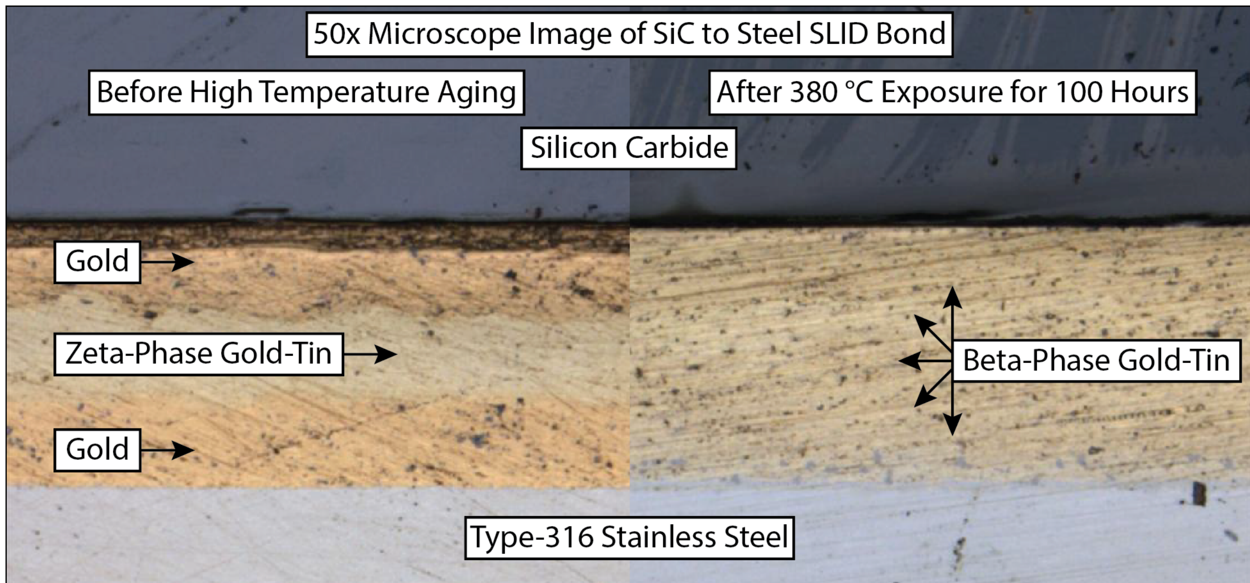

Figure 4.13: Optical images of the SLID bond's cross section before and after high temperature aging show how the bond homogenizes with prolonged exposure to high temperatures.

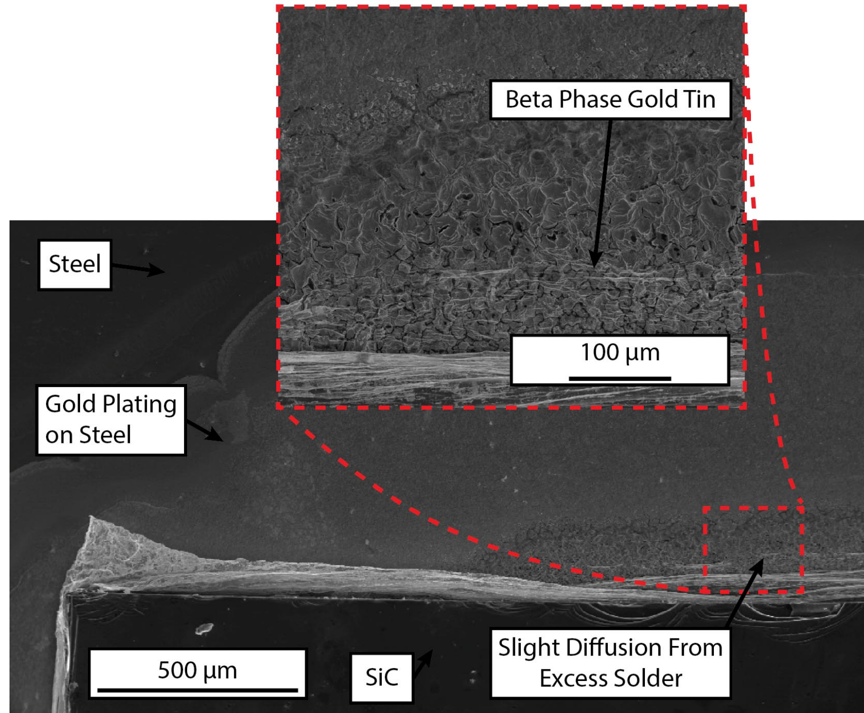

Figure 4.14: The bonded sample was optically inspected after the high temperature aging to determine if the area outside the bonding area was affected. This top-down image of the bond shows diffusion of gold, from the electroplated gold layer on stainless steel, into excess eutectic solder preform that protruded outside the bonding area. No significant external changes that would affect the strength of the bond were found.

area was investigated to see if diffusion from the gold outside the bonding area was contributing to the observed homogenization of the bond. Outside the SLID bonding area, there was noticed a slight roughening in the electroplated gold on the stainless steel. This roughening, which is representative of bulk diffusion of the gold, however, seemed to be caused only by the presence of excess gold-tin eutectic solder preform, hanging over the gold-plated steel substrate abd contacting the electroplated film[69]. The area investigated outside of the bond after 100 hour aging is shown in Figure 4.14. This external diffusion of the excess solder preform and excess gold outside the bonding area did not have any apparent effect on the performance of the bonds.

EDX analysis of the cross sections of the bond, before and after the aging revealed the extent of the diffusion and the material composition within the bond. Figure 4.15 shows a metallographically prepared cross-section of the SLID bond, immediately after bonding. In the analysis, EDX scans were performed approximately 10 µm apart to determine the compositional profile within the bond layer. The SEM image in this figure corresponds to the same non-aged sample that was photographed in Figure 4.13. In this EDX analysis, the findings observed from the optical inspection were confirmed; a pure layer of gold was present at both the silicon carbide and stainless steel interfaces and a ζ' gold-tin layer was present in the middle of the bond. In the aged sample, the measurements from the EDX analysis pointed towards the majority of the bond having a β gold-tin composition, with

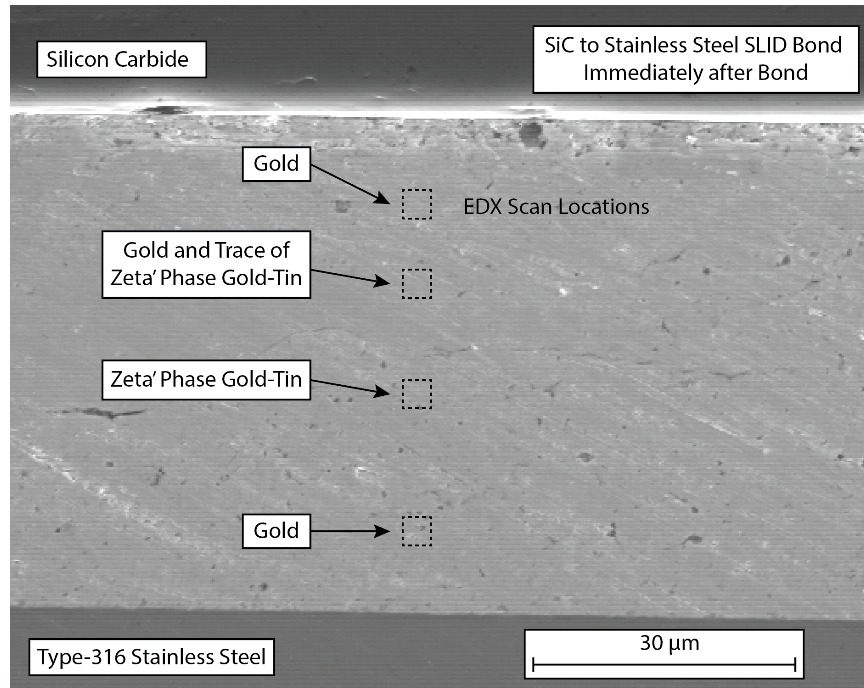

Figure 4.15: Compositional cross sectional analysis of fresh SLID bond using EDX analysis. Immediately after SLID bonding, pure gold films are present at both the silicon carbide and stainless steel interfaces while the material in the center of the bond has formed the ζ' phase of gold-tin.

an atomic percentage makeup of 92.75 % gold and 7.25 % tin. On the phase diagram, this is right along the edge of the β phase gold-tin boundary with pure gold. At the top-most EDX scan location, the measurement taken in atomic percentages was 95.1 % gold, 4.9 % tin. At this topmost region, it is reasonable that due to the spread of the electron beam the initial thickness of the electroplated gold layer on the silicon carbide and the proximity to the silicon carbide layer, this area of the inspected consisted of pure gold with a trace of the beta phase. From the results of the die shear testing and the compositional inspection of the aged samples, it is determined that prolonged exposure to high temperatures homogenizes the composition of the bond, and that homogenized composition is strong enough to surpass the military packaging standards.

4.4.4 Elevated Temperature Loading of SiC to Steel Bonds

As the silicon carbide sensors, bonded to steel, are likely to operate in the high temperature for harsh environments for long periods of time, the strength of the bond at high temperatures was investigated. Mechanical creep is the tendency of a material, such as the SLID bond layer, to deform from the action of a sustained stress. At high temperatures, the rate of mechanical creep under constant loading increases as shown in Equation 4.3, the general equation for creep rate. Where ϵ is the creep strain, CC is a constant that depends on the material and mechanism of creep, m and b are exponents that are dependent on the creep mechanism. Q is the activation energy for the creep mechanism, σ is the applied stress,

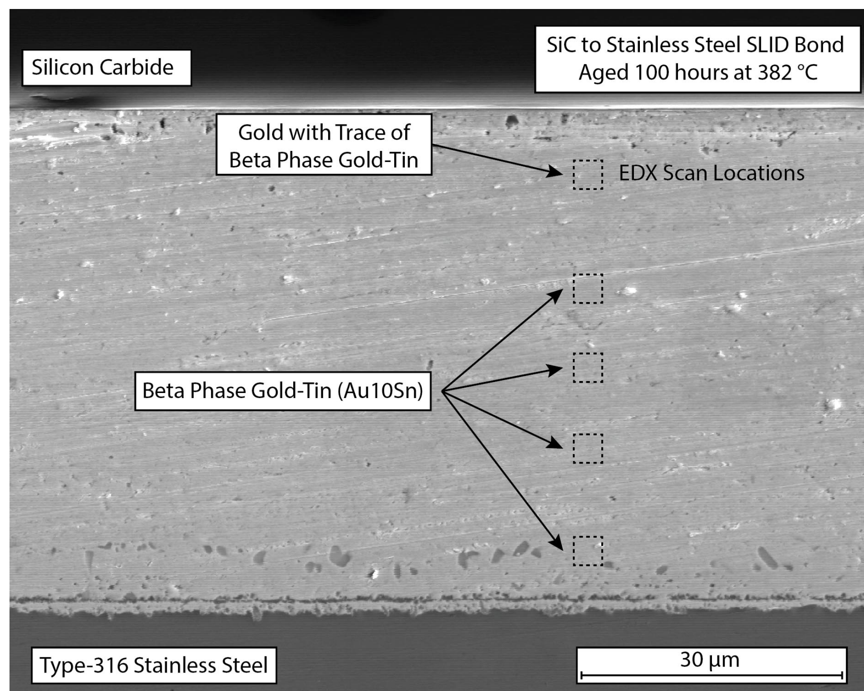

Figure 4.16: Compositional cross sectional analysis of SLID bond after 100 hours of aging at 382 °C using EDX. After prolonged high temperature exposure, the layers of the SLID bond have homogenized but there remains a trace of pure gold with β phase gold-tin near the silicon carbide die, which had a much thicker gold metalization than the steel.

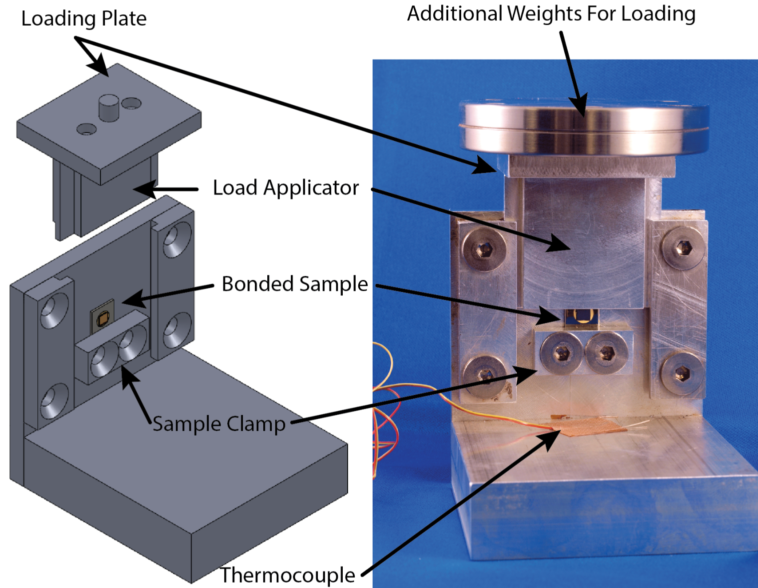

Figure 4.17: Testing apparatus built to apply shear loads to SiC to steel SLID bond at high temperatures in environmental chambers. A shear wedge, capable of accepting additional weights, was used to impart a load to the bonded SiC die during testing.

d is the grain size of the material, T is the absolute temperature given in Kelvin, and k is Boltzmann's constant. From this equation is is clear that as applied stress and temperature are increased, that the rate of creep will also increase [83].

$$\frac{\mathrm{d}\epsilon}{\mathrm{d}t} = \frac{C\sigma^m}{d^b} e^{\frac{-Q}{kT}} \tag{4.3}$$

To evaluate the performance of the SiC to steel SLID bonds, a testing jig, shown in figure 4.17 was developed to apply constant load to the SiC die while being exposed to high temperatures. The loading setup was designed to allow the application of a shear load to the SiC die bonded to stainless steel. To ensure constant load application to the die, weights were used to impart a vertical force for loading, as springs or other mechanical load applicators would soften at the high temperatures and cause fluctuations in loading. A set of guide rails on the vertical section of the testing apparatus to guide the shearing block to the bonded die. A loading applicator was machined to slide along the guides and pass over the stainless steel substrate and SLID bond layer, only applying a distributed load across the flat edge of the SiC die, as shown in Figure 4.18. The tolerances of the setup were designed to have enough slop to accomodate for the thermal expansion and potential warping of the components. Prior to testing the samples in the jig, the jig was heated to 415 °C to ensure that it could operate freely at high temperatures. Additionally, a k-type thermocouple was bonded to the testing jig to monitor the temperature of the component during high temperature testing.

The testing apparatus was built using 6061 Aluminum, limiting the maximum operating temperature of the tester to below 530 °C [84], and was designed to hold the bonded SiC to steel sample, perpendicularly oriented to the load applicator and mounted vertically against the upright of the testing jig. To ensure proper alignment of the load applicator to the die,

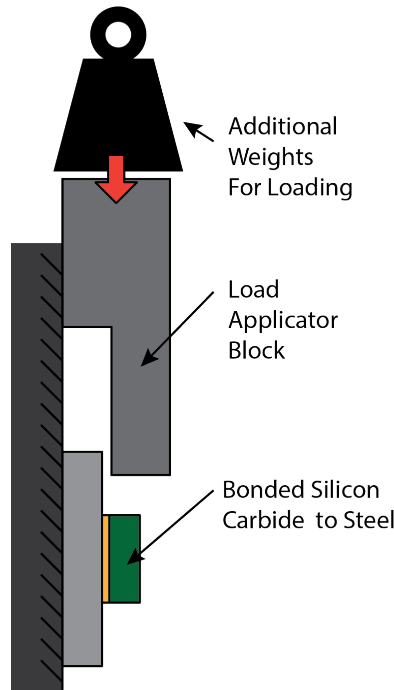

Figure 4.18: Operation of the high temperature die shear testing apparatus. The load-applicator block passes over the stainless steel substrate and contacts the SiC die.

the dies were loosely clamped and allowed to shift and rotate while the load applicator was brought into contact with the dies. After good contact was ensured, the dies were clamped into place. Stainless steel flat-head screws were used to secure the components of the testing jig together.

The high temperature creep testing began with loading the die with an applied mass of 24.5 g, which would apply a shear stress of 16.64 kPa to the sample's bond area, and bringing the testing chamber up to 200 °C. A Thermal Product Solutions Tenny Junior environmental testing chamber with a maximum operating temperature of 200 °C was use to perform the heating for the initial creep testing. The temperature was held constant for 7 hours at this temperature before cooling back down to 25 °C. Upon inspection of the die under a microscope, the die seems completely intact, and so the load was increased for further creep testing. Using the same sample, the load was increased to 772.8 g, which would impart a shear force of 525.0 kPa. The loaded testing jig was placed back in the furnace and brought back to a temperature of 200 °C and held at temperature for an additional 10 hours. After returning the testing setup to room temperature, the bond was inspected once more using an optical microscope and no noticeable damage or sliding of the bond was observed.

With the bond having survived the loads, durations and temperatures, the applied load was further increased as was the temperature. A load of 1009.0 g was applied to the top of the shearing block using stainless steel rounds and an additional CF vacuum flange. The testing jig was then placed in the Thermo Scientific Thermolyne furnace and gradually brought to a temperature of 416 °C over 1 hour, and held at a constant 416 °C for 100 hours. The high temperature creep testing of the sample in the Thermolyne furnace is shown in

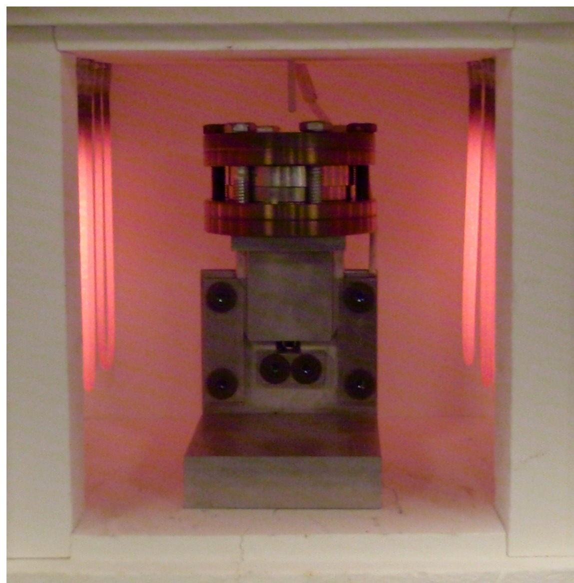

Figure 4.19: The high temperature loading apparatus, loaded with 1009 g of mass, was placed into a Thermo Scientific Thermolyne furnace and brought to a temperature of 423 °C for 100 hours to test mechanical creep of the SLID bond.

Figure 4.19. Due to the size limitations of the furnace, increasing the applied load by using more weights was not feasible and so the temperature was increased instead, as loading with the same weight at a higher temperature would produce an increased strain rate. By raising the temperature within 110 °C of the melting point of the material, and by loading the sample for 100 hours, it was expected that the bond would fail; however, it survived. Optical inspection of the bond of this bond showed no significant change in the bond or sliding of the die. Optically, the only noticeable differences were the diffusion of the excess Au80%wt.-Sn20%wt. solder into the excess electroplated gold, outside the bond area. This was the same characteristic encountered during the aging tests of the bond, indicating the homogenization of the bond due to the prolonged exposure to 416 °C.

4.4.5 High Temperature Exposure Testing of SiC to Steel SLID Bond

In the interest of verifying the maximum survival temperature of the bond, an investigation of its melting point was performed. To test the melting point of the bond, a sample was bonded using a 12.7 µm gold-tin eutectic preform, silicon carbide electroplated with a 40 µm gold layer and stainless steel electroplated with a 20 µm gold layer. Following the bonding, and before testing the melting temperature, the bonded samples were not aged, so the composition of the bond would have been the same as the samples discussed in Section 4.1, with ζ' gold-tin sandwiched between excess gold layers.

A k-type thermocouple was bonded to the stainless steel, using thermocouple adhesive cement from OMEGA Engineering, Inc., to monitor the temperature of the bond. A Research, Inc. SpotIR Model 4085 infrared heater lamp was used to heat the sample. After

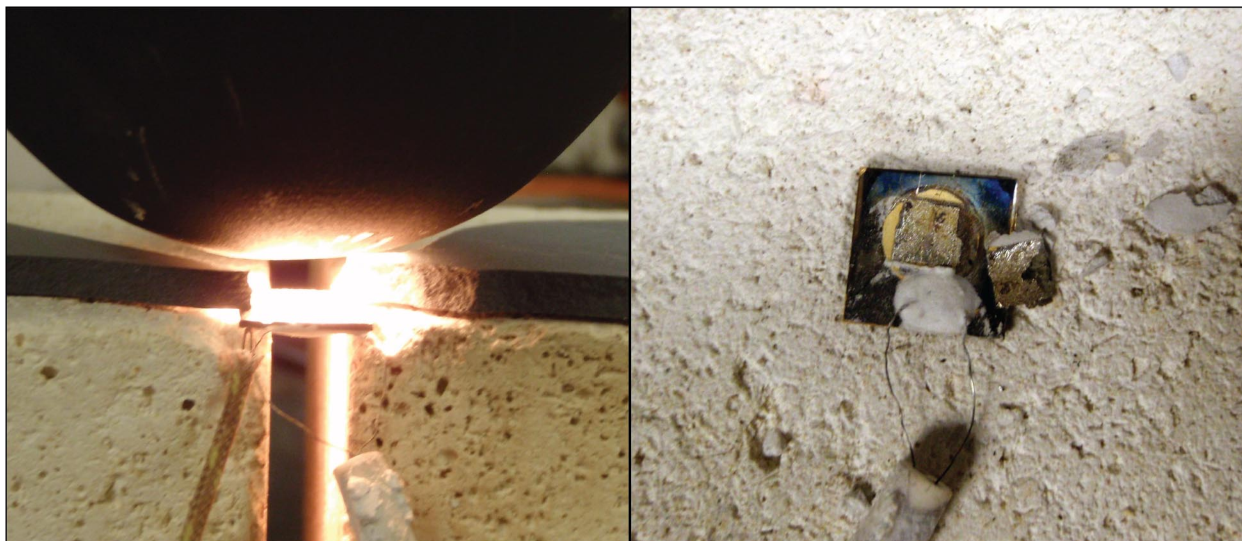

Figure 4.20: An infrared lamp was used to heat the sample to its ultimate melting point to demonstrate bond survivability up to the melting point, shown on the left. A thermocouple was bonded to the stainless steel substrate to monitor the temperature experienced by the bond. On the right, after the melting point of the bond layer was reached, 520 °C ±5 °C, the silicon carbide die fell off the steel substrate.

the bonding of the thermocouple was performed, the sample was placed upside-down, suspended between two ceramic cinder-blocks, as shown in Figure 4.20. The temperature of the substrate was monitored with a Stanford Research SR630 Thermocouple reader. The power supplied to the IR lamp was slowly ramped and the samples were steadily heated. As the samples were heated, a small force, applied manually with wafer tweezers, was used to try to slide the silicon carbide off the stainless steel. Before each contact, the tweezers were also heated under the IR Lamp, to reduce the cooling of the bond sample during contact. Only after the samples reached a temperature of 520 °C, did the silicon carbide die detach from the substrate. Other work in literature has shown that the strength of the bond does decrease with high temperatures, and though quantitative measurements of shear force during heating were not possible with the current experimental setup, the minimal force required to slide the silicon carbide die off the stainless steel at 520 °C does support those findings [85].

Chapter 5

Conclusion

In this work, a bonding method for joining silicon carbide to steel for high temperature harsh environment applications has been developed. Using the SLID bonding approach, bonds were formed at temperatures lower than the final operating temperature of the bond. Analytical and finite element analysis simulations were performed to determine the distribution of stresses in the bonds. Bond survival was demonstrated at elevated temperatures and the effects of temperature on the silicon carbide to steel bonds was investigated. This chapter recapitulates the work performed in this thesis and sets forth new areas of research interest for high temperature harsh environment packaging.

5.1 Improving the SLID Bonding of Silicon Carbide to Steel

The SLID bonding of silicon carbide to steel is a process that can greatly benefit many MEMS applications. This work investigated a bonding approach that mitigated the effects of thermally induced strains in trying to bond silicon carbide and steel. Finite element analysis simulations and analytical calculations demonstrated that the stresses would not exceed the limits of the materials used in the bond. Furthermore, work has demonstrated the successful joining of silicon carbide to steel where traditional brazing methods have failed. With the gold-tin material system, using bonding temperatures as low as 300 °C the bond has demonstrated performance at 416 °C and bond survival up to 520 °C. The effects of different bonding parameters and high temperature aging on the strength of the bonds were investigated, and die shear testing of the bonds demonstrated that they surpass the military standard for die shear strengths of microelectronics.

To deepen the investigation into silicon carbide to steel bonding, exposure testing of the bonds in downhole conditions with geothermal brines should be performed. The robustness of the bond under such conditions would confirm the suitability of SLID bonding for such applications. Additionally, this investigation would benefit the bonding of silicon carbide to silicon carbide bonding for MEMS encapsulations applications requiring high temperature survival.

Another area of for investigation would be the improvement of adhesion strength of the SLID bonding materials onto both steel and silicon carbide. In the work performed in

this thesis, an improved electroplating scheme was developed for the electroplating of gold on stainless steel by including a pickling step and a nickel strike, resulting in significantly stronger gold film adhesion. However, as the adhesion of the gold films to the silicon substrate and stainless steel were found to be a location of failure in several of the bonds during die shear testing, the interface between gold and silicon carbide as well as gold and stainless steel are of value.

5.2 Future Works and Directions

Based upon the results found in this work, several new directions of bonding and packaging work for high temperature harsh environment MEMS applications are suggested. Several applications, such as MEMS monitoring on the inside of gas turbines and automotive engines, would benefit from bonds capable of surviving temperatures greater than 600 °C. For these applications, the gold-tin material system with the SLID bonding process would not produce bonds capable of surviving the temperatures. Additionally, depending upon the materials bonded, the CTE mismatch encountered during bonding would introduce significant stresses that would cause the bond to fail. Several suggestions to overcome these issues are provided in this section to push bonds to higher temperatures and greater extremes.

5.2.1 SLID Bonding with Nanoparticles or Reactive Nano-Layers

One key aspect of interest with the use of nanoparticles is that the melting point of the nanoparticles depends on their size [86, 87]. With the melting point dependence on size, particles of materials suitable for SLID bonding could be dispersed and mixed onto substrates for suppressed temperature SLID bonding. For examples, nanoparticles of pure tin and pure gold could be mixed in a 3Au:2Sn ratio and designed to melt below the 232 °C melting point of tin. These melted particles could diffuse and form intermetallics with higher melting points. Additionally, if the bonding is performed using nanoparticles, this process could be combined with nanoparticle printing to enable direct-print packaging technologies.

5.2.2 Gradual Layering of Increasing CTE Materials

As one of the main issues with bonding materials mismatched in coefficients of thermal expansion is the thermally induced stresses, one area of investigation for high temperature harsh environment bonding would be SLID bonding with intermediate metal layers. Through the use of materials like molybdenum, which is better matched in CTE with silicon carbide than steel, a gradient of thermally induced strains could be constructed. The use of other materials like nickel superalloys, with extremely low coefficients of thermal expansion could also be investigated for use in such interlayers to change the distribution of thermal stresses in the layers of the bond.

Another option for absorbing the thermally induced stresses would be to select a ductile material to act as an intermediate bonding layer and design the bond such that the material yields to absorb the thermal stress. This particular approach would not work well for the attachment of silicon carbide strain sensors or pressure sensors, as the yielding of the bonding

material would skew the measurements of the sensor; however, for the die-attach applications of inertial sensors and accelerometers, this type of process may hold some potential.

5.2.3 Material Systems for Higher Temperature Bonds (>600 °C)

Lastly, to pursue higher temperatures, above 600 °C, the use of different SLID bonding material systems is of interest. The copper-tin material system boasts several high melting point intermetallic alloys, such as Cu_3Sn with a melting point of 756 °C and $Cu_{0.85}Sn_{0.15}$ with a melting point of 799 °C. Such material systems would still offer the benefit of lowering the temperature used for bonding, while enabling the formation of a robust high-melting point material.

Bibliography

[1] S. Beeby, E. Graham, and M. Kraft. *MEMS Mechanical Sensors*. Artech House, Boston, 2004.

[2] M. W. Chan, D. R. Myers, B. D. Sosnowchik, Lin Liwei, and A. P. Pisano. Localized strain sensing using high spatial resolution, highly-sensitive MEMS resonant strain gauges for failure prevention. In *Solid-State Sensors, Actuators and Microsystems Conference (TRANSDUCERS), 2011 16th International*, pages 2859–2862, 2011.

[3] Wei-Cheng Lien, Debbie G. Senesky, and Albert P. Pisano. 4H-SiC Lateral JFET for Low Power Operational Amplifier Applications. *Electrochemical Society Meeting Abstracts*, (41):3032–3032, 2012.

[4] Philip G. Neudeck, David J. Spry, Liang-Yu Chen, Carl W. Chang, Glenn M. Beheim, Robert S. Okojie, Laura J. Evans, Roger Meredith, Terry Ferrier, and Michael J. Krasowski. 6H-SiC transistor integrated circuits demonstrating prolonged operation at 500 °C. In *IMAPS International Conference and Exhibition on High Temperature Electronics (HiTEC 2008)*, 2008.

[5] Philip G. Neudeck, David J. Spry, Liang-Yu Chen, G. M. Beheim, R. S. Okojie, C. W. Chang, R. D. Meredith, T. L. Ferrier, L. J. Evans, M. J. Krasowski, and N. F. Prokop. Stable Electrical Operation of 6H-SiC JFETs and ICs for Thousands of Hours at 500 °C. *Electron Device Letters, IEEE*, 29(5):456–459, 2008.

[6] D. G. Senesky, B. Jamshidi, Cheng Kan Bun, and A. P. Pisano. Harsh Environment Silicon Carbide Sensors for Health and Performance Monitoring of Aerospace Systems: A Review. *Sensors Journal, IEEE*, 9(11):1472–1478, 2009.

[7] M. Mehregany, C. A. Zorman, N. Rajan, and Wu Chien Hung. Silicon carbide MEMS for harsh environments. *Proceedings of the IEEE*, 86(8):1594–1609, 1998.

[8] R. G. Azevedo, Zhang Jingchun, D. G. Jones, D. R. Myers, A. V. Jog, B. Jamshidi, M. B. J. Wijesundara, R. Maboudian, and A. P. Pisano. Silicon carbide coated MEMS strain sensor for harsh environment applications. In *Micro Electro Mechanical Systems, 2007. MEMS. IEEE 20th International Conference on*, pages 643–646, 2007.

[9] R. G. Azevedo, D. G. Jones, A.V. Jog, B. Jamshidi, D. R. Myers, L. Chen, Xiao-an Fu, Mehran Mehregany, M. B. J. Wijesundara, and A. P. Pisano. A SiC MEMS Resonant Strain Sensor for Harsh Environment Applications. *Sensors Journal, IEEE*, 7(4):568–576, 2007.

[10] Pasqualina M. Sarro. Silicon carbide as a new MEMS technology. *Sensors and Actuators A: Physical*, 82(1-3):210–218, 2000.

[11] F. T. Goericke, M. W. Chan, G. Vigevani, I. Izyumin, B. E. Boser, and A. P. Pisano. High temperature compatible aluminum nitride resonating strain sensor. In *Solid-State Sensors, Actuators and Microsystems Conference (TRANSDUCERS), 2011 16th International*, pages 1994–1997, 2011.

[12] Babak Jamshidi. *Poly-Crystalline Silicon Carbide Passivated Capacitive MEMS Strain Gauge for Harsh Environments.* PhD thesis, University of California, Berkeley, 2008.

[13] Gabriele Vigevani, Fabian T. Goericke, Albert P. Pisano, Igor I. Izyumin, and Bernhard E. Boser. Microleverage detf aluminum nitride resonating accelerometer. In *Frequency Control Symposium (FCS), 2012 IEEE International*, pages 1–4. IEEE, 2012.

[14] D. G. Jones, R. G. Azevedo, M. W. Chan, A. P. Pisano, and M. B. J. Wijesundara. Low temperature ion beam sputter deposition of amorphous silicon carbide for wafer-level vacuum sealing. In *Micro Electro Mechanical Systems, 2007. MEMS. IEEE 20th International Conference on*, pages 275–278, 2007.

[15] S. Wodin-Schwartz, J. C. Cheng, D. G. Senesky, J. E. Hammer, and A. P. Pisano. Geothermal environmental exposure testing of encapsulant and device materials for harsh environment MEMS sensors. In *Micro Electro Mechanical Systems (MEMS), 2012 IEEE 25th International Conference on*, pages 432–435, 2012.

[16] State of California. Energy action plan ii: Implementation roadmap for energy policies, October 2005 2005.

[17] Jiri Marek. Trends and challenges in modern mems sensor packages, July 2013.

[18] D. R. Lefebvre, K. M. Takahashi, A. J. Muller, and V. R. Raju. Degradation of epoxy coatings in humid environments: the critical relative humidity for adhesion loss. *Journal of Adhesion Science and Technology*, 5(3):201–227, 1991.

[19] Tai-Ran Hsu. Mems packaging, 2009.

[20] G. Humpston and D. M. Jacobson. *Principles of Soldering and Brazing.* ASM International, 1993.

[21] Thomas J. Moore. Feasibility study of the welding of sic. *Journal of the American Ceramic Society*, 68(6):C–151–C–151, 1985.

[22] J. Turner. *Automotive Sensors.* Momentum Press, 2009.

[23] D. R. Myers and A. P. Pisano. Torque measurements of an automotive halfshaft utilizing a MEMS resonant strain gauge. In *15th International Conference on Solid-State Sensors, Actuators and Microsystems. Transducers 2009*, pages 1726–1729, Denver, CO, USA, 2009. IEEE.

[24] A. Mohan, A. P. Malshe, S. Aravamudhan, and S. Bhansali. Piezoresistive mems pressure sensor and packaging for harsh oceanic environment. In *Electronic Components and Technology Conference, 2004. Proceedings. 54th*, volume 1, pages 948–950 Vol.1, 2004.

[25] Matthew W. Chan. *Localized Strain Sensing Using High Resolution, Highly-sensitive MEMS Resonant Strain Gauges*. Masters, University of California, Berkeley, 2010.

[26] Wenming Tang, Anqiang He, Qi Liu, and Douglas Ivey. Fabrication and microstructures of sequentially electroplated au-rich, eutectic au/sn alloy solder. *Journal of Materials Science: Materials in Electronics*, 19(12):1176–1183, 2008.

[27] Martin A. Schmidt. Wafer-to-wafer bonding for microstructure formation. *Proceedings of the IEEE*, 86(8):1575–1585, 1998.

[28] Z. H. Zhong, T. Hinoki, and A. Kohyama. Joining of silicon carbide to ferritic stainless steel using a w-pd-ni interlayer for high-temperature applications. *International Journal of Applied Ceramic Technology*, 7(3):338–347, 2010.

[29] H. A. Mustain, W. D. Brown, and S. S. Ang. Transient liquid phase die attach for high-temperature silicon carbide power devices. *Components and Packaging Technologies, IEEE Transactions on*, 33(3):563–570, 2010.

[30] T. A. Tollefsen, A. Larsson, O. M. Lovvik, and K. E. Aasmundtveit. High temperature interconnect and die attach technology: Au-sn slid bonding. *Components, Packaging and Manufacturing Technology, IEEE Transactions on*, 3(6):904–914, 2013.

[31] R. A. Lula. *Stainless steel*. American Society for Metals, Materials Park, Ohio, 1985.

[32] M. Mehregany and C. A. Zorman. SiC MEMS: opportunities and challenges for applications in harsh environments. *Thin Solid Films*, 355-356:518–524, 1999. doi: DOI: 10.1016/S0257-8972(99)00374-6.

[33] Benvenuto Cellini. *Due Trattati, uno inorno alle otto principali arti del l'oreficiera. L'altro in material dell'arte della scultura*. Florence, 1568.

[34] Jochem Wolters. The ancient craft of granulation. *Gold Bulletin*, 14(3):119–129, 1981. Gold Bull.

[35] Isaac Tuah-Poku, M. Dollar, and T. B. Massalski. A study of the transient liquid phase bonding process applied to a ag/cu/ag sandwich joint. *Metallurgical and Materials Transactions A*, 19(3):675–686, 1988.

[36] Y. Zhou, W. F. Gale, and T. H. North. Modelling of transient liquid phase bonding. *International Materials Reviews*, 40(5):181–196, 1995.

[37] W. D. MacDonald and T. W. Eagar. Transient liquid phase bonding. *Annual Review of Materials Science*, 22(1):23–46, 1992.

[38] D. S. Duvall, W. A. Owczarski, and D. F. Paulonis. Tlp bonding: a new method for joining heat resistant alloys. *Welding Journal*, 53(4):203–214.

[39] R. R. Wells. Microstructural control of thin-film diffusion-brazed titanium. *Welding Journal*, 55(1):S20–S27, 1976. WELLS, RR.

[40] Byjt Niemann and R. A. Garrett. Eutectic bonding of boron-aluminum structural components. In *Annual Meeting held in Chicago during*, 1973.

[41] Ahmed Elrefaey and Wolfgang Tillmann. Evaluation of transient liquid phase bonding between titanium and steel. *Advanced Engineering Materials*, 11(7):556–560, 2009.

[42] Yu ichi Komizo, Fumio Kashimoto, Toshiro Tomita, and Kazuhiro Ogawa. Diffusion bonding of stainless steel pipes by using fe-base and ni-base interlayer alloys. *QUARTERLY JOURNAL OF THE JAPAN WELDING SOCIETY*, 8(2):197–204, 1990.

[43] W. D. MacDonald and T. W. Eagar. Isothermal solidification kinetics of diffusion brazing. *Metallurgical and Materials Transactions a-Physical Metallurgy and Materials Science*, 29(1):315–325, 1998.

[44] Torleif A. Tollefsen, Andreas Larsson, OleMartin Lovvik, and Knut Aasmundtveit. Au-sn slid bonding-properties and possibilities. *Metallurgical and Materials Transactions B*, 43(2):397–405, 2012. Metall and Materi Trans B.

[45] K. E. Aasmundtveit, K. Wang, N. Hoivik, J. M. Graff, and A. Elfving. Au-Sn SLID bonding: Fluxless bonding with high temperature stability to above 350 °c. In *Microelectronics and Packaging Conference, 2009. EMPC 2009. European*, pages 1–6, 2009.

[46] K. E. Aasmundtveit, Luu Thi Thuy, Nguyen Hoang-Vu, R. Johannessen, N. Hoivik, and Wang Kaiying. Au-Sn fluxless SLID bonding: Effect of bonding temperature for stability at high temperature, above 400 °c. In *Electronic System-Integration Technology Conference (ESTC), 2010 3rd*, pages 1–6, 2010.

[47] T. B. Wang, Z. Z. Shen, R. Q. Ye, X. M. Xie, F. Stubhan, and J. Freytag. Die bonding with au/in isothermal solidification technique. *Journal of Electronic Materials*, 29(4):443–447, 2000. Journal of Elec Materi.

[48] III Welch, W., Chae Junseok, Lee Sang-Hyun, N. Yazdi, and K. Najafi. Transient liquid phase (TLP) bonding for microsystem packaging applications. In *Solid-State Sensors, Actuators and Microsystems, 2005. Digest of Technical Papers. TRANSDUCERS '05. The 13th International Conference on*, volume 2, pages 1350–1353 Vol. 2, 2005.

[49] C. C. Lee, C. Y. Wang, and G. S. Matijasevic. A new bonding technology using gold and tin multilayer composite structures. *Components, Hybrids, and Manufacturing Technology, IEEE Transactions on*, 14(2):407–412, 1991.

[50] Chuan Seng Tan, Ronald J. Gutmann, L. Rafael Reif, A. Munding, H. Hubner, A. Kaiser, S. Penka, P. Benkart, and E. Kohn. Cu/sn solid-liquid interdiffusion bonding. In *Wafer Level 3-D ICs Process Technology*, Integrated Circuits and Systems, pages 1–39. Springer US, 2008.

[51] Leonard Bernstein. Semiconductor Joining by the Solid-Liquid Interdiffusion (SLID) Process: I . The Systems Ag-In, Au-In, and Cu-In. *Journal of The Electrochemical Society*, 113(12):1282–1288, 1966.

[52] Liu He, G. Salomonsen, Wang Kaiying, K. E. Aasmundtveit, and N. Hoivik. Wafer-level cu/sn to cu/sn slid-bonded interconnects with increased strength. *Components, Packaging and Manufacturing Technology, IEEE Transactions on*, 1(9):1350–1358, 2011.

[53] R. W. Chuang and C. C. Lee. Silver-indium joints produced at low temperature for high temperature devices. *Components and Packaging Technologies, IEEE Transactions on*, 25(3):453–458, 2002.

[54] W. C. Welch and K. Najafi. Gold-indium transient liquid phase (tlp) wafer bonding for mems vacuum packaging. In *Micro Electro Mechanical Systems, 2008. MEMS 2008. IEEE 21st International Conference on*, pages 806–809, 2008.

[55] Goran S. Matijasevic, Chin C. Lee, and Chen Y. Wang. Au-sn alloy phase diagram and properties related to its use as a bonding medium. *Thin Solid Films*, 223(2):276–287, 1993. doi: 10.1016/0040-6090(93)90533-U.

[56] Torleif A. Tollefsen, Maaike M. Visser Taklo, Knut E. Aasmundtveit, and Andreas Larsson. Reliable ht electronic packaging - optimization of a au-sn slid joint. In *Electronic System-Integration Technology Conference (ESTC), 2012 4th*, pages 1–6, 2012.

[57] Brian F. Dyson. Diffusion of gold and silver in tin single crystals. *Journal of Applied Physics*, 37(6):2375–2377, 1966.

[58] Liang Yin, Stephan J. Meschter, and Timothy J. Singler. Wetting in the au-sn system. *Acta Materialia*, 52(10):2873–2888, 2004.

[59] H. Okamoto. Au-sn (gold-tin). *Journal of Phase Equilibria and Diffusion*, 28(5):490–490, 2007. J Phs Eqil and Diff.

[60] J. Tsai, C. Chang, Y. Shieh, Y. Hu, and C. Kao. Controlling the microstructure from the gold-tin reaction. *Journal of Electronic Materials*, 34(2):182–187, 2005.

[61] Yan Bohan, Wang Chunqing, and Zhang Wei. The microstructure of eutectic au-sn and in-sn solders on au/ti and au/ni metallizations during laser solder bonding process for optical fiber alignment. In *High Density Microsystem Design and Packaging and Component Failure Analysis, 2006. HDP'06. Conference on*, pages 298–303, 2006.

[62] Basudev Lahiri, Rafal Dylewicz, Richard M. De La Rue, and Nigel P. Johnson. Impact of titanium adhesion layers on the response of arrays of metallic split-ring resonators (SRRs). *Opt. Express*, 18(11):11202–11208, May 2010.

[63] A. K. Graham and H. L. Pinkerton. *Electroplating Engineering Handbook*. John Wiley & Sons, Incorporated, 1971.

[64] W. B. Hogaboom and G. B. Hogaboom. *Principles of Electroplating and Electroforming, Third Edition.*

[65] Y. Okinaka, F. B. Koch, C. Wolowodiuk, and D. R. Blessington. "polymer" inclusions in cobalt-hardened electroplated gold. *Journal of The Electrochemical Society*, 125(11):1745–1750, 1978.

[66] Silvana Dimitrijevic, M. Rajcic-Vujasinovic, and V. Trujic. Non-cyanide electrolytes for gold plating - a review. *Int. J. Electrochem. Sci*, 8:6620–6646, 2013.

[67] J. W. Dini and H. R. Johnson. Plating on stainless steel alloys. Technical report, Lawrence Livermore National Lab., CA (USA); Sandia National Labs., Livermore, CA (USA), 1981.

[68] E. Zakel and H. Reichl. Au-sn bonding metallurgy of tab contacts and its influence on the kirkendall effect in the ternary cu-au-sn. *Components, Hybrids, and Manufacturing Technology, IEEE Transactions on*, 16(3):323–332, 1993.

[69] John A. Thornton and D. W. Hoffman. Stress-related effects in thin films. *Thin Solid Films*, 171(1):5–31, 1989.

[70] P. M. Hall, F. L. Howland, Y. S. Kim, and L. H. Herring. Strains in aluminum-adhesive-ceramic trilayers. *Journal of Electronic Packaging*, 112(4):288–302, 1990.

[71] S. Timoshenko and J. N. Goodier. *Theory of Elasticity, by S. Timoshenko and JN Goodier.* McGraw-Hill Book Company, 1951.

[72] John A. Carlisle, N. Moldovan, Xingcheng Xiao, C. A. Zorman, D. C. Mancini, B. Peng, H. D. Espinosa, Thomas Aquinas Friedmann, and Orlando Auciello. *A comparison of mechanical properties of three MEMS materials - silicon carbide, ultrananocrystalline diamond, and hydrogen-free tetrahedral amorphous carbon (Ta-C).* 2004.

[73] Philip D. Harvey. *Engineering properties of steel.* American Society for Metals, Metals Park, Ohio, 1982.

[74] Rong An, Chunqing Wang, and Yanhong Tian. Determination of the elastic properties of au5sn and ausn from ab initio calculations. *Journal of Electronic Materials*, 37(7):968–974, 2008.

[75] F. G. Yost, M. M. Karnowsky, W. D. Drotning, and J. H. Gieske. Thermal expansion and elastic properties of high gold-tin alloys. *Metallurgical Transactions A*, 21(7):1885–1889, 1990.

[76] David Tabor. *The hardness of metals.* Oxford University Press, New York, 1951.

[77] Howard E. Boyer. *Atlas of stress-strain curves.* ASM International, Metals Park, Ohio, 1987.

[78] W. N. Sharpe, G. M. Beheim, L. J. Evans, N. N. Nemeth, and O. M. Jadaan. Fracture strength of single-crystal silicon carbide microspecimens at 24 °c and 1000 °c. *Microelectromechanical Systems, Journal of*, 17(1):244–254, 2008.

[79] United States of America - Department of Defense. MIL-STD-883J - Test Method Standard Microcircuits. 2013.

[80] Donald C. Zipperian. *Metallographic Handbook*. PACE Technologies, USA, Tucson, Arizona, 2011.

[81] Nist Sematech. Engineering statistics handbook, 2006.

[82] C. C. Lee, P. J. Wang, and J. S. Kim. Are intermetallics in solder joints really brittle? In *Electronic Components and Technology Conference, 2007. ECTC '07. Proceedings. 57th*, pages 648–652, 2007.

[83] J.A. Collins. *Failure of Materials in Mechanical Deisgn: Analysis, Prediction, Prevention*. John Wiley & Sons, Incorporated, New York, 1993.

[84] A. S. M. International Handbook Committee. ASM Handbook, Volume 02 - Properties and Selection: Nonferrous Alloys and Special-Purpose Materials, 1990.

[85] Torleif Andre Tollefsen, OleMartin Lovvik, Knut Aasmundtveit, and Andreas Larsson. Effect of temperature on the die shear strength of a au-sn slid bond. *Metallurgical and Materials Transactions A*, 44(7):2914–2916, 2013. Metall and Mat Trans A.

[86] K. K. Nanda, S. N. Sahu, and S. N. Behera. Liquid-drop model for the size-dependent melting of low-dimensional systems. *Physical Review A*, 66(1):013208, 2002.

[87] W. H. Qi and M. P. Wang. Size and shape dependent melting temperature of metallic nanoparticles. *Materials chemistry and physics*, 88(2):280–284, 2004.

Appendix A

ANSYS Code for Thermal Strain Modeling of SLID Bond

A.1 MATLAB Script for Calculating SLID Bond Layer Thicknesses and Compositions

```
%SLIDlayers.m
%SLID Layer Composition Effective Thicknesses
clear all, clc,
PreformThickness=5 %microns, use 12.7 for other preform

MAu=196.966;    %g/mol
MSn=118.710;    %g/mol
rhoAu=19.3;     %g/cm^3
rhoSn=5.769; %g/cm^3

PercentAu=.707     %atomic percentage of Gold. 0.707 =80Au/20Sn Slder

A=[1, 1; ((PercentAu-1)*(rhoAu/MAu)), (PercentAu*(rhoSn/MSn))];
B=[PreformThickness;0];
x=A\B;

GoldThickness=x(1)
TinThickness=x(2)
```

A.2 MATLAB Script for Analytical Model of In-Plane Stresses

```
%%%Calculation of stress in n layers%%%
clear all; clc;
%Layer 1            1095 STEEL
```

```
E(1)=     193E9;    %Pa
nu(1)=    0.27;     %no units
alpha(1)= 15.9E-6;  %1/degC
thick(1)= .030*.0254;%m
z(1)=thick(1);      %z is the z-pos at the top of the layer...
%Layer 2            Au
E(2)=     79E9;     %Pa
nu(2)=    0.42;     %no units
alpha(2)= 14.4E-6;  %1/degC
thick(2)= 14.5E-6;     %m
z(2)=thick(2)+z(1);
%Layer 3            Au5Sn Solder Layer
E(3)=     78E9;    %Pa
nu(3)=    0.398;   %no units
alpha(3)= 18E-6;  %1/degC
thick(3)= 11E-6;   %m
z(3)=z(2)+thick(2);
z(3)=thick(3)+z(2);
%Layer 4            Au
E(4)=     79E9;     %Pa
nu(4)=    0.42;      %no units
alpha(4)= 14.4E-6;  %1/degC
thick(4)= 14.5E-6;    %m
z(4)=z(3)+thick(3);
z(4)=thick(4)+z(3);
%Layer 5            Silicon Carbide
E(5)=     530E9;    %Pa
nu(5)=    0.2045;   %no units
alpha(5)= 5.12E-6;  %1/degC
thick(5)= 520E-6;   %m
z(5)=z(4)+thick(4);
z(5)=thick(5)+z(4);
h=sum(thick);       %total thickness, m
%deltaT=            %Tf-Ti = Change in temp degC  -51to Geothermal
  %Operating 374C +96 to 521 MAX
% deltaT=25-300; %delta T = 25C-290C = -265C
deltaT=375-300;
%Establish A coefficient
A=[0 0 0];
for k=1:3
    for ii=1:length(E)
        dummy(ii)=(E(ii)/(1-nu(ii)))*z(ii)^k;
        A(k)=dummy(ii)+A(k);
    end
end
```

```
clear dummy;
%Establish B coefficient
B=[0 0 0];
for k=1:3
    for ii=1:length(E)
        if ii-1==0
            dummy(ii)=0;
        else
            dummy(ii)=(E(ii)/(1-nu(ii)))*z(ii-1)^k;
        end
        B(k)=dummy(ii)+B(k);
    end
end
clear dummy;
%Establish C coefficient
C=[0 0];
for k=1:2
    for ii=1:length(E)
        dummy(ii)=(E(ii)/(1-nu(ii)))*alpha(ii)*z(ii)^k;
        C(k)=dummy(ii)+C(k);
    end
end
clear dummy;
%Establish D coefficient
D=[0 0];
for k=1:2
    for ii=1:length(E)
        if ii-1==0
            dummy(ii)=0;
        else
            dummy(ii)=(E(ii)/(1-nu(ii)))*alpha(ii)*z(ii-1)^k;
        end
        D(k)=dummy(ii)+D(k);
    end
end
clear dummy;

%2 equations, two unknowns, Ax=B
bmatrix=[2*h*deltaT*(C(1)-D(1)); 3*h*deltaT*(C(2)-D(2))];
amatrix=[(2*h*(A(1)-B(1)))+B(2)-A(2), (A(2)-B(2));...
    (3*h*(A(2)-B(2)))+(2*B(3))-(2*A(3)), 2*(A(3)-B(3))];
strain=amatrix\bmatrix;
ebot=strain(1);
etop=strain(2);
```

```
%Calculate stress as a function of Z
for ii=1:length(E)
    kk=linspace(z(ii)-thick(ii),z(ii),100);
    sigma=(E(ii)/(1-nu(ii)))*((ebot*(1-kk./h))+(etop*(kk./h))-...
    (alpha(ii)*deltaT));
%    sigma=(E(ii)/(1-nu(ii)))*(ebot+(kk./h)*(etop-ebot)-...
% (alpha(ii)*deltaT));
    if ii==1
        sigma1=sigma;
    elseif ii==2
        sigma2=sigma;
    elseif ii==3
        sigma3=sigma;
    elseif ii==4
        sigma4=sigma;
    elseif ii==5
        sigma5=sigma;
    else
        sigma6=sigma;
    end
end
hold on;
plot(linspace(z(1)-thick(1),z(1),100),sigma1)
plot(linspace(z(2)-thick(2),z(2),100),sigma2)
plot(linspace(z(3)-thick(3),z(3),100),sigma3)
plot(linspace(z(4)-thick(4),z(4),100),sigma4)
plot(linspace(z(5)-thick(5),z(5),100),sigma5)
xlabel('Position in Material Stack from Bottom (m)')
ylabel('In-Plane Stress (Pa)')
hold off;
MaxStresses=[max(sigma1) max(sigma2) max(sigma3) max(sigma4) max(sigma5)]
MinStresses=[min(sigma1) min(sigma2) min(sigma3) min(sigma4) min(sigma5)]
sigmatot=[sigma1, sigma2, sigma3, sigma4, sigma5];
xtotal=[linspace(z(1)-thick(1),z(1),100),linspace(z(2)-...
thick(2),z(2),100),...
    linspace(z(3)-thick(3),z(3),100),linspace(z(4)-...
thick(4),z(4),100),...
    linspace(z(5)-thick(5),z(5),100)];
% xlswrite('MattPhDcalc.xlsx',xtotal.','Cool300ToRmTemp','A1:A500')
% xlswrite('MattPhDcalc.xlsx',sigmatot.','Cool300ToRmTemp','B1:B500')
xlswrite('MattPhDcalc.xlsx',xtotal.','Heat300ToOpr','A1')
xlswrite('MattPhDcalc.xlsx',sigmatot.','Heat300ToOpr','B1:B500')
```

A.3 ANSYS Model Code for Stress Distribution

```
finish !Exit any previous processor
/clear !Clear everything and start from scratch
!UNITS: micrometer,kilogram,micronewton,degC,seconds,miliVolts,miliAmps
/title,SLIDexpansion Quarter Model Small SiC
!seltol,1e-6 !Select within 10 microns.
!Preprocessing: Defining the problem
/prep7 !Enter pre-processor
thisteel=762
thiau=15
thislid=15
thisubs=300
steelwid=5000
slidwid=1900
tempbond=300
tempfinal=25
tempoperate=375
tref,tempbond
antype,static !Type of Analysis
et,1,solid185,,2,,,,,!For ET, refer to Path: // Element Reference
block,0,steelwid,0,steelwid,0,thisteel !Steel Parallel,0.032 in thick
block,0,slidwid,0,steelwid,0,thisteel !Makes it so the steel can be meshed
block,0,steelwid,0,slidwid,0,thisteel !Makes it so the steel can be meshed
vovlap,all
!Pure Au, 5 micron thick
block,0,slidwid,0,slidwid,thisteel,thisteel+thiau
!Au5Sn, 32 micron thick
block,0,slidwid,0,slidwid,thisteel+thiau,thisteel+thiau+thislid
!Pure Au, 5 micron thick
block,0,slidwid,0,slidwid,thisteel+thiau+thislid,thisteel+thiau+...
thislid+thiau
!Sensor Substrate, 550 micron thick
block,0,slidwid,0,slidwid,thisteel+thiau+thislid+thiau,thisteel+thiau ...
+thislid+thiau+thisubs
vglue,all
lsel,s,length,,slidwid
lesize,all,,,20
*use,matpropmattchan.mac
!To check the parameters, run:
!TBLIST,lab,mat ! List the data table
!/XRANGE,0,0.1 ! X-axis of TBPLOT to extend from varepsilon=0 to 0.01
!TBPLOT,BKIN,mat ! Display the data table
!Mesh from Bottom Up
!316 Stainless Steel
```

```
mat,3
vsel,s,loc,z,0,thisteel
vmesh,all
!Pure Au
mat,10
vsel,s,loc,z,thisteel,thisteel+thiau
vmesh,all
!zeta' Gold-Tin Au5Sn
mat,14
vsel,s,loc,z,thisteel+thiau,thisteel+thiau+thislid
vmesh,all
!Pure Au
mat,10
vsel,s,loc,z,thisteel+thiau+thislid,thisteel+thiau+thislid+thiau
vmesh,all
!SiC Properties for the SiC
mat,8
vsel,s,loc,z,thisteel+thiau+thislid+thiau,thisteel+thiau+thislid+...
thiau+thisubs
vmesh,all
!Solution: Assigning loads, constraints, and Solving
nsel,s,loc,x,0
d,all,ux,0
nsel,s,loc,y,0
d,all,uy,0
nsel,s,loc,x,0
nsel,r,loc,y,0
nsel,r,loc,z,0
d,all,uz,0
nsel,all
bf,all,TEMP,tempfinal !set body force load as a temperature change.
finish
/solu
antype,static
allsel
solve
finish
/contour,all,101,0,,640
!The Reheating Phase!
upcoord,1,on
nsel,all
/prep7
bf,all,TEMP,tempoperate !set body force load as a temperature change.
finish
/solu
```

```
antype,static
allsel
solve
finish
/contour,all,101,0,,380
vsel,s,loc,z,0,thisteel
allsel,below,volu
vsel,s,loc,z,thisteel,thisteel+thiau
allsel,below,volu
vsel,s,loc,z,thisteel,thisteel+thiau+thislid
allsel,below,volu
vsel,s,loc,z,thisteel,thisteel+thiau+thislid+thiau
allsel,below,volu
vsel,s,loc,z,thisteel+thiau+thislid+thiau,thisteel+thiau ...
+thislid+thiau+thisubs
allsel,below,volu
```

A.4 ANSYS Macro Code for Material Properties

```
! --- Define standard set of material properties for use in simulations
! ======================================================================
! Materials list:
! 1:  Silicon [anisotropic]
! 2:  Silicon [isotropic]
! 3:  316L Stainless Steel [Bilinear kinematic hardening = elastic-plastic]
! 4:  63Sn-37Pb solder [bilinear kinematic hardening]
! 5:  Aluminum (6061-T6)
! 6:  Nickel [bilinear kinematic hardening]
! 7:  Silicon carbide (TekVac system values)
! 8:  Silicon carbide (CWRU values)
! 9:  Silicon carbide (Di Gao's paper values)
! 10: Gold
! 11: Sn Tin (Torleif's Paper)
! 12: delta-AuSn
! 13: Eutectic AuSn
! 14: zeta'-AuSn
! 15: zeta-AuSn
! 16: beta-AuSn
! 17: 1095 Steel
! 18: Chromium
! 19: 96.5Sn-3.5Ag lead-free solder
! 20: Titanium
! ======================================================================
! Remember, Units are in Microns, Kilograms, Seconds
```

```
! This makes Stresses in MPa (i.e. 166e3 = 166 GPa)
! Setup temperature table
! (not exploiting, but used for setting properties as fcn of temperature)
MPTEMP,1,0,50,100,150,200,250,!MPTEMP,STLOC,T1,T2,T3,T4,T5,T6
MPTEMP,7,300,350,400,450,500,550
MPTEMP,13,600
! --- MATERIAL #1: - Anisotropic Silicon ! Si properties from Kaajakari
MPDATA,dens,1,,2.329e-15 ! MPDATA,Lab,MAT,STLOC,C1,C2,C3,C4,C5,C6
mp,ctex,1,2.6e-6
TB,ANEL,1,1 ! TB,Lab,MAT,NTEMP,NPTS,TBOPT,EOSOPT,FuncName
TBTEMP,0.0 ! TBTEMP,TEMP,KMOD
TBDATA,,166e3,64e3,64e3,0,0,0    ! TBDATA,STLOC,C1,C2,C3,C4,C5,C6
TBDATA,,166e3,64e3,0,0,0,166e3
TBDATA,,0,0,0,80e3,0,0
TBDATA,,80e3,0,80e3,,,
!TBLIST,lab,mat ! List the data table
! --- MATERIAL #2: - Isotropic Silicon ! Si properties from Maluf
MPDATA,EX,2,,160e3
MPDATA,PRXY,2,,0.227
mpdata,dens,2,,2.329e-15
mp,ctex,2,2.6e-6
!MPTEMP,1,0,   !MPTEMP,STLOC,T1,T2,T3,T4,T5,T6
! --- MATERIAL #3: - 316L Stainless Steel
! Steel properties from http://www.azom.com/article.aspx?ArticleID=863
! 193GPa Young's Modulus, 205 MPa Yield stress at 0.2 percent Offset yield
MPDATA,EX,3,,193e3
MPDATA,PRXY,3,,0.30
! 15.9 CTE 0-100 degC, 16.2 0-315 degC, 17.5 0-538 degC from:AZOM1
MP,CTEX,3,15.74e-6,2.430e-9,3.018e-12,
! 16.3 W/m.K Therm Conductivity at 100 degC, 21.5 W/m.K at 500 degC.
!MP,KXX,16.3e6
!MP,KYY,16.3e6
!MP,KZZ,16.3e6
TB,BKIN,3,1,2,1
!!TBTEMP,0.0
TBDATA,,205,3200
! TBPLOT,BKIN,mat ! Display the data table
! --- MATERIAL #4: - 63sn-37pb solder (eutectic)
mpdata,ex,4,,32e3 ! Solder values from MatWeb
mpdata,prxy,4,,0.38
mp,ctex,4,21.6e-6
TB,BKIN,4,1,2,1 ! INTRODUCE BILINEAR KINEMATIC HARDENING
TBDATA,,43,28,,,,
! --- MATERIAL #5: - Aluminum (6061-T6)
mpdata,ex,5,,70e3 ! Aluminum values from Popov
```

```
mpdata,prxy,5,,0.33 ! 241 MPa Yield strength, 300MPa uts @ 0.25
!from http://www.makeitfrom.com/material-data/?for=6061-AlMg1SiCu-Aluminum
! http://asm.matweb.com/search/SpecificMaterial.asp?bassnum=MA6061t6
mp,ctex,5,25.2e-6
TB,BKIN,5,1,2,1
TBDATA,,241,219
! --- MATERIAL #6: Nickel
mpdata,ex,6,,207e3 ! Nickel values from MatWeb
mpdata,prxy,6,,0.31
mp,ctex,6,13e-6
TB,BKIN,6,1,2,1 ! INTRODUCE BILINEAR KINEMATIC HARDENING
TBTEMP,0.0
TBDATA,,59,860,,,,
mp,ctex,6,13e-6
! --- MATERIAL #7: Silicon carbide (using TekVac system properties)
!Silicon carbide values from Moboudian's research papers
mp,CTEX,7,3.21e-6,3.56e-9,1.62e-12
mpdata,ex,7,,700e3    ! Much higher than standard (why?), ~400 GPa
mpdata,prxy,7,,0.3    ! No Poisson value available
! --- MATERIAL #8: Silicon carbide (using CWRU paper values)
!Silicon carbide values from Mehregany's research papers
mpdata,ex,8,,340e3 ! From Trevino, et al. (2005)
mpdata,prxy,8,,0.3 ! No Poisson value available
mp,ctex,8,3.21e-6,3.56e-9,1.62e-12
mpdata,dens,8,,3.2e-15
! They never measured this, it was assumed to be the same as bulk
! --- MATERIAL #9: Silicon carbide (Roya's values) Values from Di Gao
mpdata,ex,9,,740e3
mpdata,prxy,9,,0.227 ! Guess
mp,ctex,9,3.21e-6,3.56e-9,1.62e-12
mpdata,dens,9,,3.2e-15
! They never measured this, it was assumed to be the same as bulk
! --- MATERIAL #10: Gold Values from MatWeb
mpdata,ex,10,,77.2e3
mpdata,prxy,10,,0.42
mp,CTEX,10,27.2e-6 !From Torleif Paper
mp,DENS,10,19.320e-15 !From Torleif Paper
!mpdata,kxx,10,,301e6
!mpdata,kyy,10,,301e6
!mpdata,kzz,10,,301e6
!mp,GXY,10,27.2e3 !From Torleif Paper
!mp,C,10,128e12
TB,BKIN,10,1,2,1 !Values from Emery Paper
!TBTEMP,0.0
TBDATA,,377,1000
```

```
! --- MATERIAL #11: Sn Tin (Torleif's Paper)
mp,DENS,11,7.290e-15
mpdata,ex,11,,41e3
mpdata,prxy,11,,0.33
mp,CTEX,11,22e-6
!mp,GXY,11,16e3
!mpdata,kxx,11,,63e6
!mpdata,kyy,11,,63e6
!mpdata,kzz,11,,63e6
! --- MATERIAL #12: delta-AuSn
mp,DENS,12,11.7e-15
mpdata,ex,12,,78e3
mpdata,prxy,12,,0.3
mp,CTEX,12,14e-6
!mp,GXY,12,25e3
!mpdata,kxx,12,,57e6
!mpdata,kyy,12,,57e6
!mpdata,kzz,12,,57e6
! --- MATERIAL #13: Eutectic AuSn
mp,DENS,13,14.7e-15
mpdata,ex,13,,72e3
mpdata,prxy,13,,0.4
mp,CTEX,13,16e-6
!mp,GXY,13,25e3
!mpdata,kxx,13,,57.3e6
!mpdata,kyy,13,,57.3e6
!mpdata,kzz,13,,57.3e6
! --- MATERIAL #14: zeta'-Au5Sn
mp,DENS,14,16.3e-15
mpdata,ex,14,,69e3
mpdata,prxy,14,,0.4
mp,CTEX,14,18e-6
!mp,GXY,14,22e3
! --- MATERIAL #15: zeta-AuSn 0.85-0.15 at.%
mpdata,ex,15,,58e3
mpdata,prxy,15,,0.4
!mp,GXY,15,20e3
mp,CTEX,15,20e-6
! --- MATERIAL #16: beta-AuSn
mpdata,ex,16,,88e3
mpdata,prxy,16,,0.33
mp,ctex,16,14e-6 !***GUESS***
! --- MATERIAL #17: 1095 Steel Data from MatWeb
mpdata,ex,17,,205e3
mpdata,prxy,17,,0.29
```

```
mpdata,dens,17,,7.85e-15
mp,ctex,17,11.4e-6
! --- MATERIAL #18: Chromium
mpdata,ex,18,,248e3 ! Chromium values from MatWeb (recrystallized Cr)
mpdata,prxy,18,,0.3 ! No value for Poisson ratio found
mp,ctex,18,8.2e-6 !Ranges from 4.9-8.2
! --- MATERIAL #19: 96.5Sn-3.5Ag lead-free solder
mpdata,ex,19,,26.2e3
mpdata,prxy,19,,0.3 ! Not known, taken as 0.3
mpdata,dens,19,,7.5e-15
mp,ctex,19,21.7e-6
TB,BKIN,19,1,18,1   ! INTRODUCE BILINEAR KINEMATIC HARDENING
TBDATA,,22.5,26.7,,,,         !  (E.G. ELASTIC-PLASTIC BEHAVIOR)
! --- MATERIAL #20: Titanium
mpdata,ex,20,,116e3
mpdata,prxy,20,,0.32
mp,CTEX,20,8.6e-6
mpdata,dens,20,,4.51E-15
!mp,GXY,20,44e3
```

A.5 MATLAB Script for Calculating SLID Bond Area in Si-to-Si Bond

```
%TLP3-3-Middle_1000x.jpg
Solderarea=295.38+78.34+110.87+9.08+69.28+317.42+21.43+23.18+14.70+20.84;
Scanarea=69.50*55.59; %um^2
midTLP33=Solderarea/Scanarea
clear
%TLP6-6_surface_measured250x_BottomCorner.jpg
Solderarea=17+29.41+11.92+96.34+76.22+104.24+247.46+406.67+79.51+...
    29.72+108.45+44.60+91.82+163.65+106.22+55.96+52.16+19.59+29.08+...
    68.15+77.08+31.56+44.96+39.35+37.31+79.26+18.70+32.29+21.74+8.76+...
    61.68+27.85+39.24+86.46+58.8;
Scanarea=66.15*104.19; %um^2
botcorTLP66=Solderarea/Scanarea
clear
%TLP6-6_Surface_measured1000x_AboveMiddleAwaySquare.jpg
Solderarea=13.59+17.43+85.42+274.36+35.64+85.99+35+117.84+50.97+90.03+...
    100.75+70.87+36.32+19.79+75.04+9.42+15.82+13.57+15.42+2.97;
Scanarea=69.5*55.59; %um^2
midtopTLP66=Solderarea/Scanarea
%TLP6-6_Surface_measured1000x_Bottom.jpg
Solderarea=17.34+31.58+140.37+71.02+156.09+63.64+75.25+67.56+51.14+63.40+...
```

```
    57.49+113.19+187.85+60.64+64.03+20.17;
Scanarea=55.59*69.50;
botTLP66=Solderarea/Scanarea
%TLP6-6_Surface_measured1000x_MiddleOfSample.jpg
Solderarea=19.06+22.92+64.26+28.78+116.67+48.30+69.63+44.54+39.17+...
    11.52+14.07+90.54+60.80+12.02+35.8+116.96+67.83+186.13+83.55+35.14;
Scanarea=55.59*69.50;
midTLP66=Solderarea/Scanarea
%TLP6-6_Surface_measured1000x_Top.jpg
Solderarea=34.48+8.4+29.94+137.39+105.20+51.25+15.36+47.48+190.77+...
    80.44+17.84+70.4+37.39+32.2+65.35+21.2+85.37+116.6+41.12+32.65+54.04;
Scanarea=55.59*69.5;
topTLP66=Solderarea/Scanarea
```

A.6 MATLAB Script for Calculating DOE Cause and Effects

```
%PhDMattDOE.m
%Matt Chan DOE Observations
%Full Factorial Design of Experiments to quantify effects of
%SLID Bonding Parameters
y1=23.327; %Units in kg "force" applied to die
y2=11.821;
y3=19.814;
y4=9.328;
y5=5.734;
y6=47.429;
y7=9.370;
y8=42.227;
c1=((1/4)*(y2+y4+y6+y8))-((1/4)*(y1+y3+y5+y7)) %Thick. of Au80Sn20 Foil
c2=((1/4)*(y3+y4+y7+y8))-((1/4)*(y1+y2+y5+y6)) %Thick. of Au Plating on SS316
c3=((1/4)*(y5+y6+y7+y8))-((1/4)*(y1+y2+y3+y4)) %Thick. of Au Plating on SiC
```

Appendix B

Process Recipes and Notes for SLID Bonding

B.1 E-Beam Evaporation Thin Films Deposition

Electron Beam evaporation was used to deposit the adhesion layers of titanium and gold onto the silicon carbide substrates. The EdwardsEB3 evaporation tool in the UC Berkeley Nanofabrication laboratory was used to deposit the films. A tooling factor of 0.5 was used for the titanium and gold films.

After pumping to a chamber pressure of 1×10^{-6} torr, a tooling factor of 0.5 was used and a crystal monitor was used to measure the thickness of the deposited film. 50 nm of titanium and 50 nm of gold were deposited as an adhesion layer and seed layer for the following electroplating steps.

B.2 Electroplating

Electroplating was performed with Technigold 434-RTU (ready-to-use) neutral gold electroplating solution, manufactured by Technic, Inc. A platinized electrode 2 cm by 2 cm was used as the anode. An alligator clip was used to connect the prepared silicon carbide dies and stainless steel dies, making them the cathode. A Keithley 2400 Sourcemeter was used to monitor the process through the use of a GPIB cable and a National Instruments LabVIEW virtual instrument.

The manufacturer's recommended current density of $0.3\,\frac{\mathrm{A}}{\mathrm{dm}^2}$ was used to achieve an electroplating rate of $0.19\,\frac{\mathrm{\mu m}}{\mathrm{min}}$.

B.3 Substrate Dicing

Dicing of the silicon carbide substrate was performed in the UC Berkeley Marvell Nanofabrication Laboratory. A Dicing Technology CX-010-270-080-H blade was used for the dicing of the silicon carbide wafers.

A spindle speed of 30,000 rpm and a cutting speed of 0.25 $\frac{mm}{s}$ was used. With a dicing tape thickness of 120 µm a blade dicing height of 100 µm was used to ensure that the blade would cut all the way through the silicon carbide die.

B.4 Heating the SLID Bond

For the heating of the SLID bond a Hewlett Packard 6263B DC power supply was used to supply power to the Sakaguchi E.H Voc Corp. MS-M1000 micro ceramic heater. The power supply was operated in a voltage limited mode, and the voltage was increased at specified time intervals to achieve the desired heating rate and temperatures for the SLID bond. Table B.1 provides the recipe used

Table B.1: The recipe used for the heating of the MS-M1000 micro ceramic heater using the Hewlett Packard 6263B DC power supply. 1 A of current was drawn by the heater for the various voltages applied

Time (s)	Applied Voltage (V)
0	0
10	1
20	2
30	3
45	3.5
60	4
75	4.5
90	5
120	6
150	6.5
180	7
210	7.5
240	8
270	8.5
...	8.5
1100	7
1140	6
1180	5
1220	4
1260	3
1300	2
1340	0